Bio-nano-transformations de nanoparticules en milieu cellulaire

Alexandre Fromain

THESE DE DOCTORAT
D'UNIVERSITE PARIS CITE

Spécialité : Physique
Ecole doctorale 564 Physique en Ile-de-France

Réalisée
Au laboratoire Matière et Systèmes Complexes (MSC), CNRS UMR 7057
Au laboratoire Physico-Chimie Curie (PCC), CNRS UMR168

Sujet de Thèse :

Bio-Nano-Transformations de nanoparticules en milieu cellulaire

---

Présentée par Alexandre FROMAIN

Dirigée par Claire WILHELM

Soutenance prévue le 20 juillet 2022 devant le jury composé de :

Rapportrice : Mme **Charlotte RIVIERE**, Maître de conférences, Université Lyon 1, ILM.

Rapporteur : Mr **Stéphane MORNET**, Directeur de recherche CNRS, Université de Bordeaux, ICMBM.

Président du Jury : Mr **Frédéric KANOUFI**, Directeur de recherche CNRS, Université Paris Cité, ITODYS.

Directrice de thèse : Mme **Claire WILHELM**, Directeur de recherche CNRS, PCC.

Table des matières

Remerciements

Je voudrais dans un premier temps remercier Charlotte Rivière et Stéphane Mornet d'avoir accepté d'être rapporteur de mon travail de thèse de doctorat. J'aimerai également remercier Frédéric Kanoufi en tant que président du jury.

Un immense merci à Claire de m'avoir encadré pendant toute ma thèse. Merci pour la bonne humeur et pour toutes ces idées qui n'ont de cesse aider à voir encore plus loin. Encore merci de m'avoir donné la possibilité d'interagir dans pleins de domaines et de projets différents.

Un merci tout particulier à Aurore qui m'aura initié au projet de Biosynthèse et qui se sera impliquée plus qu'elle n'aurait dû. Merci. Je remercie également Alberto de m'avoir accompagné dans de nombreuses expériences, ainsi que dans la découverte des manips vivo. Merci à Anouchka d'avoir pris le temps de m'aider à découvrir les secrets de la photothermie. Merci à Efrain pour toute l'aide et la participation à l'étude sur la dégradation.

Je remercie également Yoann et Ali de m'avoir fait participer aux synthèses de nanoparticules ainsi que pour les conseils avisés. Merci à Ana de m'avoir permis de réaliser des expériences aux différents Synchrotron. Merci à Natalie de m'avoir distillé de précieux conseils sur la culture cellulaire.

Un grand merci à tous les membres et les personnes croisées dans les laboratoires MSC et IPGG, avec qui j'ai eu la chance de travailler ou même simplement d'échanger, merci à tous cela a été un réel plaisir. Un merci également à l'ensemble des collaborateurs avec qui j'ai eu la chance de travailler.

Un merci également à Catherine et Miryana, qui ont bien voulu me donner une chance quand j'en avais besoin. Un merci également à Miryana et Claire pour les conseils et d'avoir participé lors de mes comités de thèse.

Un remerciement tout particulier à ma famille et mes amis.

Résumés

Les nanoparticules magnétiques occupent toujours une place centrale en biomédecine compte tenu de leurs propriétés multifonctions, d'origines magnétique ou optique. Ainsi, elles sont au cœur du développement de nouvelles méthodologies diagnostiques et thérapeutiques, tels que le ciblage et l'administration de médicaments, la thérapie génique, les thérapies thermiques contre le cancer ou la médecine régénérative. Néanmoins, toutes les avancées biomédicales fondées sur l'utilisation des nanoparticules magnétiques, notamment pour les thérapies cellulaires, nécessitent de questionner en profondeur les bio-nano-transformations que ces nanoparticules peuvent subir au cœur des cellules, domaine de recherche encore jeune. Dans ce contexte, les nanoparticules d'oxyde de fer occupent une place bien particulière, car leur cœur est composé de fer, qui peut intégrer le métabolisme du fer de l'organisme, et ainsi assurer une biocompatibilité optimale.

Cette thèse propose deux approches de l'étude des biotransformations des nanoparticules d'oxyde de fer dans les cellules.

La première se focalise non pas sur la dégradation de nanoparticules synthétisées par voie chimique, mais plutôt sur la possible cristallisation intracellulaire de nanoparticules magnétiques, alors biogéniques. En effet, des nanoparticules magnétiques ont été détectées chez l'homme, en particulier dans le cerveau, et récemment, l'équipe a montré que la recristallisation de nanoparticules magnétiques était possible, après dégradation, dans les cellules souches, première preuve que les cellules humaines sont capables d'une biosynthèse magnétique. Dans cette thèse, nous avons tenté de reproduire cette biosynthèse en cellules souches de mammifère (souris) mais cette fois uniquement à partir de sels de fer mis au contact des cellules. Nous avons ainsi pu conduire une étude précise sur l'entrée du fer dans les cellules, et de son devenir sur le long terme, avec la possible apparition d'un signal biomagnétique. Cette approche est présentée dans le chapitre 3.

La seconde approche a été de suivre leur devenir après une thérapie thermique activée par les nanoparticules elles-mêmes. En effet, les nanoparticules d'oxyde de fer sont les acteurs principaux de l'hyperthermie magnétique anticancéreuse, et plus récemment, elles ont été décrites comme des agents également très efficaces pour la photothermie dans la fenêtre biologique infrarouge. Néanmoins, leur devenir après chauffage est peu étudié. Nous avons ainsi pu montrer que l'application d'un laser pouvait déclencher une dégradation importante des nanoparticules. Cette mesure a dans un premier temps permis de mesurer l'échauffement local autour d'une nanoparticule. Nous avons ensuite exploré comment cette dégradation sous irradiation laser avait lieu dans les cellules, en fonction de la localisation membranaire ou endosomale des nanoparticules. Enfin, nous avons corrélé cette dégradation à l'efficacité de la thérapie anticancéreuse. Ces travaux sont présentés dans le chapitre 1.

Finalement, une dernière partie de la thèse s'est concentrée sur une étude plus classique de photothermie anticancéreuse, à partir d'un nouveau type de nanoparticules, à base de platine, qui s'avèrent être également des agents photothermiques efficaces. De plus une dégradation du platine pourrait être un atout pour une photo-chimio-thérapie combinée. Nous démontrons dans un premier temps dans cette thèse qu'une thérapie photothermale anticancéreuse est effectivement possible avec des nanoparticules de platine intracellulaires (chapitre 2).

Mots clés : Nanoparticules, Magnétisme, Dégradation, Photothermie, Biosynthèse, Oxyde de Fer, Platine.

Abstract:

Magnetic Nanoparticles (Nps) rise more and more interest in biomedical thanks to its multifunctional features like magnetism or optical. Nanoparticles have an important place in the development of new diagnostic or therapeutic method, like targeting, drug administration, thermal therapy against cancer or regenerative medicine. Due to the increasing use of magnetic nanoparticle in biomedical, especially in cellular therapy, it raises the question of Bio-nano-transformation of these nanoparticles in the organism. Therefore, I approach the study of transformations that nanoparticles undergo in cells. Firstly, I followed Nanoparticle's fate with photothermal therapy activated by Nps themself. Indeed, iron oxide nanoparticles have increasing interest due to its great biocompatibility with its iron core that can be integrated by the iron metabolism of the organism. Theses nanoparticles also showed good capacity in biological windows for photothermal therapy. Thus, they can be used as a treatment for cancer by inducing heat via laser exposure before having biotransformation in endosome to be integrated in the organism. The Second approach rely on the study of platinum nanoparticle as a heating agent for photothermal therapy to compete with the well establish gold nanoparticles. This is a new stable metal that showed great optical response, so we tested them to identify their usability in thermal therapy. Lastly, we studied the production of magnetic iron oxide nanoparticles by stem cell, based on newly reported biosynthesis by human cells. Indeed, magnetic nanoparticles have been found in human brain or reported in cells as a recrystallization of degraded magnetic nanoparticles in human stem cells, which highlight the capability of human stem cell to perform biosynthesis. Therefore, we tried to identify and increase biosynthesis of magnetic iron oxide nanoparticle made of non-magnetic iron precursor by stem cells, following magnetotactic bacteria's culture.

Key words: Nanoparticles, Magnetism, Degradation, Photothermia, Biosynthesis, Iron Oxide, Platinum.

Introduction générale

Le développement récent des nanotechnologies pour le domaine biomédical est en partie le résultat des multiples recherches autour de l'utilisation de nanoparticules, pour des approches diagnostiques et thérapeutiques. La nanomédecine est considérée, pour beaucoup, comme la médecine du futur.

En effet, les nanoparticules permettent d'accéder à un large éventail d'actions issues de leurs multiples propriétés pour répondre à de nombreux enjeux via une nouvelle approche. Ces propriétés se déclinent en fonction de la forme, la taille, l'habillage, la fonctionnalisation ou la composition du cœur des nanoparticules [1,2]. Elles génèrent soient des actions thérapeutiques supplémentaires, soit une amplification d'une propriété déjà existante. L'atout principal des nanoparticules est sans doute leur taille, à l'échelle nanométrique, qui permet des interactions intimes avec l'environnement biologique, comme une circulation facilitée dans l'organisme ou la possibilité de franchir certaines barrières biologiques. Elles peuvent aussi cibler un type cellulaire, voir même un compartiment cellulaire, puis être activées à distance par une stimulation, par exemple de leur cœur, limitant ainsi les effets néfastes possibles sur les cellules alentours saines.

Par exemple, les nanoparticules inorganiques offrent la propriété de pouvoir être activées à distance par un stimulus physique tel que le magnétisme ou via un rayonnement lumineux pour permettre un contrôle, spatial et/ou temporel, de l'action thérapeutique de la nanoparticule, ou encore pour libérer de façon contrôlée un principe actif associé à la nanoparticule[3,4,5,6].

Dans ce paysage en pleine expansion, les nanoparticules magnétiques, probablement les plus anciennes, sont encore en plein essor pour des applications médicales telles que les thérapies thermiques (hyperthermie magnétique ou photothermie), l'imagerie par résonance magnétique nucléaire (IRM), la délivrance ciblée, le traitement de l'anémie, ou l'ingénierie tissulaire[7]. Généralement considérées comme biocompatibles[8], la question du devenir à long terme des nanoparticules magnétiques reste d'actualité, pour pouvoir envisager leur utilisation pour des traitements où elles resteront par la suite, sur le site dans l'organisme.

Il faut commencer par insister sur le fait que le fer est impliqué dans le métabolisme humain, même essentiel à la survie des organismes[9,10], et que donc les oxydes de fer sont par essence des candidats idéaux dans le développement de thérapies. Le rôle du fer dans l'organisme est particulièrement bien documenté, que ce soit pour sa fonction de métal de transition impliqué dans des réactions d'oxydation/réduction mais aussi pour son action métabolique avec les protéines et transporteurs associés[11]. Cependant, toute la connaissance du Fer endogène

présent dans l'organisme le décrit sous une forme non magnétique. Le fer magnétique est davantage singulier et sa présence est très peu documentée chez les mammifères. Pourtant, il est possible d'en retrouver dans des organes tels que le cerveau, le cœur, ou même les tumeurs[12,13].

Récemment, la première preuve que nos cellules souches humaines étaient capables de produire du fer magnétique a été apportée de manière indirecte après internalisation de nanoparticules d'oxyde de fer synthétisées par voie chimique. En effet ces nanoparticules chimiques commencent par être dégradées dans la cellule, mais le ions fer libérés par cette dégradation sont ensuite utilisés pour recristalliser de nouvelles nanoparticules d'oxyde de fer magnétique. Cette néosynthèse a lieu entre 9, et après 21 jours après l'internalisation des nanoparticules chimiques, et elle met en lumière la capacité des cellules souches à produire de manière biogénique du fer magnétique.[13,14,15]

Cette nouvelle capacité de recristallisation in cellulo de nanoparticules montre qu'il reste encore beaucoup à explorer quant au devenir à long-terme des nanoparticules magnétiques. Même si leurs multiples propriétés leur ont permis de s'installer solidement dans le domaine des applications cliniques, la majorité des applications envisagées étudient les interactions immédiates des nanoparticules avec l'organisme, le plus souvent via leur internalisation dans les cellules. Comprendre et contrôler les biotransformations intracellulaires qui s'ensuivent est non seulement essentiel mais aussi potentiellement porteur si de nouvelles espèces chimiques réactives peuvent être créées sur un plus long terme.

La première partie de ce manuscrit de thèse porte sur l'étude de l'environnement auquel des nanoparticules d'oxyde de fer synthétiques sont exposées durant leur internalisation en cellule et l'impact que celui-ci peut avoir sur leur dégradation afin de pouvoir contrôler cet aspect. Ainsi, nous avons voulu savoir si le chauffage induit par ces nanoparticules en étant soumises à un rayonnement laser pouvait impacter leur structure. Nous avons en effet observé que ce chauffage laser pouvait déclencher une dégradation importante des nanoparticules, et que la quantification de cette dégradation était un moyen d'estimer la température locale générée dans le voisinage immédiat de la nanoparticule, de façon non intrusive (sans sonde). Cette étude a été réalisée dans des solutions aqueuses mimant le milieu de dégradation avant de l'exploiter sur un modèle 3D de cellules cancéreuses de glioblastome.

La seconde partie du manuscrit est focalisée sur la compréhension du mécanisme de biosynthèse de nanoparticules magnétiques par les cellules souches. L'objectif était de tenter de déclencher cette biosynthèse à partir de sels de fer (non magnétiques). Pour ce faire, nous nous sommes appuyés d'un coté sur la récente observation de cellules souches humaines capables de néosynthétiser des nanoparticules d'oxyde de fer magnétique à partir de produit

de dégradation de nanoparticules chimiques, mais aussi, d'un autre côté, sur les études approfondies sur bactéries magnétotactiques qui synthétisent leurs propres nanoparticules (magnétosomes) à partir de sels de fer.

1. Biodégradation des nanoparticules magnétiques dans les cellules ou dans des milieux mimant l'environnement intracellulaire

Les nanoparticules utilisées en nanomédecine diffèrent par leur taille, leur forme, leur matériau de cœur ou leur habillage, et sont généralement optimisées pour remplir au mieux une fonction choisie. Le cycle de vie idéal d'une nanoparticule démarre donc par sa synthèse, avec l'objectif de lui conférer une stabilité suffisante pour rester intègre et fonctionnelle jusqu'à son action thérapeutique et se termine par son recyclage au sein des cellules de l'organisme, qui doit permettre d'éviter toute toxicité à long terme.

Dans cette thèse, les nanoparticules étudiées ont été choisies pour être les plus simples possibles, afin de pouvoir généraliser les résultats au plus grand nombre de nanomatériaux possibles. Elles ont un cœur en oxyde de fer de 9 nm avec un enrobage de surface composé citrate qui permet d'assurer la stabilité colloïdale en solution. Elles ont été déjà largement utilisées pour des applications biomédicales[16,17,18,144] et sont internalisées par les cellules de manière rapide et efficace.

De plus, plusieurs études ont déjà été effectuées avec ce type de nanoparticules montrant leur biodégradation intracellulaire qui débute rapidement, après 1 ou 2 jours, suivant l'incubation et le confinement dans les lysosomes. Elles peuvent être quasi totalement dégradées après 9 jours et le fer libéré est généralement stocké sous forme de ferrihydrite dans les ferritines.[19,20,21]

En amont de la biodégradation, les nanoparticules sont internalisées dans la cellule par le processus d'endocytose et sont confinées dans des endosomes, puis après fusion, dans les lysosomes, dont l'environnement est composé d'enzymes, de protéines et de lipides, avec un pH acide (4.5-4.7)[22,23]. C'est dans cet environnement qu'a lieu la dégradation des nanoparticules en ions ferrique Fe^{3+} ou ferreux Fe^{2+}, avant d'être pris en charge par l'organisme, et c'est probablement le pH acide couplé à la présence de chélatant du fer qui sont la cause de la dégradation des nanoparticules, sans toutefois que cela ait été démontré jusqu'à présent. Les cellules sont donc exposées à une forte concentration de fer qui doit être pris en charge par l'organisme pour éviter tout effets toxiques.

En parallèle, des études de dégradation ont été menées dans des milieux mimant l'environnement lysosomal, afin de pouvoir clairement identifier l'impact des différents paramètres sur la dégradation des nanoparticules. Typiquement, ce milieu de dégradation contient des ions citrates, chélateur du fer, et un pH acide (4.5).[16,24]

2. La magnétométrie permet de quantifier la dégradation des nanoparticules magnétique

Afin de pouvoir suivre la dégradation des nanoparticules en solution et en cellules, celle-ci a été mesurée par la quantification du signal magnétique, qui est la signature directe des transformations subies par les nanoparticules : la diminution du signal magnétique, en conservant une quantité de fer constante, correspond à la dégradation du cœur d'oxyde de fer des nanoparticules[25,26,27,28,29]. Ce suivi est généralement effectué par magnétométrie (VSM ou SQUID) qui permet de mesurer des aimantations allant jusqu'à du microemu (µemu). C'est typiquement lesignal obtenu pour environ 100 000 cellules ayant internalisé autour de 10 pg de fer par cellule. Les détails de cette technique de magnétométrie cellulaire ont été résumés dans un article de démonstration dans JoVE, présenté dans l'Annexe A, et qui a fait partie des travauxde cette thèse :

Using Magnetometry to Monitor Cellular Incorporation and Subsequent Biodegradation of Chemically Synthetized Iron Oxide Nanoparticles par Van de Walle A, Plan A, **Fromain A**, Wilhelm C, Lalatonne Y. Jove (2021).

Néanmoins ces mesures magnétiques nécessitent de travailler sur cellules fixées, rendant impossible le suivi du signal magnétique sur une même population cellulaire.

Nous avons récemment démontré qu'un senseur magnétique de paillasse pouvait permettre de suivre la biodégradation sur cellules vivantes en temps réel. Cette étude a fait partie du travail de thèse, et l'article publié est présenté dans l'Annexe B :

Real-time in situ magnetic measurement of the intracellular biodegradation of iron oxide nanoparticles in a stem cell-spheroid tissue model, par Van de Walle A, **Fromain A**, Plan Sangnier A, Curcio A, Lenglet L, Motte L, Lalatonne Y, Wilhelm C; Nano Research 13, 467-476 (2020).

Tout d'abord, nous avons montré que le signal magnétique mesuré par le senseur est directement proportionnel au moment magnétique mesuré au magnétomètre. Cette corrélation est aussi valable une fois les nanoparticules internalisées dans les cellules, et reste corrélé après dégradation. En plus d'offrir une mesure rapide, ce senseur magnétique permet donc de suivre l'évolution d'un signal en temps réel, sans avoir à fixer l'échantillon ; de plus la mesure n'affecte pas l'échantillon qui peut donc être remesuré au cours du temps. Cependant, le signal magnétique obtenu est très spécifique de la taille de la nanoparticule, et doit donc être recalibré pour chaque nanoparticule.

3. Devenir des ions ferreux et ferriques après dégradation

Après dégradation, les ions ferreux et ferriques libérés du cœur des nanoparticules d'oxyde de fer peuvent avoir plusieurs devenirs. Les ions ferriques Fe III sont réduits en ions Ferreux

Fe II par la protéine STEAP3, et peuvent ainsi être transportés dans le cytosol (phase liquide du cytoplasme) par le transporteur DMT1 (divalent metal transporter 1 ou SLC11A2), avant d'être envoyé vers le plasma sanguin grâce à la protéine transmembranaire ferroportine (FPN). Cet export est accompagné d'une activité ferroxydase qui va permettre à l'apotransferrine de se lier à ce fer circulant, qui sera transporté ainsi sous forme Fe III par la transferrine vers les différents tissus, muscles (myoglobine) et moelle osseuse (hémoglobine).[30]

Au sein même de la cellule, l'apoferritine peut lier ces ions ferreux, une fois chargée celle-ci est nommé ferritine. Elle est considérée comme la principale protéine de stockage du fer.

Il s'agit d'un complexe protéique qui peut contenir jusqu'à 4500 atomes de fer en son cœur et est composé de deux sous unités : la sous unité lourde dites ferritine H responsable de l'activité ferroxidase, permettant d'oxyder le Fer II en Fer III ; et la sous unité légère, la ferritine L qui permet la liaison avec le Fer III. Ainsi ces deux molécules sont responsables de la balance et du maintien des ions fer, évitant ainsi la réaction toxique de Fenton :

($Fe^{2+} + H_2O_2 \rightarrow Fe^{3+} + OH^- + \bullet OH$).

Le Fer des nanoparticules libéré par la prise en charge de l'organisme est donc un mécanisme connu et résumé par la **Figure 1**.

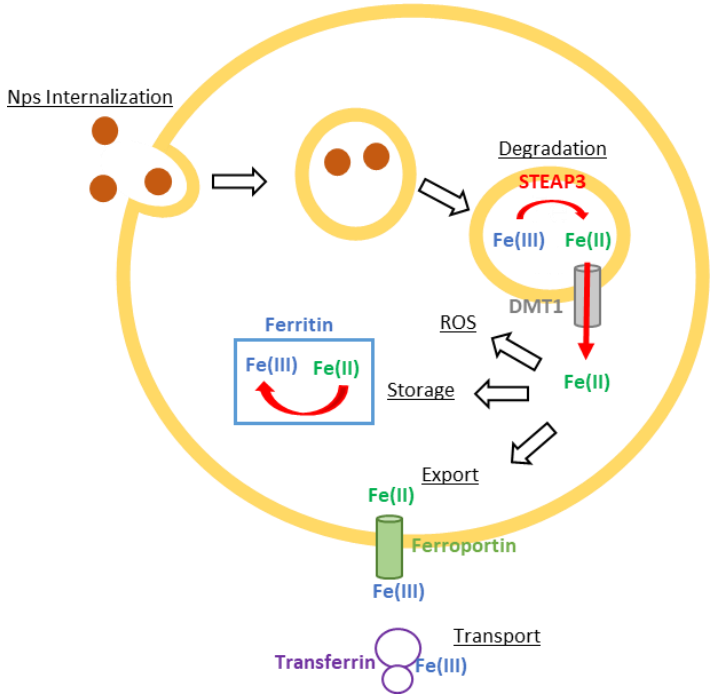

Figure 1 *: Schéma résumant la prise en charge de nanoparticules d'oxyde de fer par les cellules et l'intégration des produits de dégradation dans le métabolisme du fer de la cellule. Les nanoparticules sont internalisées par endocytose, et subissent une dégradation une fois l'endosome fusionné en lysosome. Les ions produits subissent une réduction et sont transportés par DMT1 pour être stockés sous forme de ferritine ou exportés vers l'extérieur de la cellule par la ferroportine et transportés dans tout l'organisme sous forme de transferrine.*

Si le fer est essentiel à la survie des organismes, le métabolisme du Fer met aussi en lumière la possible toxicité d'un excès de fer via les ROS (Reactive oxygen species) pouvant être produits par cette réaction de Fenton. Ce sont donc les ions ferreux Fe^{2+} qui sont cytotoxiques. L'introduction de nanoparticules dans le corps humain induit un apport conséquent d'ions fer instantané, qui doit être maitrisé par l'organisme. Les nanoparticules d'oxyde de fer ont généralement un cœur de maghémite (γFe_2O_3) ou de magnétite (Fe_3O_4). La maghémite présente des Fer tous oxydés (Fe(III)), et est donc préférée pour les applications biomédicales. En revanche, la magnétite a en moyenne un ratio de 1:2 ferreux/ferrique et présente donc un état d'oxydation du fer provoquant un apport en ion Ferrique Fe III qui pourrait induire un stress oxydant aboutissant à la réaction de Fenton. Une concentration élevée de nanoparticules peut avoir un effet cytotoxique, allant d'un dérèglement de la croissance cellulaire à l'apoptose[31,32,33,34]. Cela dit, de nombreuses études ont reporté peu voire pas d'effet cytotoxique lié à l'introduction de nanoparticule d'oxyde de fer dans le corps à des concentrations faibles. Un contrôle de cette cytotoxicité, notamment à long terme, est nécessaire, car elle peut mener à des phases apoptotiques, des dommages sur l'ADN voir affecter la différenciation des cellules.[35]

4 Thérapies thermiques avec des nanoparticules magnétiques

L'utilisation de nanoparticules en thérapie permet de pouvoir contrôler à distance, de façon spatiale et temporelle, l'action thérapeutique. L'une des applications médicales concerne le traitement des cancers par hyperthermie, qui peut être déclenchée soit par l'application d'un champ magnétique soit par un rayonnement laser sur une zone cible.[36,37,38]

La thérapie par l'hyperthermie est étudiée depuis de nombreuses années pour déclencher une réponse cytotoxique sur site tumoral. La fenêtre de chauffage généralement visée est entre 41-48°C car elle permet une augmentation du débit sanguin accompagnée d'une diffusion à travers les membranes, permettant un meilleur approvisionnement des cellules immunitaires et des produits de chimiothérapies, en plus de dénaturer les protéines pouvant mener à la mort cellulaire. Au-delà de 48°C, des effets irréversibles sont générés, entraînant notamment la nécrose. Et au-delà de 60°C, la dénaturation des protéines est instantanée. (**Figure 2**)

37°C – 41°C	Diathermia	- Cellular homeostasis can be maintained - Increment in diffusion rate across membrane - Increment in blood flow
41°C - 48°C	Hyperthermia	- Unfolding and aggregation of proteins - Increased susceptibility to radiation and chemotherapy - Irreversible damage for long exposure (>60min)
49°C – 60°C	Irreversible injury	- Severe and irreversible denaturation of proteins - DNA damage and denaturation - Irreversible damage for short exposure (5min)
+ 60°C	Irreversible injury	- Near instantaneous protein coagulation

***Figure 2**: Tableau récapitulatif des différents effets induits par une élévation de température sur la cellule.*

5. Photothermie

La photothermie est l'application d'un rayonnement électromagnétique par un faisceau laser sur des nanoparticules afin d'augmenter leur température : les photons incidents sont diffusés dans diverses directions ou sont absorbés par les nanoparticules. Quand les photons sont absorbés, les électrons des nanoparticules passent d'un état fondamental à un état excité, et cette énergie est réémise par les nanoparticules sous forme de nouveaux photons (luminescence) ou sous forme de phonons (chaleur) provoquant une augmentation de la température autour des nanoparticules.[39,41]

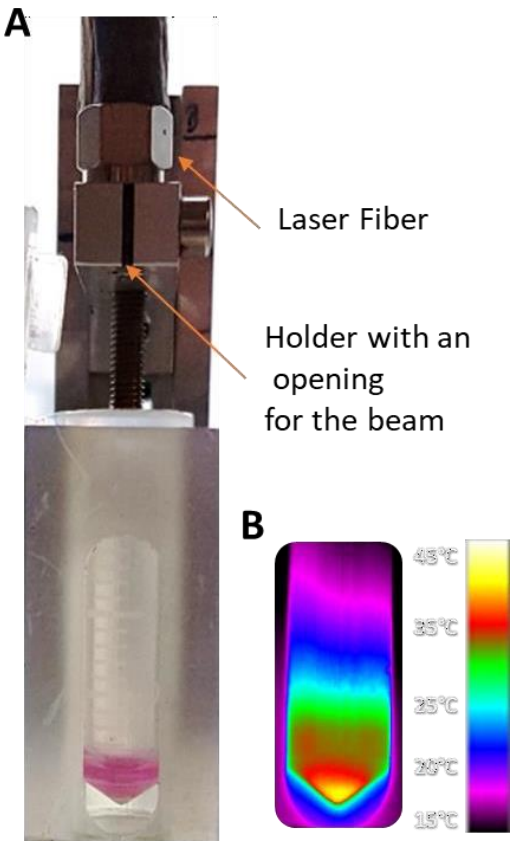

Figure 3 : *Set-up typique pour l'exposition d'un échantillon à une irradiation laser. (A) L'échantillon est placé dans un eppendorf avec le laser dirigé directement sur l'échantillon. La distance entre la surface de l'échantillon et la fibre du laser est mesurée pour calculer la densité de puissance d'exposition. (B) Image typique de l'élévation de température mesurée par une caméra thermique.*

L'un des inconvénients de la photothermie est la difficulté à faire pénétrer le rayonnement lumineux jusqu'à la tumeur, et provoquer l'échauffement seulement dans les cellules cancéreuses où les nanoparticules se sont accumulées et non sur des tissus sains alentours. C'est pourquoi la fenêtre thérapeutique biologique aura tendance à correspondre au proche infrarouge (NIR-I entre 650 et 950 nm et NIR-II entre 1000 et 1300 nm) afin d'avoir une absorbance minimale des tissus biologiques, qui contiennent de l'hémoglobine, de la mélanine ou encore de l'eau, qui absorbent en particulier dans le visible et sont invisible dans l'infrarouge. (**Figure 3**)

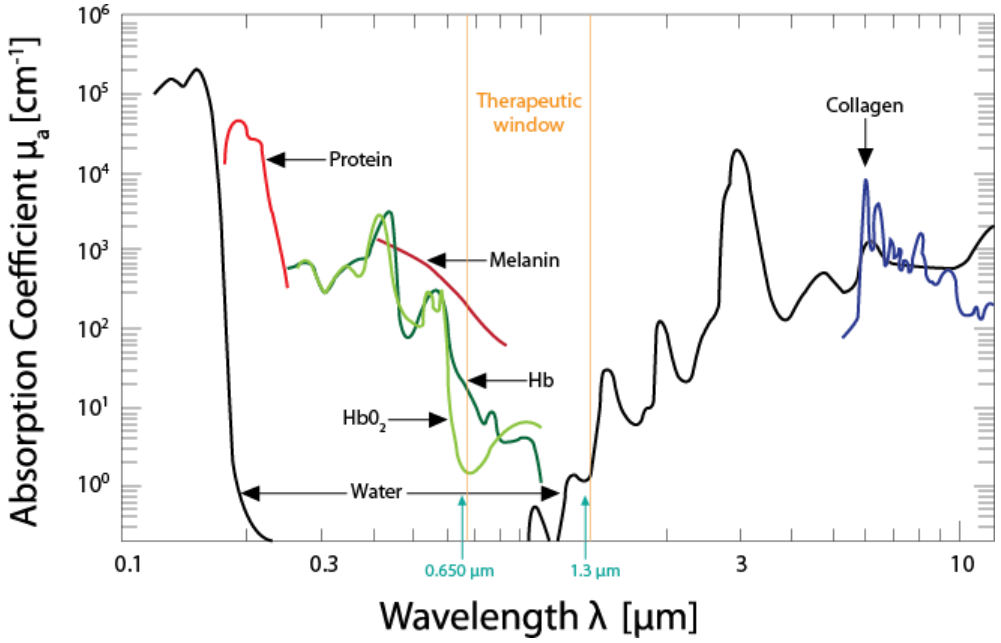

Figure 3 *: Spectre d'absorption en fonction de la longueur d'onde, représentant la fenêtre thérapeutique visée pour une absorption minimale des tissus.*

De nombreux types de nanoparticules sont utilisés pour leur propriétés en photothermie tels que les nanoparticules d'or, les quantums dots ou autres nanoparticules inorganiques. L'utilisation des nanoparticules d'oxyde de fer est plus récente, mais est de plus en plus étudiée. La production de chaleur sous rayonnement dans le proche infra-rouge est alors liée aux transitions de la bande de valence Fe(II)-Fe(III).

Dans ce paysage encore en plein essor de l'utilisation de nanoparticules magnétiques dans le domaine biomédical, cette thèse s'est concentrée sur les propriétés de biodégradation et de photothermie (chapitres 1 et 2), et de biosynthèse (chapitre 3).

CHAPITRE 1 : Biodégradation des nanoparticules magnétiques sous rayonnement laser

Le devenir des nanoparticules après avoir accompli leur mission thérapeutique est une question centrale de la nanomédecine. Pour des nanoparticules d'oxyde de fer, cette question est doublement importante, car le fer est un des métaux les plus abondants dans l'organisme, avec un taux de 0.1% du poids total, juste après le magnésium (0.1% également), le sodium (0.15%), le potassium (0.2%) et le calcium (1.5%). Le fer est donc indispensable au fonctionnement de l'organisme, et la dégradation de nanoparticules d'oxyde de fer doit être étudiée en lien étroit avec l'intégration de fer relargué au sein du métabolisme du Fer de l'organisme. Comprendre la dégradation de ces nanoparticules est donc essentielle à leur utilisation, mais au-delà, pouvoir contrôler cette dégradation serait également un atout de taille. En effet, l'objectif serait alors d'avoir des nanoparticules qui resteraient stables et intègres jusqu'à leur action thérapeutique, mais qui puissent ensuite être dégradées pour intégrer in fine le métabolisme du fer.

Dans l'étude qui suit, nous avons donc adopté une double approche. D'un côté, nous avons étudié l'impact des composantes responsables de la dégradation des nanoparticules (pH lysosomal, chélateurs du fer, température). De l'autre côté, nous avons cherché à trouver un stimulus externe qui permette de contrôler, à un instant donné, la biodégradation dans l'environnement biologique.

Il est important de commencer par insister sur le fait que l'ensemble de cette étude n'a été rendue possible que grâce aux propriétés magnétiques des nanoparticules d'oxyde de fer. En effet, c'est un atout de taille pour avoir un paramètre de contrôle quantitatif de l'intégrité structurale des nanoparticules, et donc un indicateur de leur dégradation. L'utilisation de magnétomètres (SQUID, VSM) aurait pu être suffisante pour réaliser la mesure de dégradation. Néanmoins, chaque mesure nécessite au moins 5 min dans l'appareil, ce qui limite le nombre d'échantillons testés en solution, et la mesure dans les cellules nécessite une fixation préalable, donc rendant impossible de faire un suivi du magnétisme sur le même échantillon cellulaire. A l'opposé, le senseur magnétique introduit dans le chapitre précédent, et décrit dans l'Annexe B, permet une mesure en moins de 40 sec, sur un volume de 100 µL, qui peut être fait soit en temps réel, soit échantillonné autant de fois que nécessaire, et la mesure sur cellules vivantes est totalement non invasive, pouvant être répété autant de fois que nécessaire. C'est donc grâce à ce senseur magnétique que nous avons pu dans la première partie de l'étude établir les cinétiques de dégradation, et mettre en évidence le rôle de la température, du citrate (en tant que chélateur du fer), et du pH.

L’autre atout des nanoparticules d’oxyde de fer est leur capacité à générer de la chaleur sous champ magnétique alternatif (hyperthermie magnétique) ou sous rayonnement laser (en particulier dans le proche infrarouge où les tissus sont relativement transparents). Cette utilisation comme activateurs de chaleur sous stimulation laser proche infrarouge est en plein essor pour la thérapie photothermique anticancéreuse. L’étape suivante a été d’explorer la possibilité de provoquer la dégradation sous rayonnement laser, via une augmentation de la température.

De manière attendue, le chauffage des solutions de nanoparticules par l’application du laser accélère bien la dégradation, tout comme le fait un chauffage global des solutions en bain-marie. En revanche ce qui est remarquable, pour une même température de solution mesuré, on observe une dégradation sous laser plus importante qu’en bain-marie. Cela reflète directement la température locale autour de la nanoparticule issue de l’irradiation laser qui est rapidement dissipée dans la solution. La température mesurée en solution est donc la température globale. Il devient donc possible d’estimer la température locale comme la température nécessaire par un chauffage global pour dégrader autant de nanoparticules.

Nous avons ainsi pu remonter au chauffage local autour de la nanoparticule, ou de manière équivalente au gradient de température entre la nanoparticule et le bain. Ce chauffage local ("hot spot") autour d’une nanoparticule restait une question centrale aux traitements thermiques en nanomédecine, avec quelques études qui avaient tenté de le mesurer, mais avec des approches bien plus complexes, soit via des sondes thermosensibles fonctionnalisées à la surface des nanoparticules [40,41]ou une mesure structurale au synchrotron (XAS)[42,22,43].

Munis de ces différents outils, nous avons dans un second temps pu explorer cette dégradation déclenchée par laser directement dans l’environnement cellulaire, après, ou même pendant l’internalisation des nanoparticules d’oxyde de fer magnétique dans les cellules. Afin d’étudier ces effets, l’étude a été réalisée sur un modèle sphéroïde de cellules tumorales de glioblastome. Le modèle 3D de sphéroïdes (tumoroïdes) permet une approche plus réaliste que la culture cellulaire 2D de cellules tumorales. Ce modèle permet aussi de suivre la dégradation quantitativement et en temps réel à l’aide du senseur magnétique, à l’échelle d’un sphéroïde unique. Finalement, il permet également l’application ciblée du laser au niveau du sphéroïde qui se comporte comme un système fermé contenant un nombre constant de nanoparticules (ou plutôt d’atomes de fer, lorsque les nanoparticules commencent à être dégradées).

Mais surtout, ce modèle sphéroïde nous a permis de localiser les nanoparticules séquentiellement, soit au niveau des membranes et des endosomes précoces, soit dans les endosomes tardifs et les lysosomes, au moment de l’exposition au laser. Nous avons tout

d’abord ainsi pu confirmer que le laser permettait de déclencher la dégradation également dans l’environnement cellulaire. Et cette dégradation forcée sur des temps courts a ensuite permis de mettre en évidence que les nanoparticules étaient exposées à un milieu de plus enplus propice à la dégradation au fil de leur internalisation.

Quant à la mortalité cellulaire liée à l’irradiation des sphéroïdes, l’effet du chauffage local est bien mis en évidence pour les conditions sous rayonnement laser, mais sans effet significatif du lieu d’internalisation donc pas d’effet de la dégradation sur la toxicité.

A ce stade, nous avons donc répondu à la question initiale : peut-on déclencher la dégradation via l’échauffement localisé autour des nanoparticules ? De même, nous avons pu utiliser cette dégradation sous laser comme indicateur de la température locale (hot spot) autour de la nanoparticule. Il restait alors à exploiter cette dégradation pour la thérapie, et l’utiliser pour relarguer des Fe^{2+} cytotoxiques en une thérapie combinée PTT-ferroptosis. C’est ce que nous démontrons en fin d’étude.

L’ensemble des résultats est rédigé dans les pages suivantes sous le format d’un article.

Abstract

Magnetic iron oxide nanoparticles have become fundamental over the years for their exciting potential in biomedical applications. It thus becomes essential to follow and control the ultimate fate of iron oxide nanoparticles due to their diagnostic and therapeutic activity in synergy with the endogenous cellular iron metabolic pathway. With the aim of manipulating and optimizing their use, we focused on environmental conditions affecting nanoparticles in order to influence and exploit nanoparticle transformation during their bio-assimilation, using their inherent magnetism as an imprint of this transformation. Here, we established a suitable *ex cellulo* environment for nanoparticle degradation by mimicking the low pH of lysosomal medium, which is responsible for nanoparticle degradation after cell endocytosis. Additionally, we evidenced the impact of temperature on nanoparticle degradation and further used their photothermal properties to control the degradation process, allowing the estimation of local heating profiles. Lastly, we proposed a controlled nanoparticle localization protocol in a tumor spheroid model to evidence the difference degradation profile of the nanoparticles under photothermal therapy as they are endocytosed and processed intracellularly, highlighting cytotoxicity effects due to high local temperature reached and the release of ferroptosis precursor elements during degradation.

Introduction

Nanomedicine emerged as one of the most attractive fields of research due to the wide range of possible treatments made possible by the properties of nanoparticles. Magnetic nanoparticles were previously proposed for therapies like regenerative medicine [44,45,46], organized tissue [1,47,48,49], thermal and magnetic therapy[34], or as magnetic targeting carriers [50,51], but were also exploited as contrast agents for magnetic resonance imaging [52,53,54] or simply as an iron supplement for anemia[55]. The use of magnetic nanoparticles at the cell interface in these domains raised the question of their fate in the organism after the completion of their therapeutic goal [17,56,57]. For the majority of nanoparticles, they showed a decreased stability[21] and loss of magnetic properties, which implied a degradation response with possible detrimental effects such as cytotoxicity via the release of reactive ion species. While increasing preclinical studies focused on tailoring nanoparticle properties such as their core and coating in order to ameliorate these effects[14,17,58], the long-term degradation of nanoparticle still presented some direct cytotoxicity [59,60].

Iron-based nanoparticles have been a central focus in the field, in part due to this element being highly abundant and essential for many biological functions in the organism[8]. This essentially translates into a good biocompatibility, thus reducing a possible nano-cytotoxic effect and with the possibility of integration of iron nanoparticles inside cells with endogenous iron related metabolic pathways, such as ferritin storage[23,61,62]. Indeed, multiple studies *in vivo* identified the ultimate transformation of iron oxide nanoparticles with their bio-assimilation after therapy[17,56,57,], the assimilation of iron oxide nanoparticles with their ultimate transformation in the organism, highlighting their good fit in the nanomedicine field.

Within this framework, it is of interest to follow the evolution of iron oxide nanoparticles *in cellulo*. One of their unique properties can be used for this purpose: their magnetism. Intracellular nanoparticle degradation naturally entails a loss of their magnetic properties, which allows the direct quantification of their degradation and transformation[16,24]. Using a custom magnetic sensor[63] or a vibrating sample magnetometer (VSM), we were able to measure the kinetics of degradation of iron oxide nanoparticles inside a biological environment[13,63]. Iron oxide nanoparticle internalization leads to iron release in endosomes, which could be degraded over 10 days[14,16,17,64,65,66,67,68], yet interestingly without huge impact on iron homeostasis due to ferritin storage acting as a regulator of the iron byproducts[17,69,70,71]. Released iron can further be mobilized for use in the body, or it can be the source for neo-synthesis of new iron nanoparticles by recrystallisation: an exposure to a high nanoparticle dose in stem cells results in the neo-synthesis of nanoparticles after the initial degradation, which involves ferritin and its protein as a catalyzer acting as a detoxification process established by the cell to rid itself of iron excess [13,18]. Nevertheless, this mechanism of protection to maintain iron homeostasis establishes that despite the

biocompatibility of iron, checks are in place at the cellular level to prevent cytotoxicity. Indeed, the degradation of iron oxide nanoparticles into a high pool of free iron played an essential role in the mechanism of ferroptosis [18,72,73,74,75], a non-apoptotic form of cell death with the iron-dependent accumulation of reactive oxygen species by the Fenton reaction culminating in cell damage.

Ferroptosis activation is a novel way to use iron oxide nanoparticle in cancer therapy [76,77,78]. Another approach is hyperthermia therapy, which consists in the elevation of the tumor temperature to induce apoptosis. There are two main nanoparticle-based thermal therapies: magnetic hyperthermia (MHT)[35,50,54,79,80] and photothermal therapy (PTT)[36,37,38,39,50], based on the use of a magnetic field or photothermal irradiation via laser, respectively. Iron oxide nanoparticles are potent photothermal agents, showing a better efficiency with laser excitation in the near infrared (NIR)[50].

In this increasing field of research around iron nanoparticles, it is essential to monitor and control their degradation. Here, we monitored iron oxide nanoparticle degradation using a lysosomal-like solution[22,23,81] of acidic pH and containing citrate as an iron chelating agent to identify parameters influencing degradation. In addition, we focused on the influence of temperature increase through PTT as a degradation accelerator which would allow a coupled therapy using temperature increase and the cytotoxicity of the degradation products. In summary, we found that pH and the ratio of iron chelating agents and nanoparticles mediate nanoparticle degradation, with temperature acting as an accelerator. Thus, we used PTT as heating element to trigger degradation. Interestingly, we observed a higher degradation in our *ex cellulo* model for photothermal irradiation compared to a controlled global heating application (water bath heating the solution homogeneously), highlighting that PTT induced a higher local heating at the nanoparticle level. This novel approach allowed us to estimate the local nanoparticle temperature reached by comparing the degradation rates between the two heating methods. We additionally coupled PTT and ferroptosis as a cumulative therapy with iron oxide nanoparticles.

Results and discussion

1. A custom magnetic sensor to follow nanoparticle degradation

We used iron oxide superparamagnetic nanoparticles with an average diameter of 8 nm synthesized through a known method[82] and coated with citrate as a stabilizing agent. We used the magnetometry signal as a direct representation of the integrity of the nanoparticles[16,24] in order to follow their degradation under different conditions. Standard magnetometry methods typically require large-scale equipment that may not be readily available. Here, we

used a custom bench-top magnetic sensor device to have a quick and effective magnetometry quantification[13,63]. The device's output is a dynamic signal based on the non-linearity of the magnetization of the nanoparticles. Briefly, nanoparticles are exposed to a two-frequency alternating magnetic field variating between two amplitudes. The rather quick measurement allows a dynamic monitoring of nanoparticle integrity without any sample preparation. The output signal is proportional to the quantity of magnetic nanoparticles, expressed in arbitrary units, and can be converted into magnetic moment (emu), as both measurements showed a very strong correlation ($r^2 > 0.99$) (**Figure 1A**). **Figure 1B** shows a schematization of the coil of the custom bench-top device used for the measurement.

2. Environment required for nanoparticle degradation

We used a lysosomal-like solution to investigate the conditions that influence nanoparticle degradation, since nanoparticles are usually internalized via the endosomal pathway in cells and are ultimately localized within lysosomes. This solution was made to mimic the low, acidic pH of lysosomes, with added citrate as an iron chelating agent. A solution of nanoparticles at [Fe] = 2 mM nanoparticles at pH = 4.5 was prepared with a citrate content ranging from 0 to 20 mM and measured over different temperature and time intervals. The nanoparticles showed a maximum degradation after 22 hours at room temperature with a clear influence of the citrate concentration: from no significant sign of degradation with no iron chelating agent to an almost total degradation for a citrate concentration of 20 mM, or a 10-fold ratio of [Citrate]: [Fe] (**Figure 2A**). Moreover, an increase in temperature speeds up the degradation process: subjecting the solution of [Fe] = 2 mM at 60°C for two hours allowed it to reach the same maximum level of degradation as that observed at room temperature over the course of 22 hours. Next, the effect of the pH was assessed. Solutions of nanoparticles at [Fe] = 2 mM] and [Citrate] = 4 mM were prepared at a pH ranging from 4 to 6.5. These solutions were left at room temperature for 22 hours to reach their maximum degradation and showed that low, acidic pH increased nanoparticle degradation at room temperature, with up to a quarter of the degradation taking place at pH = 5.5 and saturation reached around pH = 4.5 (**Figure 2B**). These comparative results suggest that the chelating agent and an acidic pH were necessary and even governed the maximum amount of nanoparticle that can be degraded. Selecting this last condition of [Fe] = 2 mM] and [Citrate] = 4 mM, we then proceeded by subjecting the solution to increasing temperatures between 4°C and 60°C over the course of two hours (**Figure 2C**). This highlighted the effect of heating on degradation, reaching 47% after 30 minutes to 80% after two hours at 60°C compared to 15% after 30 minutes and 30% after two hours at 37°C, or 6% after 30 minutes to 12% after two hours at room temperature. Indeed, high temperature in solution accelerated the degradation process, with the effect being more efficient during the first minute of exposure. The degradation can be visually observed, as the solution's color becomes clearer as the nanoparticles degrade (**Figure 2D**).

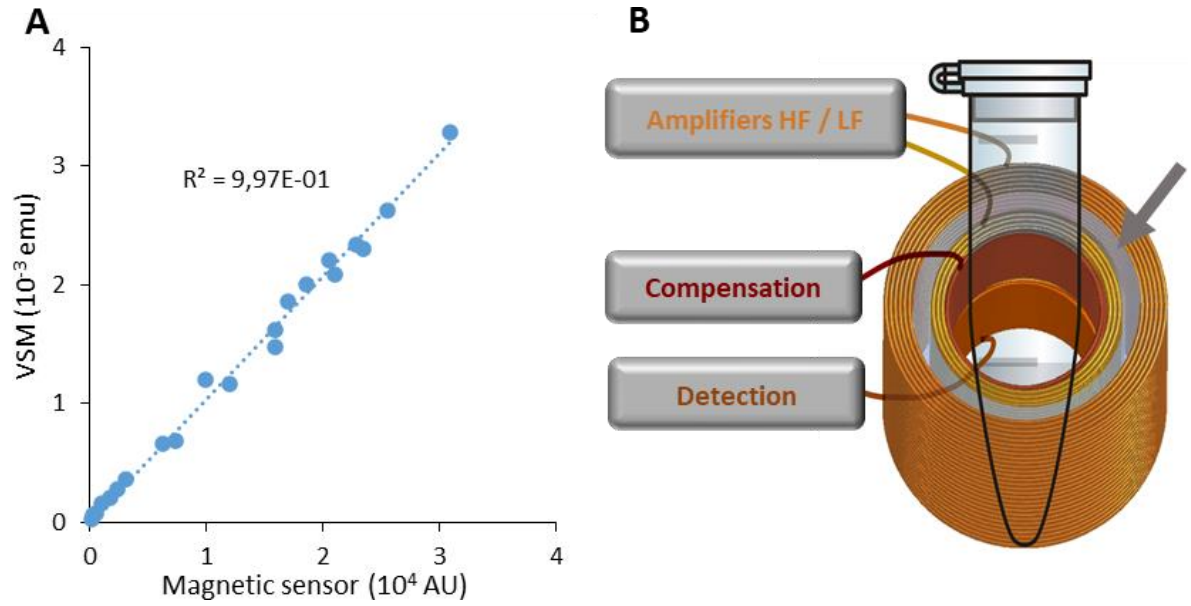

Figure 1: *Using a Custom magnetic sensor to easily assess magnetism and use it as a fingerprint of the nanoparticle degradation process. (A) Correlation between the custom magnetic sensor signal and the magnetic moment obtained via magnetometer (VSM), highlighting a strong correlation ($r^2 > 0.99$) for the magnetism measurement of an 8 nm iron oxide nanoparticle coated with citrate in water. (B) Schematization of the Custom magnetic sensor used for the measurement.*

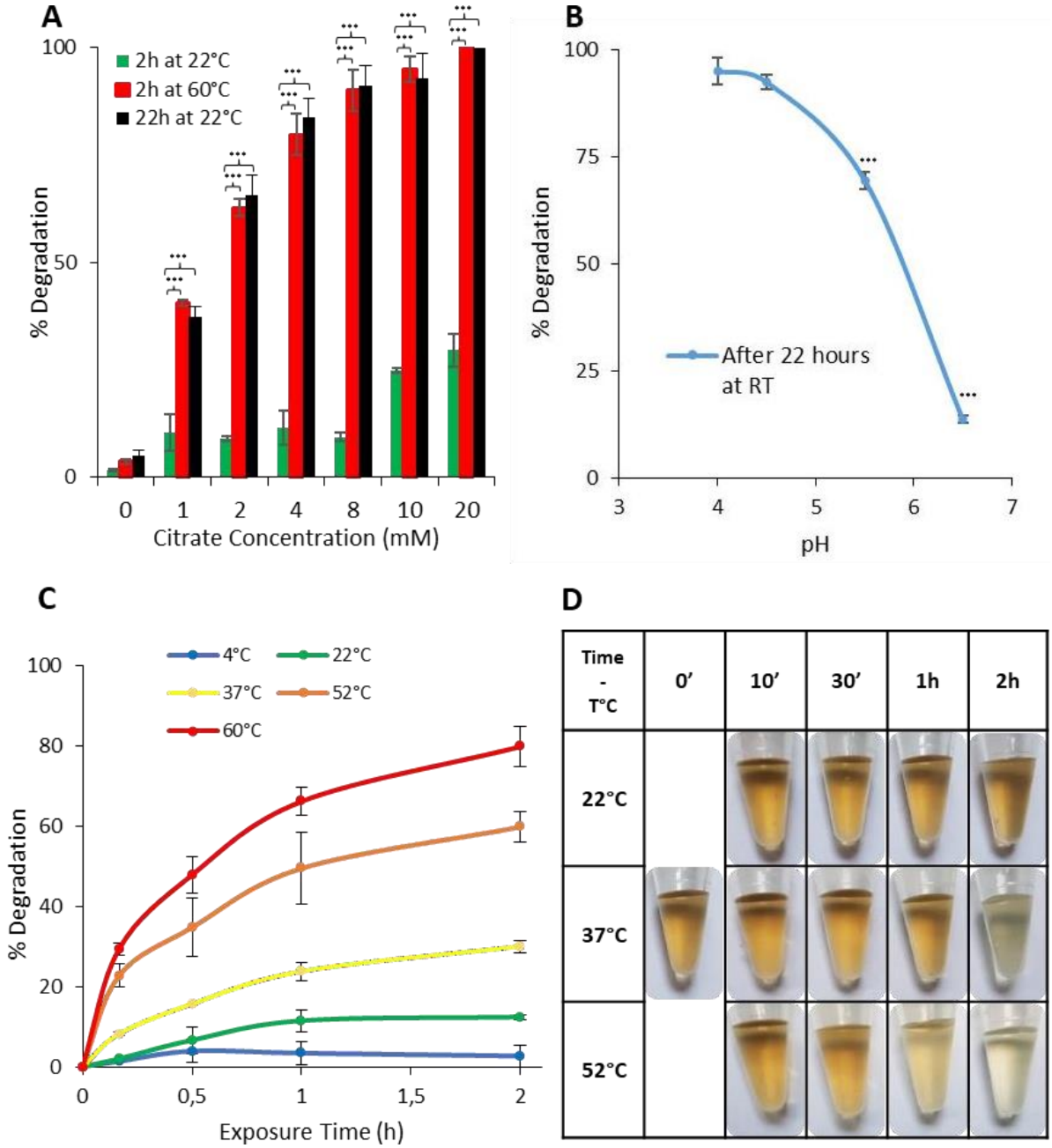

Figure 2: *Study of the environment required for nanoparticle degradation. Degradation was assessed in a lysosomal-like solution with low pH and containing iron chelating agent. (A) Average degradation of the lysosomal-like solution with a pH 4.5 with nanoparticles at [Fe] = 2 mM with varying amount of iron chelating agent at different temperatures. (B) The [Fe] = 2 mM and [Citrate] = 4 mM condition was selected to study the effect of pH on degradation at 22°C for 22 hours. (C) Nanoparticle degradation in lysosomal-like solution subjected to increasing temperature. Images show the solution becomes clearer following the degradation with increasing exposure time and temperature. (D)*

3. Photothermal capability of iron oxide nanoparticles under photothermal irradiation

Iron oxide nanoparticles have been widely used in biomedical research for their versatile magnetic properties, biocompatibility, biodegradability, and good performance as nano heaters in the NIR region[83,84]. Indeed, some reports have exploited these optical properties, resulting from electronic transitions localized in the NIR absorption spectra. Other synthetic or biogenic nanostructures were already used in the NIR-I region (650 - 950 nm) for their photothermal response after an excitation in this range[36]. (The optical properties of synthesized nanoparticles were analyzed by ultraviolet visible (UV-Vis) spectroscopy and exhibited an optical absorbance even at low concentration (1 mM). Additionally, the absorption band was 2-fold higher for magnetite compared to maghemite in the NIR-I region.)

To probe their heating capability, magnetite (Fe_3O_4) and maghemite (γ-Fe_2O_3) nanoparticles were diluted in water at concentrations ranging from up to [Fe] = 320 mM and exposed to an 808 nm laser line at 1 W/cm². We used an infrared (IR) thermal camera to reveal the heating properties of both these types of nanoparticles, with results showing a correlation between the iron concentration and heating potential (**Figure 3**). Magnetite nanoparticles exhibited a higher efficiency, with temperature saturation around [Fe] = 40 mM compared to [Fe] = 80 mM for the maghemite ones. It is known that these optical heating properties depend on multiple physical characteristics, such as size and shape of the magnetic core or the crystallinity[80,95], which could explain the difference between our magnetite and maghemite nanoparticles, since iron (III) based synthesis presented a less disordered structure. Another belief would be the remaining presence of non-oxidized iron (III) at the core of the maghemite nanoparticle. However, the use of iron oxide nanoparticles for their optical-based heating ability in therapy remains recent and heat transfer is not well understood.

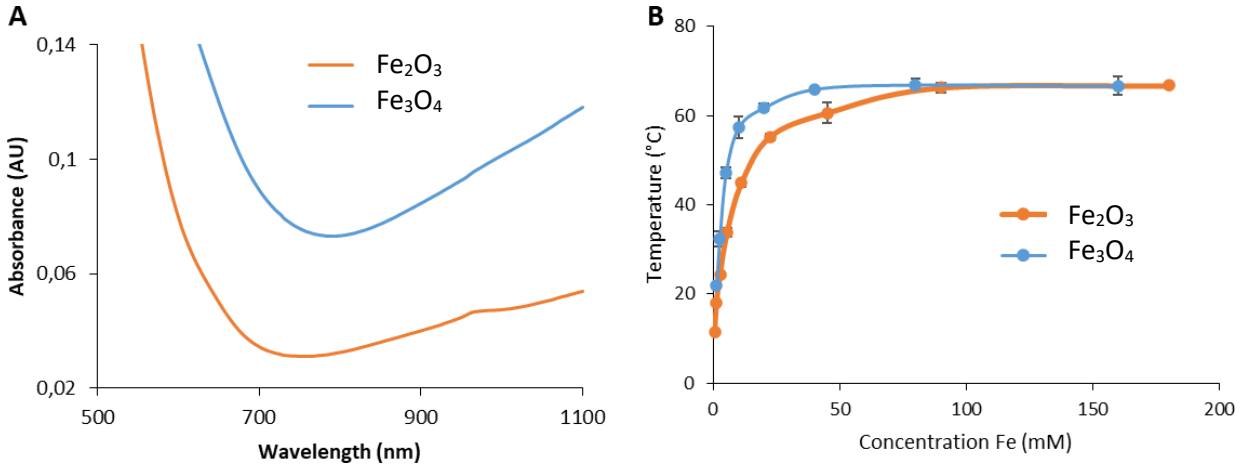

Figure 3*: Photothermal properties of magnetite and maghemite nanoparticle. (A) UV-Vis spectra of an aqueous solution of maghemite and magnetite nanoparticles at [Fe]=1mM, respectively. (B) Heating induced by an 808nm laser irradiation at 1W/cm² for 5min for both nanoparticle,with varying iron concentration.*

4. Photothermal effect on nanoparticles and a new approach to estimate the induced local temperature

We then subjected a [Fe] = 2 mM magnetite nanoparticle solution to different photothermal power densities to quantify their heating capability and, as expected, temperature saturation increased proportionally to photothermal power density (**Figure 4A** and **Figure 4B**). However, this heating profile is not totally accurate since it was made by measuring the global temperature of the solution, while the local temperature at the nanoparticle level is significantly different from the surrounding one (**Figure 4C**) [36,86]. Indeed, MHT and PTT proved having a local heating near the surface of the nanoparticle[42,85,86,87,88,89,90,91]. It remains challenging to quantify the surrounding temperature of the nanoparticle yet attempts have been made using probes attached to the nanoparticle's surface like luminescent molecular thermometers[40], thermo-responsive decomposition or fluorescent molecules[41] or X-ray absorption spectroscopy[22]. Here, we developed a novel, simple and original way to assess this information, using the effect of temperature on degradation. We set a calibration curve of nanoparticle degradation in function of the temperature of a [Fe] = 2mM magnetite nanoparticle solution and [Citrate] = 4 mM at pH = 4.5. This solution was placed in a controlled global heating for 30 minutes to ensure the same global temperature profile. Magnetism was measured before and after exposure, working as a marker of nanoparticle degradation.

Similarly to our previous results, degradation was increased for higher temperature of exposure. We then set the heating profile of this solution under photothermal irradiation for 31 minutes by measuring global temperature via an IR camera, varying laser power. The

additional exposure time of one minute was due to the time needed to reach saturation for this heating condition. We obtained a higher degradation rate under photothermal irradiation for the same global temperature reached (**Figure 4D**), the difference increasing at higher laser power (**Figure 4E**). Using the two degradation and temperature profiles of the two outlined methods (photothermal irradiation and controlled global heating), we calculated the local nanoparticle temperature induced by photothermal irradiation by comparing the degradation rates, with the local temperature induced by photothermal heating being equal to the controlled global temperature applied needed to reach the same degradation rate. At low laser power, local temperature was 5°C higher and increased up to 15°C at higher laser power. This is a simple approach to measure the local temperature without using external equipment, although sacrificing some level of accuracy: obtaining a 1.2-fold increase compared to the 1.5-fold increase previously reported for iron oxide nanoparticles under 808 nm photothermal irradiation[22]. This opens up the opportunity to trigger temperature "hot spots" for possible therapeutic use as it can trigger effective cellular damage[92].

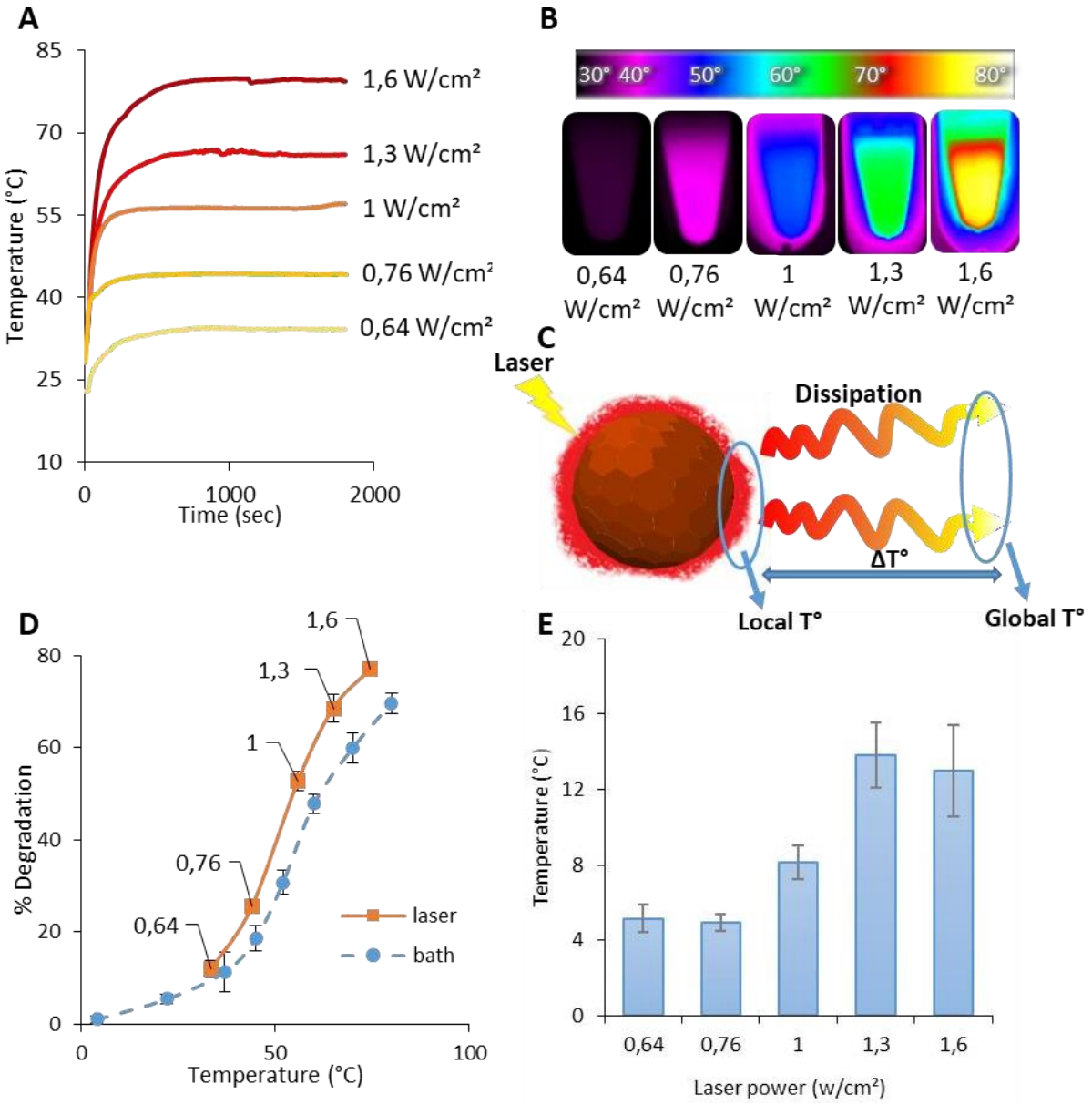

***Figure 4**: Projection of the local heating around nanoparticles deduced from the global heating mediated degradation. (A) Temperature increase profile of a nanoparticle suspension at different photothermal power densities (808 nm). (B) Corresponding typical IR images after 31 min of photothermal irradiation. (C) Schematization of local photothermal heating compared to global heating measured. Heating bath allowed a controlled increased global temperature solution when photothermal-induced local heating at the nanoparticle level, and the diffusion in the solution is the global temperature measured on camera. (D) Degradation as a function of global temperature and different irradiation power densities. Increasing temperature made degradation occur faster. For the same temperature reached, solutions under photothermal irradiation were more degraded, meaning a higher local temperature. (E) Difference between the temperature under laser and the global temperature needed to reach the same amount of degradation.*

5. Controlled location after nanoparticle internalization in a tumor spheroid model

Based on our obtained nanoparticle degradation data, we established a 3D glioblastoma spheroid model to study the degradation environment after nanoparticle internalization by the cells. Tumor spheroids have been widely used as a model for therapeutic research, as they provide a better replication of the microenvironment and signaling cascade due to establishment of connection cell-cell, cell-matrix that mimic *in vivo* more accurately compared to 2D models[93,94,95,96]. Despite the non-favorable electrostatic[97,98] interaction between the both negatively charged citrate-coated nanoparticles and the cell membrane, internalization of the nanoparticles still occurs via non-specific endocytosis in a fast and efficient manner[99].

Our spheroid model consisted of 400,000 cells aggregated in an initial cell pellet through centrifugation and allowed to mature for two days. Spheroids were incubated in a [Fe] = 10 mM magnetite nanoparticle solution with [Citrate] = 20 mM for 30 minutes at 4°C. These conditions were selected to slow down the internalization process, so nanoparticles will be at the beginning of the uptake pathway, i.e. at the cell membrane interface, at the end of the incubation. Then, the spheroids were washed and placed at 37°C. Subsequent incubation time was tuned to control the location of the nanoparticles within the endocytosis pathway, at a maximum of four hours: at less than 30 minutes to localize the nanoparticles at the cell membrane or in early endosomes, or between two to four hours to localize the nanoparticles within endosomes or late endosomes (**Figure 5**). To confirm these assumptions, iron staining of spheroid tissue histological sections and transmission electron microscopy (TEM) imaging were performed to observe our samples at both of these incubation time conditions. After the 30 minutes incubation, iron was detected at the cell membrane, on the edge of the spheroid (**Figure 6A**) and nanoparticles were clearly identified at the membrane and in early endosome near the cell membrane (**Figure 6B** and **Figure 6C**). On the other hand, spheroids incubated at four hours showed iron located deeper into the spheroids (**Figure 6D**) and nanoparticles accumulated mostly in endosomes, with none observed at or near the cell membrane (**Figure 6E** and **Figure 6F**).

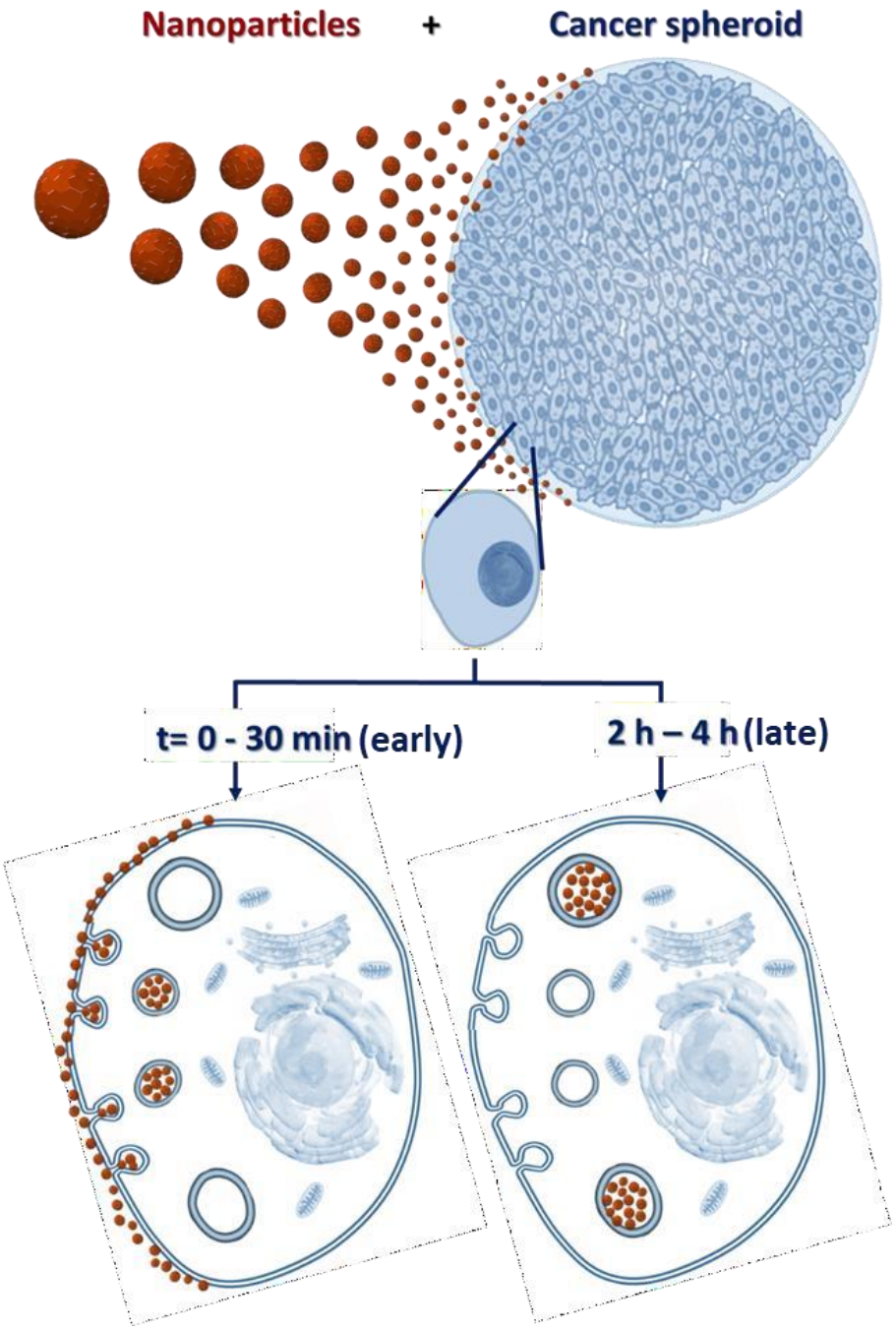

***Figure 5**: Theorical incubation protocol to locate nanoparticles in different compartment during cell iron uptake in a U87 tumor spheroid model. (A) Nanoparticles were internalized by the spheroids by a simple initial nanoparticle interface procedure at 4°C followed by a washing and then a controlled incubation under two different intervals time at 37°C (0 to 30 minutes and two hours to 4 hours).*

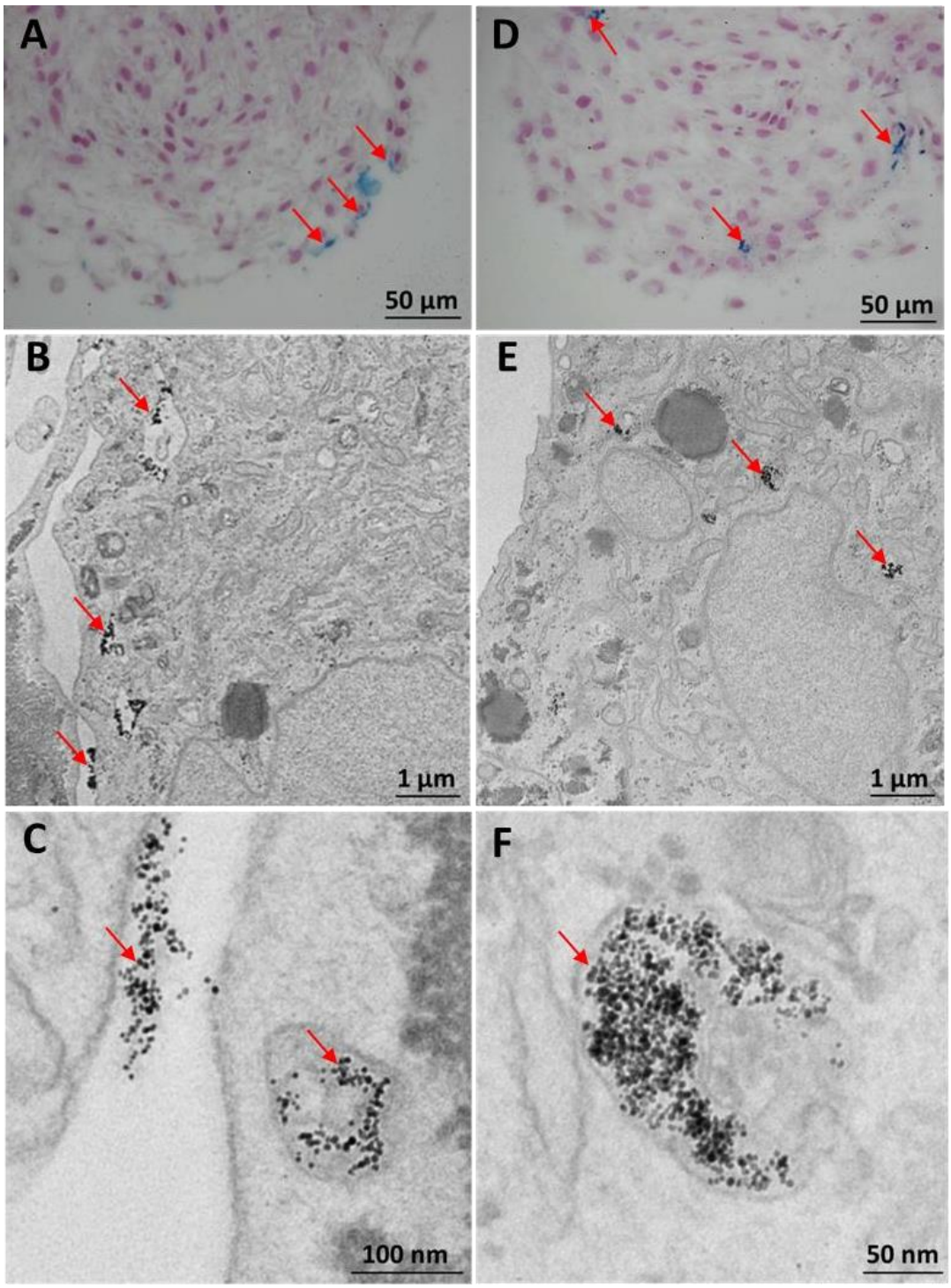

Figure 6: *Study of the intracellular environment and nanoparticle location in U87 tumor spheroid models. (A) PERLS staining showing the presence of iron near the cell membrane for spheroids incubated with nanoparticles for 30 minutes at 37°C and (B-C) TEM imaging for the same incubation conditions. (D) PERLS staining showing the presence of iron deeper into the spheroid tissue after incubation between two and four hours. (E-F) Confinement of nanoparticles in cell endosomes and late endosomes evidenced by TEM imaging.*

6. Nanoparticle degradation *in cellulo* and *in situ* through thermal therapy

In addition to their biological relevancy, spheroid models are useful for distribution, diffusion and heat dissipation studies, making them robust models for phototherapy[100]. **Figure 7A** shows our experimental setup for phototherapy application to our spheroid tumor models. Following the previous incubation method (**Figure 5**), the spheroids were irradiated at a power density of 1.6 W/cm^2 for 31 minutes. The power applied was selected to reach the temperature range for hyperthermia (42 - 45°C)[101]. We measured the global temperature around the spheroids, and remarkably, the heating profiles were similar for all conditions, reaching saturation at 43 - 44°C, highlighting that nanoparticle location in the cell did not impact this parameter (**Figure 7B**). We then proceeded to measure the magnetism of each spheroid via Custom magnetic sensor, before and after photothermal heat application. We observed a significant difference in the percentage of degradation between heating with a global heating source (water bath) and with the more localized photothermal heating, with the latter showing a consistently higher degradation regardless of the location of the nanoparticles in our tumor spheroid model (**Figure 7C**). Remarkably, the later stages of the endocytosis pathway are more favorable environments for degradation. We also verified by ICP that spheroids presented no significant variation in internalized iron, even between conditions and after the heating treatment, evidencing no nanoparticle loss (**Figure 7D**).

Cell viability of the spheroids was assessed using a live/dead cell assay and calculated via cell counting and fluorescence imaging. Cell viability was higher for controlled global heating, at 86% and 74%, compared to photothermal application, at 64% and 61%, for both a 30 minutes and 4 hours application, respectively (**Figure 8A** and **Figure 8B**). This could be explained by photothermal irradiation involving local heating that was much higher than the global heating measured, which was already in the hyperthermia range (42 to 45°C[101]), therefore inducing a higher level of apoptosis and/or necrosis. In the case of the early endosome condition, cell death could additionally be explained by local heating inducing disruption of the cellular membrane where nanoparticles are located. Meanwhile, nanoparticles are packed in endosomes for the late endosome condition. However, the higher degradation observed could induce other cytotoxic responses, such as ferroptosis as iron II is released[102,103,104].

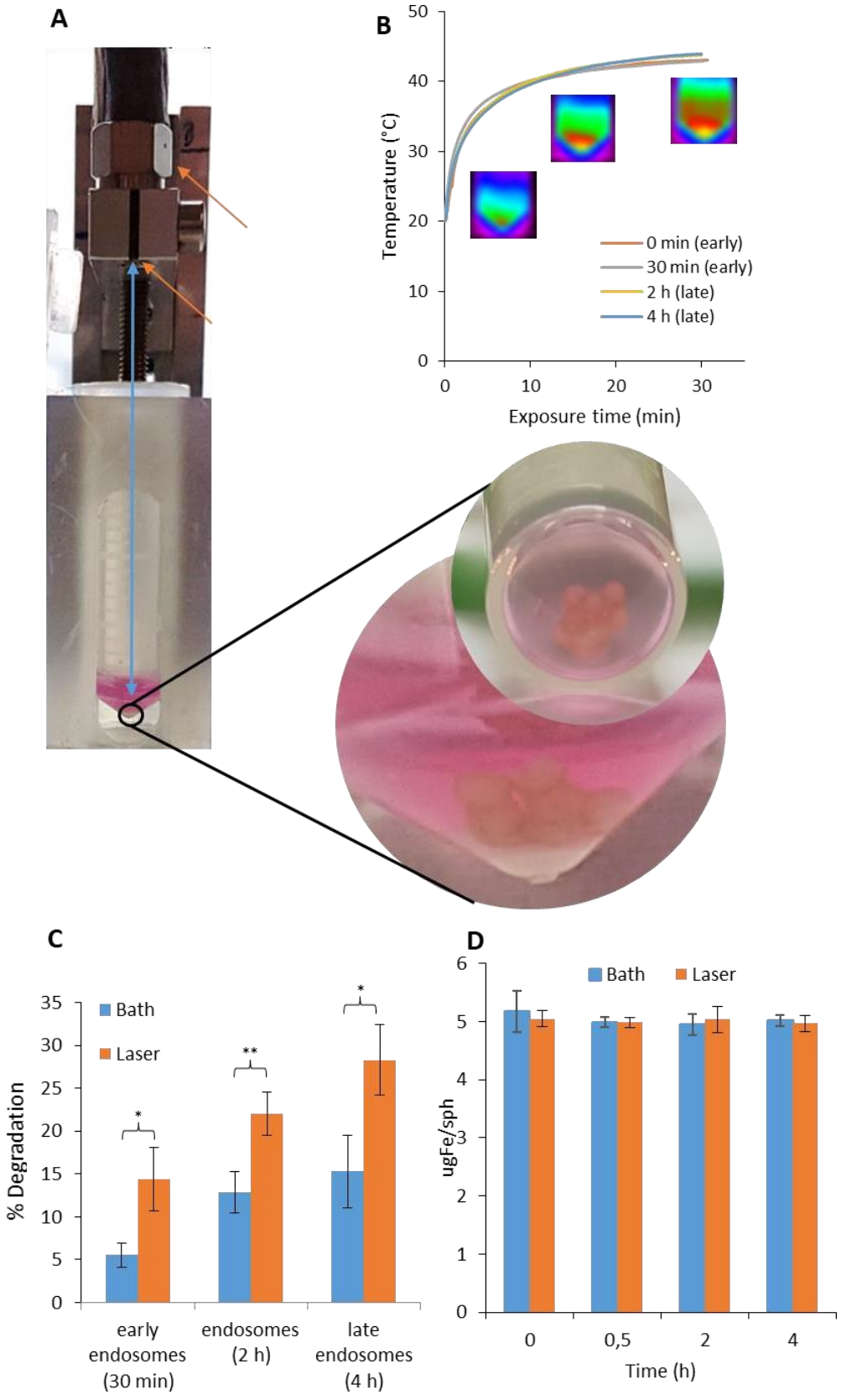

Figure 7: *Nanoparticle's degradation induced by laser application in U87 Spheroid. (A) Experimental setup for photothermal application. (B) Heating profile of spheroids as a function*

of time, for a power density of 1.6 W/cm² applied during 31 minutes, with differential nanoparticle internalization time. Insets show corresponding thermal profiles, as obtained by an IR camera. (C) Average nanoparticle degradation after 31 minutes at 42°C, depending on their apparent intracellular location. (D) Quantitative Iron quantity measured after Photothermal treatment at different maturation time and compared to the control without laser (0h), highlighting there is no significant nanoparticle loss therefore loss of magnetism is due to degradation.

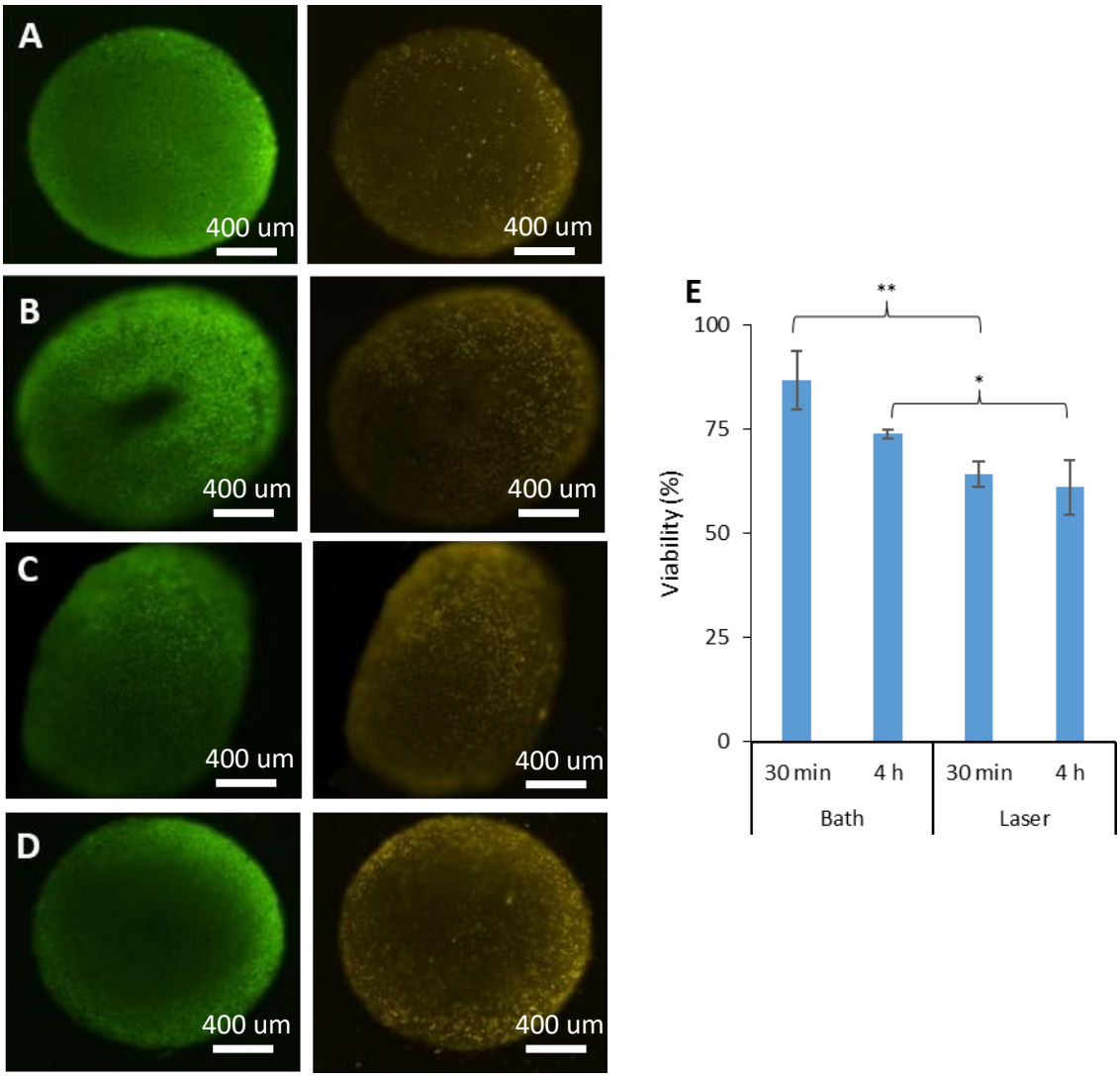

Figure 8: *Impact of hyperthermia and nanoparticle's degradation on cell viability in a tumor spheroids. (D) Composite fluorescence images illustrating the cytotoxicity of the heating treatment. Images show live green (left) and dead red (right), for the controlled global heating condition after 30 minutes (A) and 4 hours (B), and under photothermal irradiation after 30 min (C) and 4 hours (D). (E) Alamar blue quantifying cellular activity as an image of a spheroid viability for the same conditions.*

7. Cytotoxicity and iron (II) release after nanoparticle degradation upon photothermal irradiation

In addition to the photothermal Cell death induced by laser exposure, the forced degradation of nanoparticles by the same laser exposure could provide an additive strategy for cancer therapy through the subsequent induction of a cell cytotoxic response through ferroptosis due to the release of iron (II) as a degradation product. To test this hypothesis, we used a similar 3D glioblastoma spheroid model with some slight modifications. We implemented a system of agarose wells made with a 3D printed stamp with a set of micropillars of 200 µm in diameter and 200 µm in height (**Figure 9A**). This produced spheroids with an average diameter of approximately 200 µm after seeding and a centrifugation step (**Figure 9B**). This spheroid fabrication design was followed in order to ensure a thorough photothermal irradiation across the model tissue in a high-throughput and quantifiable manner. Additionally, the cells were pre-labeled with magnetic nanoparticles before spheroid formation to guarantee a late endosome localization of the nanoparticles, given that a higher degradation was observed for this condition under photothermal irradiation (**Figure 7C**).

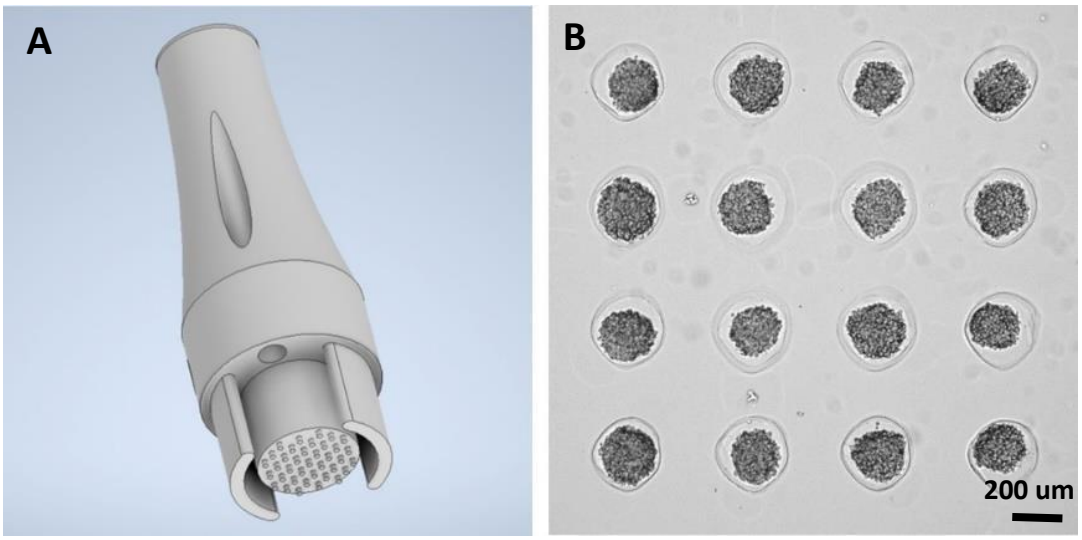

***Figure 9**: Agarose microwell patterning for high-throughput spheroid formation. (A) 3D printed stamp with micropillars used to pattern agarose wells inside a 96-well plate for spheroid formation. (B) U87 glioblastoma cells grown in the microwells for two days, starting from 10,000 cells per well.*

We thus proceeded to evaluate the cytotoxicity induced by photothermal irradiation on this spheroid model using the live/dead cell fluorescent assay. Two sets of nanoparticles were tested: magnetite (Fe_3O_4) and maghemite (Fe_2O_3). The latter were included because

their oxidation state does not allow the release of iron (II). These nanoparticles are obtained via a harsh oxidation of the magnetite ones, leading to a differential core composition, yet possessing the same average size and citrate coating, and thus a similar cell internalization profile can be expected. **Figure 10** shows typical fluorescently stained live and dead U87 spheroids after a five minutes photothermal irradiation. No red dead signal is observed for the control group, where most of the spheroids showing a bright green signal, indicating highly metabolically active cells. An inverse scenario is observed for the photothermal irradiation condition, with all the spheroids being stained only by the red fluorescent dye, highlighting the cytotoxic potential of PTT.

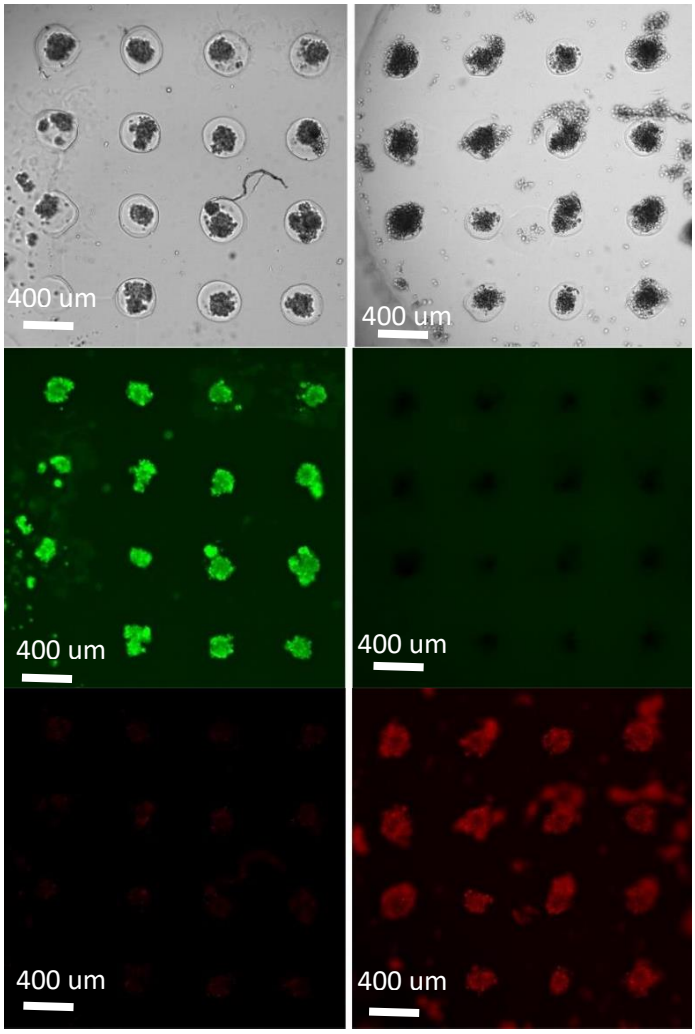

***Figure 10**: Typical live/dead imaging sequence of U87 glioblastoma spheroids under photothermal irradiation. U87 spheroids at one day maturation (10,000 cells per well) after incubation with the magnetite nanoparticles. The left column shows the control condition (no photothermal irradiation), whereas the right column shows spheroids subjected to a 2.6W/cm² photothermal irradiation applied during five minutes. Top row: bright field; middle row, live green fluorescent signal of calcein; bottom row: dead red fluorescent signal of propidium iodide.*

The live/dead fluorescent staining and imaging procedure was followed for increasing photothermal power density conditions and for both the magnetite and maghemite nanoparticle formulations. The quantification of the fluorescent intensity for each of these conditions is shown in **Figure 11**. A relatively low live green fluorescent signal was observed for spheroids with cells labeled with maghemite nanoparticles irradiated at a power density of 2.6W/cm² and compared to the control group (no irradiation). Similarly, low live green signals were observed for magnetite-labeled spheroids irradiated either at 1.6W/cm², 2.1W/cm² or 2.6W/cm². Remarkably, a clearly pronounced increase of the red dead signal was induced by irradiation of the magnetite nanoparticles, with a proportional increase in relation to an increase in power density.

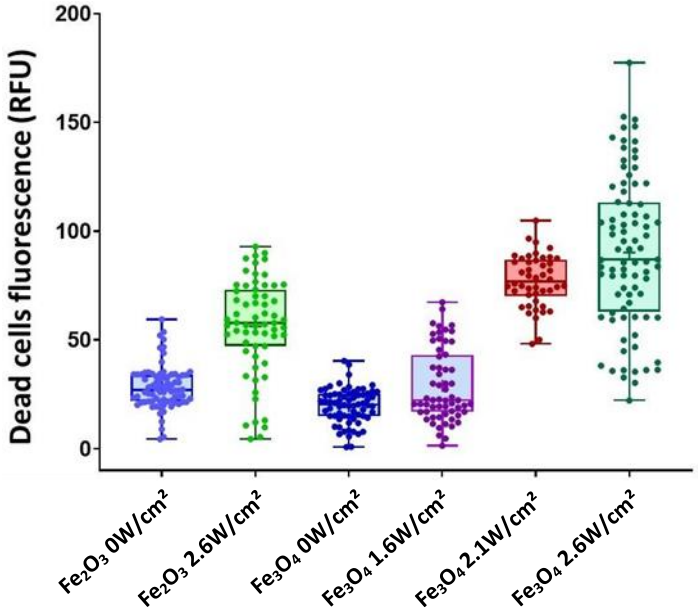

***Figure 11**: Dead red fluorescent signal quantification in magnetically labeled U87 glioblastoma spheroids under photothermal irradiation. Box plots show the live green and dead red signal quantification for U87 spheroids made of cells labeled with either magnetite (Fe_3O_4) or maghemite (Fe_2O_3) nanoparticles and exposed to photothermal irradiation (808 nm) at power densities of 1.6W/cm², 2.1W/cm² or 2.6W/cm². n = 200 spheroids per condition on average.*

Lastly, we proceeded to quantify the presence of iron (II) under the same experimental irradiation conditions. We used a FerroOrange live cell fluorescent dye that specifically detects free iron (II) ions. The dye is not sensitive to the presence of iron (III), other bivalent metal ions, or chelated iron stored in ferritin, and thus allows us to observe any possible nanoparticle degradation products released inside the cells. **Figure 12** shows typical fluorescent images of U87 spheroids loaded with magnetite nanoparticles after photothermal irradiation and subsequent FerroOrange staining. No FerroOrange signal was detected on the negative

control group of spheroids, whereas a clear increase in fluorescent signal can be observed as the irradiation power density increases due to increased degradation. This indicates that photothermal irradiation results in the release of iron (II) ions from the magnetite nanoparticles, possibly as an oxidative effect after heat degradation.

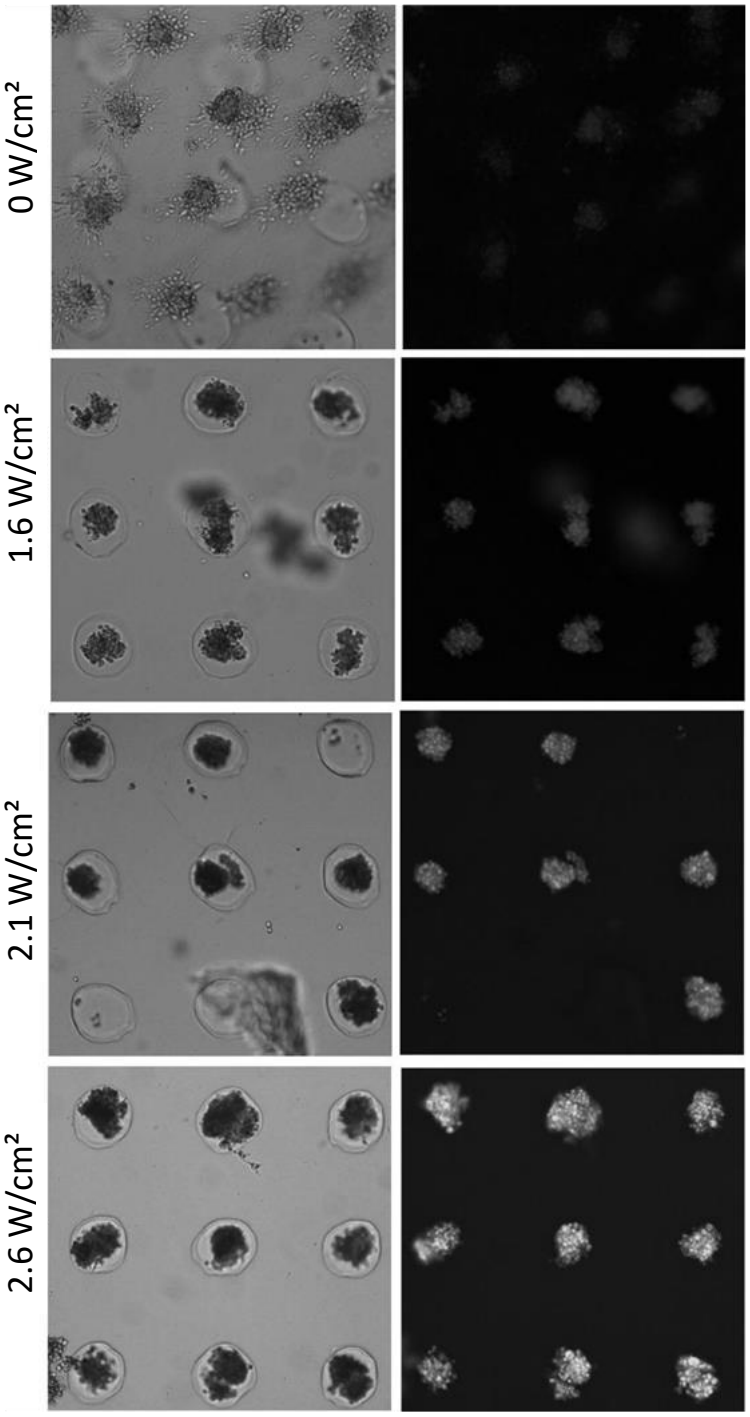

***Figure 12**: FerroOrange iron (II) fluorescent imaging. Images show U87 glioblastoma spheroids loaded with magnetite (Fe_3O_4) nanoparticles after a five minutes photothermal irradiation at increasing power densities. Left column images show bright field settings, whereas the right column shows the FerroOrange fluorescence channel.*

The FerroOrange fluorescent quantification of all the experimental conditions is shown in **Figure 13**, up to 2.6W/cm² for a rapid degradation. Irradiation of spheroids with maghemite nanoparticles resulted in a very low release of iron (II) ions. This is an expected response, as the iron present in these nanoparticlesis almost totally oxidized. On the other hand, the iron (III) present in the magnetite nanoparticles does degrade and release iron (II) ions upon photothermal irradiation, with an increasing dose-response relationship. Overall, these results confirm that the cytotoxicity observed under the same irradiation conditions (**Figure 11**) is correlated with the release of iron (II) ions after photothermal irradiation and is likely an iron (II)-mediated ferroptosis response mediated via nanoparticle degradation upon heat exposure.

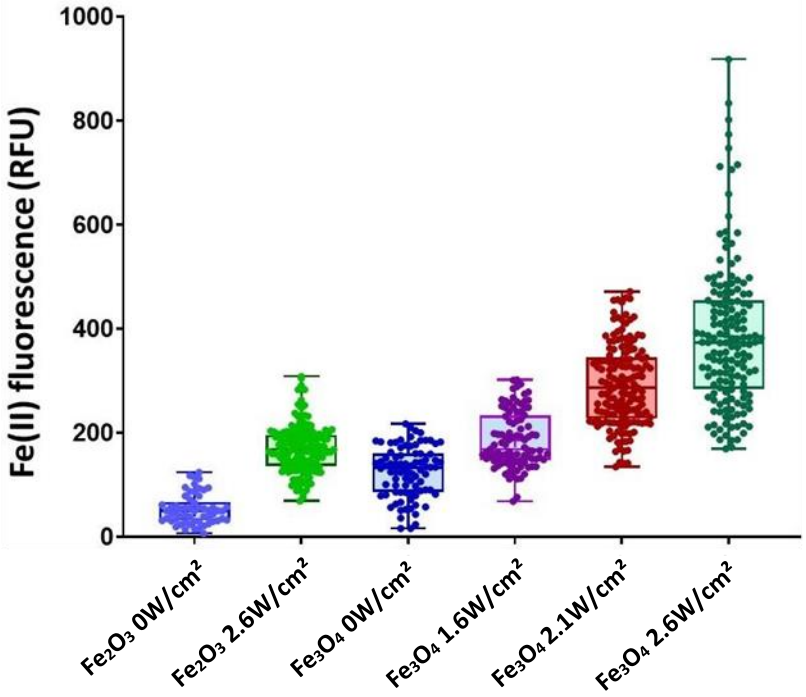

Figure 13 *: FerroOrange iron (II) fluorescent quantification. The release of iron (II) is only incurred by U87 glioblastoma spheroids labeled with magnetite (Fe_3O_4) nanoparticles after photothermal irradiation. n = 200 spheroids per condition on average.*

Conclusion

Here, we show the conditions needed for iron oxide nanoparticle degradation by implementing a model of a low pH medium with an iron chelating agent, also allowing to get a glimpse of the environment that the nanoparticles are exposed during internalization. We followed nanoparticle degradation *in cellulo* using the magnetism of the nanoparticles as a

footprint. This degradation is accelerated with high temperature exposure which allows a short-term control over it. By exploiting the photothermal properties of iron oxide nanoparticles, we were able to draw a heating profile of the local temperature induced by irradiation via the control of the degradation by the temperature exposure. This method allows a quick and easy estimation of the temperature at the nanoparticle level. Overall, it allows a double therapy with PTT inducing hyperthermia coupled with ferroptosis induced by the release of iron ions from the magnetite nanoparticle's degradation. Indeed we showed nanoparticle degradation induced by photothermia result in the release of iron (II) ions cytotoxic.

Materials and methods

1. Magnetic nanoparticles synthesis

Magnetic nanoparticles were synthesized via microwave-assisted synthesis. Briefly, 400 mg of iron (III) acetylacetonate (> 99.9%) (Sigma Aldrich) were dissolved in 10 mL of benzyl alcohol anhydrous (99.8%) (Sigma Aldrich) within a 30mL monowave glass vial and placed in a monowave 300 from Anton Paar. The temperature of the suspension was increased up to 250°C in 20 minutes and then maintained constant for 30 minutes. The resulting suspension was precipitated using a neodymium magnet and the precipitate was washed successively with dichloromethane, sodium hydroxide (1M), ethanol and pH = 7 water (three times). A last washing step was performed in acidic water (pH 2) and the nanoparticles were separated by ultracentrifugation using Amicon® ultra centrifugal filters (30 kD) at 2200g during 10 minutes. Finally, the magnetic nanoparticles were resuspended in acidic water (pH = 2) for further coating. Iron oxide nanoparticle majorly formed in magnetite (Fe_3O_4) were obtained. To obtain maghemite (Fe_2O_3) nanoparticles, a fraction of the previous batch was oxidized by heating the solution at 80°C with ferric nitrate under magnetic stirring for 30 minutes. X-ray diffraction (XRD) and a vibrating sample magnetometer (VSM, Quantum Design Versalab) were used to determine the oxidation state of the iron nanoparticle solution.

2. Nanoparticle coating

Citric acid (Sigma Aldrich) was used in excess with a mass of citrate five times higher than the mass of nanoparticles and was dissolved in water at pH = 2. The coating molecule solution and nanoparticle dispersion were mixed and left to agitate for two hours under stirring. The pH was then adjusted to 7 with sodium hydroxide at 1 M and left for two hours to equilibrate. Finally, nanoparticles were magnetically sorted three times in water (pH = 2), using a neodymium magnetic disc, then ultra-centrifuged with deionized water at pH = 7 in Amicon® ultra centrifugal filters (30 kD) during 10 minutes at 2200g.

3. Aqueous solutions for degradation experiments in suspension

Degradation was assessed in a solution with similar lysosomal conditions. Magnetic nanoparticles were mixed in a solution buffer with acidic conditions (with pH ranging from 4 to 6,5) and an iron chelating agent (citrate, from 1 to 20 mM) to be at a final concentration of [Fe] = 2 mM of iron oxide nanoparticles.

4. Magnetization measurement

Magnetization was then measured by a custom magnetic sensor developed by Magnisens SA for diagnostic tests. The analysis is based on the non-linear superparamagnetic magnetization of the nanoparticle. Briefly, an alternating magnetic field is applied to the sample at two different frequencies: f_1 = 100 kHz and f_2 = 100 Hz and amplitudes of 10 and 200 Oe for both, respectively. The signal measured represents the third derivative of the sample magnetization at zero magnetic field at room temperature, proportional to the amount of nanoparticles within the sample. This custom magnetic sensor had previously showed strong correlation between the custom magnetic sensor signal of the nanoparticles and their VSM magnetic moment. It allows us to follow the integrity of the nanoparticles, indeed the decrease of the signal of the sample corresponds to degradation. However, the method used by the sensor to obtain the signal is dependent of the size of the nanoparticle, and thus the correlation must be redone for each nanoparticle type

5. Laser-induced thermometric measurements

Heating profiles of aqueous solutions were obtained by placing suspensions of 50 µL of magnetic nanoparticles diluted in lysosomal-like solution at [Fe] = 2 mM in a 0.5 mL Eppendorf tube, and a working distance of 4.5 cm between the laser source line and the liquid surface. Samples were irradiated with an 808 nm laser (Laser Components) at power densities between 0.6 to 1.6 W/cm² for 10 minutes to two hours. The increase in temperature was measured in real time using an infrared thermal camera (FLIR A615) and processed with the FLIR ResearchIR software.

For degradation experiments in our spheroid model, eight spheroids were placed at the bottom of a 2 mL Eppendorf tube with 100 µL of culture medium. Spheroids were irradiated at a power density of 1.6 W/cm² for 31 minutes, with all spheroids being directly exposed to the laser.

6. Cell culture and spheroid formation

U-87 MG human glioblastoma cells (ATCC) were cultured in Dulbecco's Modified Eagle Medium (DMEM, Gibco) supplemented with 10% fetal bovine serum and 1% penicillin-streptomycin (Thermo Fisher Scientific) at 37°C in a humidified incubator with 5% CO_2. Upon

reaching 80% confluence, cells were detached using 0,05% trypsin-EDTA (Gibco). 400,000 cells were dispersed in 1 mL of culture medium in a 15 mL Falcon tube and centrifuged at 1100 rpm for five minutes to form a pellet. The pellets were left in an incubator with an open cap for two days to mature and systematically form cohesive spheroids.

7. Nanoparticle labelling

A labeling solution was prepared with nanoparticles diluted at [Fe] = 2 mM in serum-free RPMI culture medium (Thermo Fisher Scientific) supplemented with 5 mM free citrate (to avoid nanoparticle precipitation). Spheroids at day two of maturation were placed in this solution at 4°C under slow stirring every 5 minutes to allow nanoparticles to interact with the entire spheroid surface, and for up to 30 minutes of total incubation. The spheroids were then rinsed thoroughly in serum-free RPMI medium and incubated at different times (up to four hours) in complete DMEM medium at 37°C before further processing to allow nanoparticles to be internalized at different stages of the endocytosis process (from surface/early endosome to endosome/late endosome).

8. Prussian blue staining

Prussian blue staining was used to observe the location of iron in cells. Spheroids were fixed with 4% paraformaldehyde then included in 1.5% agarose deionized water. Spheroids were cut in slices of 7 µm directly from the agarose mold and were stained with Prussian blue (5% potassium ferrocyanide (Sigma) in 10% hydrochloric acid (Sigma Aldrich)) for 35 minutes and counterstained with nuclear fast red (Sigma) for 15 minutes. Hematoxylin and eosin staining was performed by Institute Cochin (France). Images were taken using an Olympus Bx40 optical microscope.

9. Transmission electron microscopy imaging

Spheroids were analyzed under transmission electron microscopy to observe the nanoparticles within the cells at the nanoscale level. The spheroids were washed with cacodylate buffer (0.2 M), then fixed with 5% glutaraldehyde in 0.1 M cacodylate buffer for 30 minutes at room temperature and washed once again in the same buffer. Samples were then contrasted with Oolong Tea Extract (OTE) at 0.5% diluted in cacodylate buffer, post fixed with 1% osmium tetroxide containing 1.5% potassium cyanoferrate and then dehydrated in graded ethanol baths. Samples were then included in Epon epoxy resin, ultra-sectioned (70 nm) and deposited onto cooper grids for observation with a HITACHI HT 7700 electron microscope operating at 120kV (INRA, France). Post-fixation preparation and observations were performed at Institut National de la recherche agronomique (INRA, Plateau MET, Jouy-en-Josas,France).

10. Iron quantification

Total iron content was determined by inductively coupled plasma atomic emission spectroscopy (ICP-AES) (Spectrogreen, SPECTRO, Germany) to discard any possibility of cell death and subsequent iron release from the spheroids. For each measurement, cell number was counted using a Malassez chamber, and samples were digested in 290 µL of 69% nitric acid (Sigma, trace metal basic grade) for two days. The solutions were then diluted in filtered ultrapure water to obtain a final 2% nitric acid solution ready for analysis.

11. Live/Dead Fluorescent staining and visualization

The LIVE/DEAD™ Cell Imaging Kit (R37601, Invitrogen™) was used to assess cell viability in live spheroids. Spheroids at day two of maturation were stained with Live Green/Dead Red staining solution mixed at a 1:2 dilution in complete culture medium in non-adherent dishes for two hours in an incubator at 37 °C, according to vendor's instructions. The spheroids were then imaged using a Nikon Eclipse microscope (Nikon®) coupled with fluorescence and a CoolSnap HQ2 camera (Photometrics), with a 10x and 20x objective. Images were processed using the ImageJ software.

12. Statistical Analysis

All values are presented as mean ± SEM. Significance between two groups was determined using independent Student's t-test, and significance between three or more groups was determined using one-way ANOVA. If ANOVA indicated significance at $p < 0.05$, a Tukey's honest significant post hoc test was performed to compare group means. For all values, a minimum of 95% confidence level was considered significant, with $*p < 0.05$, $**p < 0.01$ and $***p < 0.005$. Number of independent measurements was systematically superior to three ($n > 3$).

13. Spheroid formation using agarose microwells

U87 glioblastoma cells were incubated with [Fe] = 2 mM of either magnetite or maghemite nanoparticles in DMEM cell medium and left overnight in a 37°C incubator. The following day, cells were detached using 0.05% trypsin-EDTA and counted. A 3D printed stamp with micropillars of 200 µm diameter and 200 µm in height was used to print molds into the wells of a 96-well plate containing 50 µL of 2% agarose (A0576, Sigma Aldrich) in PBS. The agarose was then left to solidify between one and two minutes and the stamp was removed, leaving an array of molds in the wells. The 96-well plate was then sterilized in UV light for 30 minutes before cell seeding (10,000 cells per well) and centrifugation. Cells were allowed to mature overnight before photothermal irradiation. Imaging was performed on an EnSight® Multimode Microplate Reader (Perkin Elmer), and the ImageJ software was used for processing the acquired images and for fluorescence quantification.

14. FerroOrange iron (II) fluorescent staining

Iron (II) fluorescent imaging and quantification was perfomed with the FerroOrange fluorescent probe (Millipore BioTracker™ FerroOrange Live Cell Dye, # SCT210), following the specified protocol by the vendor. Before staining, the spheroids were washed thoroughly with washing buffer to remove traces of extracellular iron. The spheroids were then incubated at 37°C for 30 minutes in a 1 µM FerroOrange solution diluted in Hank's Balanced Salt Solution (Thermofisher Scientific). After the incubation, the cells were rinsed twice with washing buffer and placed in observation buffer before imaging with an EnSight® Multimode Microplate Reader. Images were analyzed using the ImageJ software.

CHAPITRE 2 : Photothermie avec des nanoparticules de platine

La recherche sur l'utilisation des nanoparticules comme sources de chaleur est de plus en plus répandue, notamment pour le traitement des tumeurs, car elles offrent une large variété de propriétés exploitables[105]. Parmi elles, l'utilisation de nanoparticules d'or est bien connue car considérée comme l'une des plus efficaces[35,106,107]. Nous avons cependant pu voir que d'autres nanomatériaux, comme les oxydes de fer, pouvaient être des alternatives robustes permettant de nouvelles approches. D'autre nanomatériaux catalytiques ont ainsi vu leur intérêt grandir durant cette dernière décennie, tels que le platine ou le cérium qui possèdent des propriétés physicochimiques de surface uniques et offrent un potentiel d'application accru notamment dans le domaine biomédical : bio imagerie[108-111], détection de molécules biologique[112-114] ou en nanomédecine[115-117].

Le Platine (Pt) fait partie des candidats prometteurs comme photosensibilisateur[118-121] grâce à son nombre atomique élevé (78), car il est capable d'améliorer l'efficacité de la radiothérapie en augmentant l'absorption des énergies de radiation ionique ou d'agent de contraste[122,123].

Le platine est aussi associé au cis-platine[124-128] et les nanoparticules de platine pourraient donc être considérée comme nanoparticule chimio-thérapeutique, pour améliorer les traitements anticancéreux[129-137,143,145]. En effet le cis-platine est un complexe à base de platine [$Pt(NH_3)_2Cl_2$] utilisé dans le traitement de différents cancers (poumons, ovaires, testicules, lymphomes) et qui agit en allant provoquer une variation de la conformation du double brin d'ADN (alkylation de l'ADN), inhibant ainsi la réplication et la transcription de l'ADN, induisant en retour la mort cellulaire.

Cependant, les applications en biomédecine sont toutes soumises à une caractérisation précise de la toxicologie en milieu biologique, et qui n'est pas encore totalement clair pour les nanoparticules de Pt. Même si les nanoparticules de Pt sont déjà utilisées pour des applications thérapeutiques de plusieurs pathologies, sans avoir d'effets néfastes[131-133], nous avons montré que dans certaines conditions, certaines nanoparticules métalliques peuvent relarguer des ions réactifs[138-140] et provoquer une cytotoxicité. Cependant, malgré son association au cisplatine, les nanoparticules de Pt possèdent, comme pour l'or, une haute stabilité en milieu cellulaire acide, démontrant ainsi une cytocompatibilité et une tolérance in vivo. Malgré tout, cette observation reste générique pour ce nanomatériau, puisque le rôle de la taille ou l'impact du recouvrement de surface restent peu connus dans leur rôle sur le devenir de la nanoparticule[135,136,141-145,153-156].

Dans ce contexte, nous avons vu précédemment que l'exposition à un laser pouvait accélérer le phénomène de dégradation, ce qui ferait des nanoparticules de Pt un puissant agent thérapeutique si leur dégradation pouvait également être déclenchée. Cependant, la résonnance plasmonique de ce matériau se situe dans la région UV[146,147], ce qui en fait une nanostructure moins efficace que l'or, la référence en photothermie. Malgré tout, quelques études ont rapporté de possibles applications dans ce domaine[127,128,148,149,150,160].

Ainsi, il a été démontré que la phototoxicité pouvait dépendre de la taille de la nanoparticule, et que l'utilisation de petites nanoparticules de platine, n'ayant pas d'effet toxique intrinsèque, pouvait causer une mort cellulaire une fois irradiées par un laser dans le proche IR[160-162], ce qui en ferait un agent théranostique.

Résultats et discussion

a. Caractérisation de nanoparticules de platine et de leur pouvoir chauffant.

Nous avons donc cherché à intégrer ce nouveau champ d'une possible photothermie avec des nanoparticules de platine. En collaboration avec Erwann Guénin (UTC, Laboratoire TIMR) pour la synthèse des nanoparticules, nous avons étudié deux types de nanoparticules de platine : une forme monocœur, sphérique de 6 nm de diamètre (appelée « small » par la suite), et une autre forme multi-cœur appelée
« nano-framboise » (FRB) d'environ 200 nm de diamètre. La synthèse est basée sur la synthèse multi-cœur de nanoparticules de palladium[151]. Brièvement, une solution de platine est mixée avec un agent réducteur (Ascorbate de Sodium) et à une solution stabilisatrice de biphosphonate (Alendronate) en milieu à pH acide (3) ou basique (10) et cette solution est chauffée pendant 30 min à 100°C sous condition aérobique. En effet, un pH basique de la solution d'Alendronate permet d'obtenir des petites nanoparticules, tandis qu'un pH acide permet l'agglomération des petites nanoparticules entre elles, formant des nano-framboises.

Cette structure originale en nano-framboise a été choisie car dans le cas de nanoparticules d'or, le même type de framboises multi-cœurs ont permis de déplacer l'absorption optique vers l'infrarouge, ces mêmes nanoparticules d'or sphériques permettant aussi une photothermie très efficace[148].

Les solutions ont été soumises à une analyse en XAS afin de déterminer leur état d'oxydation au Pt L3-edge et ont montré que les nano-framboises étaient les nanoparticules les plus oxydées (**Figure 1**), potentiellement dû à la synthèse en milieu acide, et représenté par le décalage de l'intensité. Les petites nanoparticules sont plus proches du Pt métallique[152].

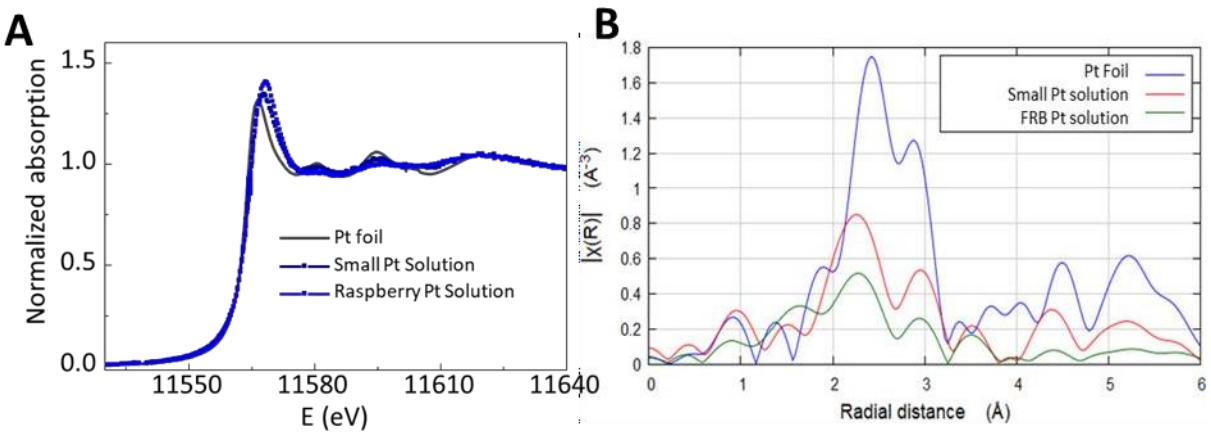

Figure 1: *Microscopie d'absorption des rayons X. Le spectres XAS et XANES ont été mesurés au niveau de la couche L3 de Pt pour caractériser les nanoparticules en les comparant au platine metal (foil). (A) Spectre d'absorption XANES des solutions de petites nanoparticules et des nano-framboises de Pt révélant un état d'oxydation de ces nano-framboises plus élevé. (B) Signal EXAFS des deux types de nanoparticules en solution.*

Ces deux solutions de nanoparticules ont ensuite été soumises à l'application d'une irradiation par un laser de 808 nm à 1 W/cm² pendant 10 min afin de caractériser leurs capacités photothermiques dans cette région proche infra-rouge, pour des concentrations allant de [Pt]= 0 mM à 7 mM. L'augmentation de température a été mesurée à l'aide d'une caméra infrarouge. A noter que l'augmentation de température a tendance à atteindre un plateau à haute concentration.

On observe ainsi un chauffage important en solution même à faible concentration pour les framboises (**Figure 2B**), montrant un fort potentiel en tant que sources de chaleur et une application possible pour la thérapie par photothermie, tandis que les petites nanoparticules montrent au contraire une faible capacité de chauffage (**Figure 2A**). Cela met donc en évidence la capacité de nanoparticules de platine en configuration multi-cœur à provoquer une élévation de température induite par l'exposition d'un laser proche infra-rouge (**Figure 2C**).

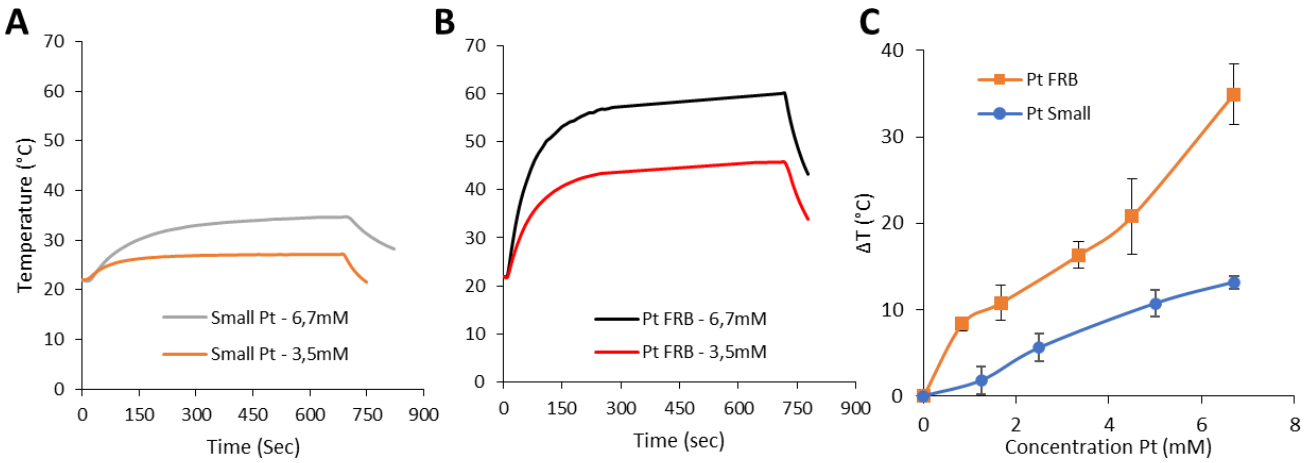

Figure 2: *Mesure de l'augmentation de température des petites nanoparticules monocœur (small) et des nano-framboise multicœur (FRB) dans l'eau. L'élévation de température obtenue sous exposition à un laser de 808 nm à 1 W/cm² et pour des concentrations en Pt de [Pt] = 3,5 et 6,7 mM. Profil de chauffage typique pour de la photothermie, au cours du temps, pour les petites nanoparticules (A) et les nano-framboises (B) et l'élévation de température mesurée au plateau pour des concentrations allant de [Pt] = 0 à 6,7mM (C).*

Afin de pouvoir situer les capacités thermiques de ces nanoparticules parmi d'autres types de nanoparticules, nous avons calculé le taux d'absorption spécifique (SAR) qui représente le pouvoir chauffant d'un matériau exprimé en Watt par gramme de matériel absorbant. Le SAR a été calculé pour des concentrations allant de [Pt] = 0,25 à 2 mM après exposition à un laser de 808 nm et une puissance de 1 W/cm². Les deux types de nanoparticules peuvent ensuite être comparés au SAR obtenus pour de petites nanoparticules et des nano-framboises d'or[149] calculés pour des concentrations d'or comprises entre [Au]= 0,25 et 2 mM.

Les petites nanoparticules de Pt présentent un SAR faible, semblable à celui de petites nanoparticules d'or (**Figure 3A**) tandis que les nanoparticules multicœurs montrent un SAR plus important. A noter que ce SAR reste inférieur à celui des nano-framboises d'or (**Figure 3B**).

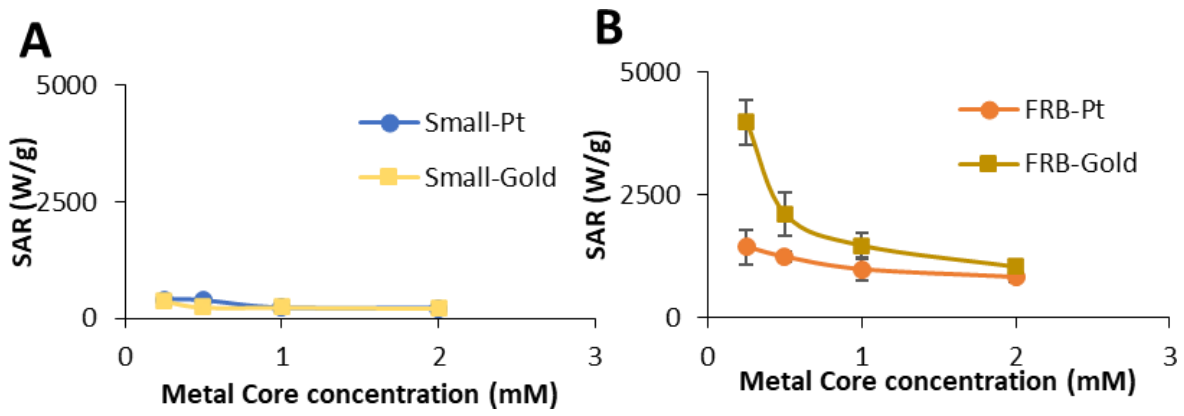

Figure 3 : *Valeurs de SAR de petites nanoparticules mono*cœur (6nm) *et de nano-framboises multi*cœur *de platine et d'or dans l'eau, en fonction de la concentration en métal absorbant ([Pt] et [Au]) après une irradiation à un laser de 808 nm à 1 W/cm².*

b. Impact de l'internalisation des nanoparticules de platine sur le pouvoir chauffant : rôle du confinement dans les endosomes.

Dans l'optique d'utiliser ces nanoparticules de Pt en thérapies thermiques, ces agents doivent être testés en milieu biologique, au cœur des cellules cancéreuses, cibles de la thérapie. En particulier, il s'agit d'évaluer non seulement leur capacité à être internalisées par les cellules, mais également la conservation (ou l'augmentation) de leurs capacités de chauffage en environnement intracellulaire. En effet, pour les nanoparticules de platine mono-cœur, dont le pouvoir thermique en solution est faible, on pourrait s'attendre à ce que le confinement endosomal augmente leurs capacités de chauffage, comme c'est le cas pour de petites nanoparticules d'or[153,154].

Les nanoparticules de Pt ont donc été incubées avec des cellules cancéreuses de glioblastome (U87) à des concentrations entre [Pt] = 0,2 et 1,25 mM pendant 24 h menant à des concentrations intracellulaires allant de 0,1 à 1 pg de Pt par cellule. 200000 cellules sont ensuite agrégées par centrifugations et laissées maturées en eppendorf, en milieu complet, pendant 2 jours, pour former un sphéroïde, modèle tumoral 3D clos[95].

Tout d'abord, nous avons vérifié que les deux types de nanoparticules de Pt suivaient bien la voie d'endocytose, et nous les avons localisées dans les endosomes par microscopie électronique en transmission TEM (**Figure 4 et 5**). On trouve notamment quelques framboises par endosome (1 à 5) (**Figure 4A et B**), tandis que les petites nanoparticules de Pt sont hautement agrégées dans un même endosome (**Figure 5A et B**). Cette internalisation efficace a été ensuite confirmée par un dosage du Pt intracellulaire par ICP (**Figure 6**). Les deux types de nanoparticules s'internalisent de manière remarquablement comparable.

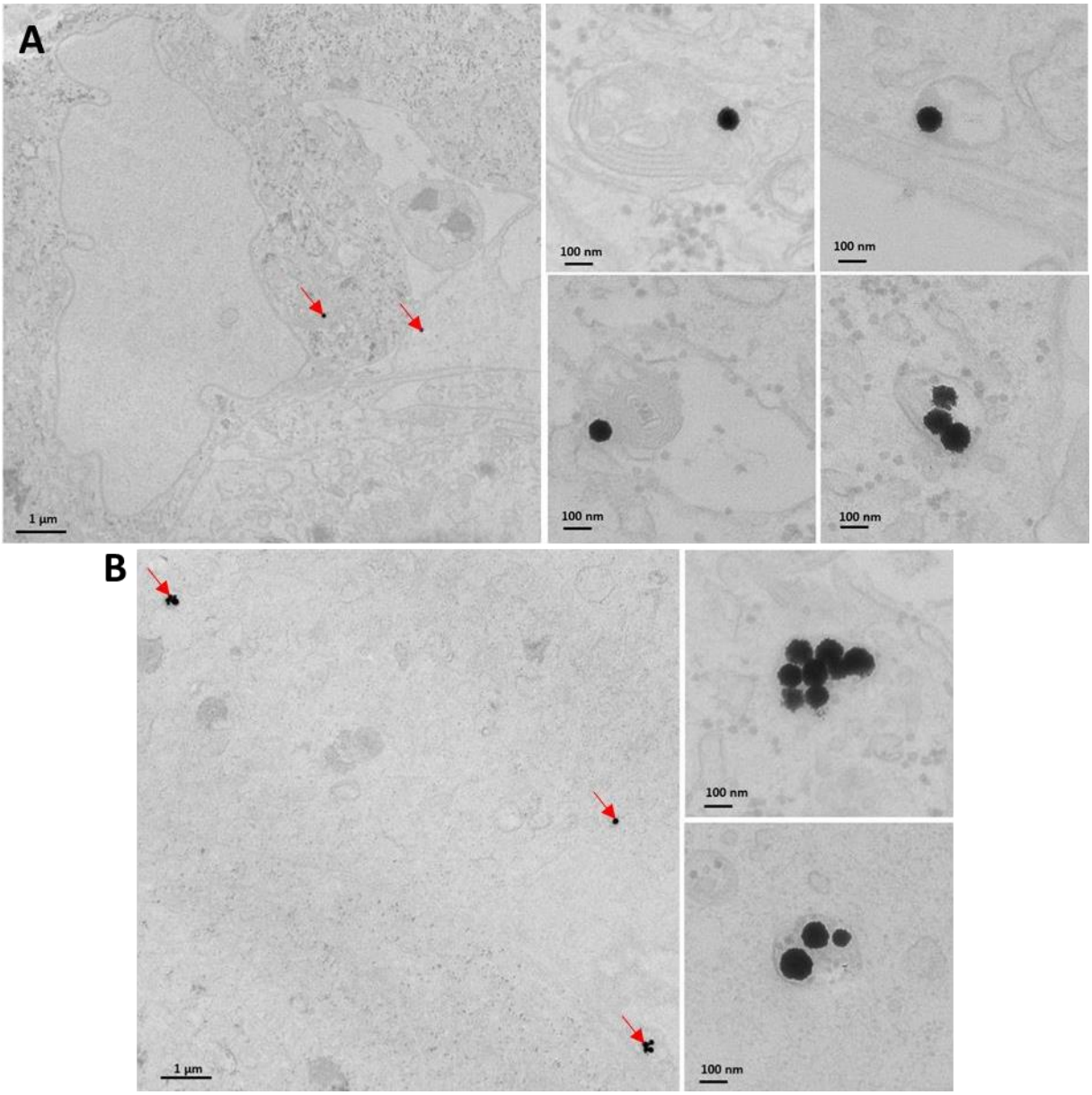

Figure 4 : *Images de TEM des Nano-framboises internalisées dans les endosomes des cellules d'un sphéroïde de glioblastome, après une incubation à [Pt] = 0,2mM (A) et 0,5mM (B) pendant 24 heures. Les images ont été prises 1 jour après, identifiant une à plusieurs nano-framboises au sein d'un même endosome.*

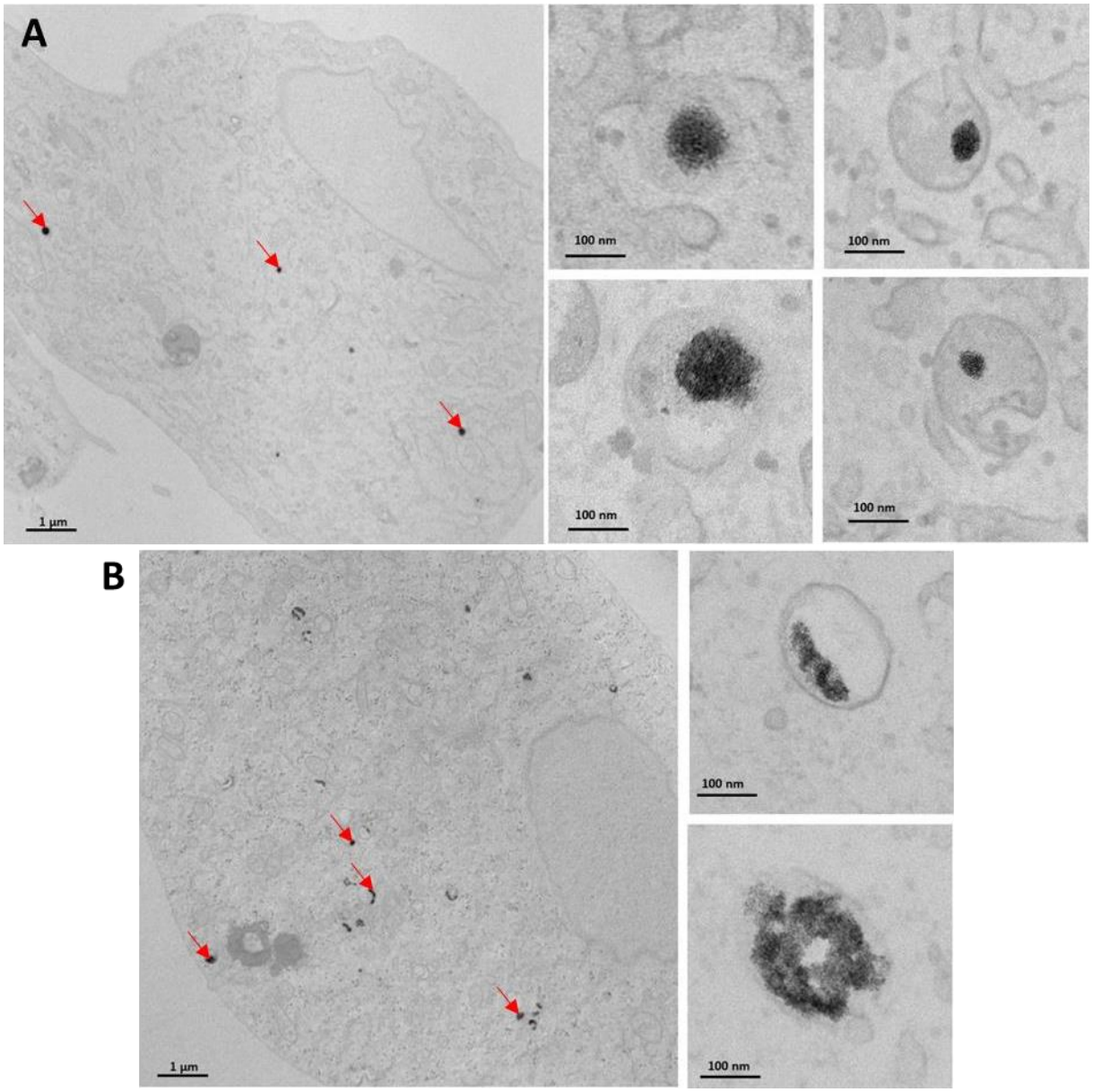

Figure 5 : *Images de TEM des petites nanoparticules de Platine internalisées au sein des cellules d'un sphéroïde de glioblastome, prises un jour après une incubation à [Pt] = 0,2mM (A) et 0,5mM (B) pendant 24 heures, nous permettant de localiser le confinement et l'agrégation des nanoparticules dans les endosomes de la cellule.*

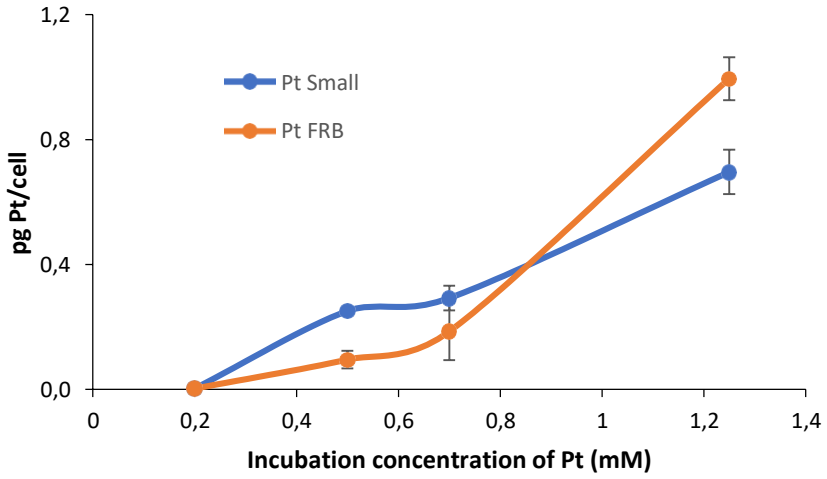

Figure 6 *: Taux d'internalisation des deux types de nanoparticules de platine dans les cellules de glioblastome en fonction de la concentration en platine pendant l'incubation, de [Pt] = 0.2 à 1.25 mM, pendant 24 heures, mesuré par ICP-AES.*

Maintenant assuré de l'internalisation et du confinement des nanoparticules de Pt dans les endosomes, un sphéroïde à la fois a été irradié par un laser à 808 nm et 1 W/cm² pendant 10 min. Les résultats obtenus correspondent à l'élévation de la température à saturation.

Il est ainsi possible d'observer une élévation de température plus importante pour les nano-framboises de platine (**Figure 7**), comme observé précédemment en solution. Mais de façon intéressante, il est possible d'observer un impact du confinement des nanoparticules dans les endosomes avec un échauffement ΔT deux fois plus important qu'en solution pour les FRB et presque dix fois plus grand pour les petites nanoparticules. En effet, l'espace restreint et la proximité entre les nanoparticules au sein des endosomes provoque l'agrégation des objets et augmente considérablement le pouvoir thermique de ces nanoparticules sous irradiation laser, notamment des petites qui va même égaler le chauffage des framboises multicœur. Ceci devrait donc permettre un traitement hyperthermique sous application laser beaucoup plus efficaces au sein des endosomes des cellules cancéreuses grâce à l'accumulation des nanoparticules,.

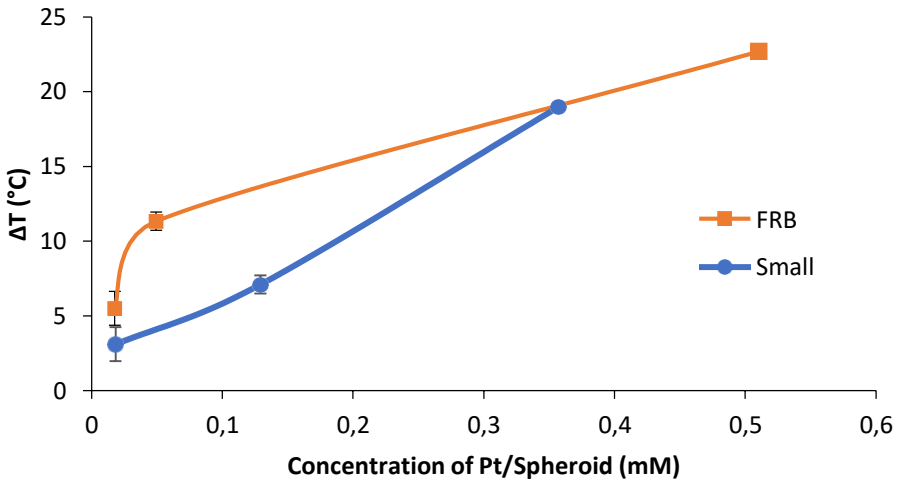

Figure 7 : *Valeurs moyennes de l'augmentation de température en photothermie à 1 W/cm². Après incubation des nanoparticules à différentes concentrations et formation de sphéroïdes, chaque sphéroïde est placé individuellement sous le laser 808 nm à 1 W/cm² et l'élévation de température atteinte au plateau est mesuré par caméra infra-rouge. Le sphéroïde est ensuite dissout dans l'acide et sa concentration est mesurée en ICP-AES afin d'obtenir la concentration en platine responsable de la génération de photothermie*.

c. Impact de l'application du laser sur l'intégrité de la nanoparticule de Pt.

Nous avons ensuite cherché à savoir si cette augmentation de température pouvait déstabiliser la structure stable du platine et provoquer une dégradation en milieu cellulaire acide pour libérer des ions, comme on l'a vu précédemment pour les nanoparticules d'oxyde de fer. Ainsi, les nanoparticules de Pt pourraient générer une double action thérapeutique, chimique (ions Pt) et thermique. Pour cela, nous avons exposé les sphéroïdes à une puissance laser de 1 W/cm² pendant 31min et observé leur structure par XANES, deux semaines après l'exposition.

En environnement cellulaire, les deux nanoparticules ressemblent au métal Platine, et cet effet est d'autant plus prononcé pour les framboises. Les résultats d'EXAFS montrent de nouvelles coordinations avec des éléments tels que O, N, C ou S aux jours 1 et 12 correspondants aux interactions avec le milieu biologique. Cependant aucun changement n'est observé entre les jours 1 et 12 sans irradiation (**Figure 8 A,B**), attestant de la parfaite stabilitée de ces nanoparticules en milieu cellulaire. Pour les petites nanoparticules, on retrouve un remodelage de la nanoparticule après l'irradiation (**Figure 8 C,D**). Ce remodelage disparait au fil du temps, jusqu'à ne plus voir l'effet du laser sur la nanoparticule 12 jours après l'irradiation (**Figure 8 E,F**). Concernant les nano-framboises, on observe une biotransformation vers le métal platine après 12 jours, avec une réduction de la valence du Pt (**Figure 9 A,B**). Le laser semble aussi moduler la nano-framboise en améliorant sa cristallinité (et non sa dégradabilité), observation conservée pendant les 12 jours de suivi (**Figure 9 C-F**).

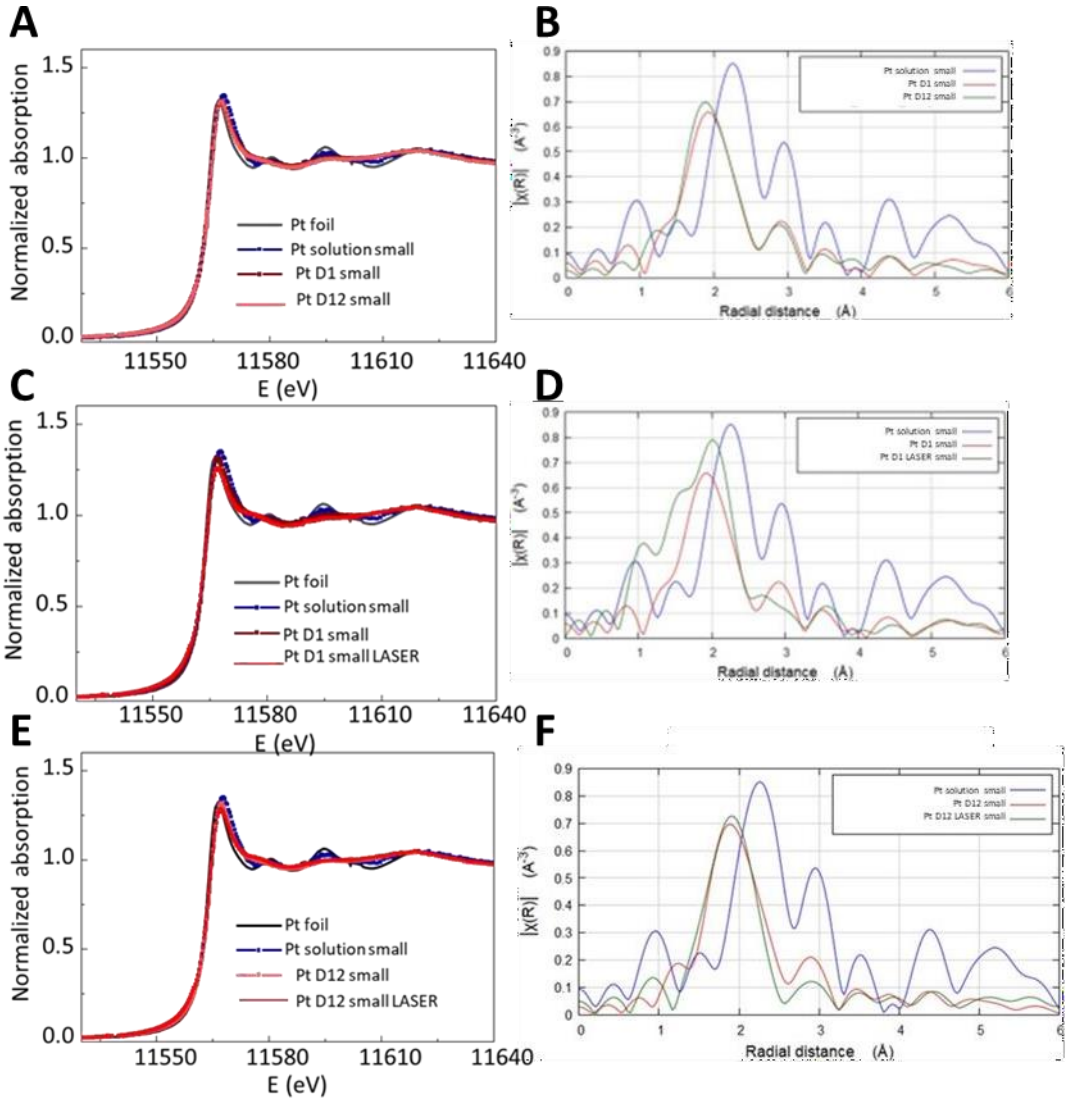

Figure 8 : *Spectre d'absorption XANES et EXAFS mesurés pour la couche L3 du Pt pour étudier l'évolution des petites nanoparticules monocoeur une fois internalisées dans les cellules d'un spheroide tumoral, après 1 ou 12 jours, et avec ou sans application du laser au jour 1 (A-B). Absorption XANES des sphéroides contenant ses petites nanoparticules, avec ou sans traitement laser au jour 1 (C-D) ou 12 jours après (E-F). Ces spectres permettent d'identifier un remodelage de la nanoparticule juste après l'expostion au laser, et qui peut disparaître au cours du temps.*

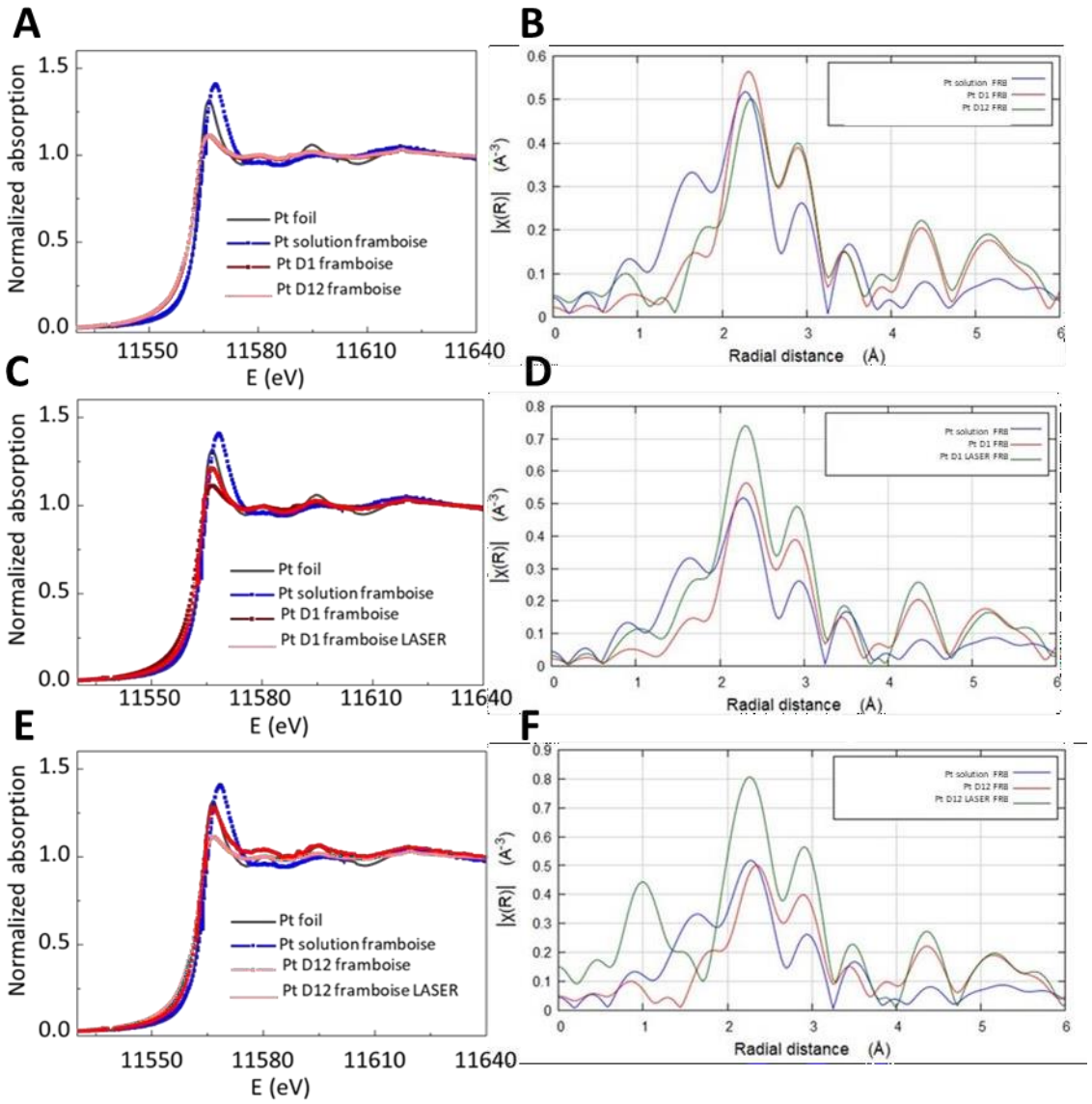

Figure 9 : *Spectres d'absorption XANES et EXAFS mesurés pour la couche L3 du platine afin d'étudier l'évolution des nanoparticules de framboisess multicoeur une fois internalisées dans les cellules d'un spheroide tumoral, après 1 ou 12 jours, avec ou sans application du laser au jour 1 (A-B). Absorption XANES des sphéroides contenant ses petites nanoparticules, après avoir subi une irradiation laser ou non, au jour 1 (C-D) ou 12 jours après (E-F). On observe une augmentation de la crystallinité liée à l'expostion au laser, ainsi qu'un remodelage qui persiste.*

Conclusion

Lors de cette étude, nous avons pu mettre en évidence les propriétés photothermiques des nanoparticules de Pt. Nous avons notamment observé un fort potentiel de chauffage de la structure multicœur en milieu aqueux, et qui, une fois confinée dans les cellules, conserve ses propriétés de chauffage sous irradiation laser. De plus, elles conservent une bonne stabilité

dans l'environnement intracellulaire, sans dégradation observable, leur offrant une bonne cytocompatibilité. Même après application du laser, les structures en framboise ne semblent pas se dégrader, n'offrant donc pas la possibilité d'exploiter la possible toxicité des ions Pt pour le moment. A l'inverse, l'exposition au laser rend les structures davantage cristallines. Un remodelage est donc possible et reste encoreà explorer.

Concernant les petites nanoparticules de Pt monocœur, celles-ci présentent des capacités de chauffage faibles en solution, mais génèrent davantage de chaleur une fois confinées et agrégées dans les endosomes. Ainsi dans le cas d'un ciblage sur les cellules cancéreuses, cela permettrait une thérapie par l'hyperthermie seulement dans les cellules ayant fortement internalisées et concentrées ces nanoparticules, et de limiter les effets délétères aux tissus voisins sains. Cependant, tout comme les structures multicœurs, les petites nanoparticules de Pt restent très stables dans les cellules, sans se dégrader, même après irradiation au laser.

Matériel et méthodes

a. Synthèse des nanoparticules de Pt

Dans une fiole jaugée de 10 mL, 80 µL de potassium tetrachloroplatinate (II) (K_2PtCl_4) à 20 mM sont dispersé dans 2 mL d'eau distillé puis 180 µL d'une solution d'Alendronate à 20 mM y est ajoutée. Cette solution placée à un pH acide ou basique permet la formation des deux types de nanoparticules. Puis 40 µL d'une solution d'ascorbate de sodium (17.6 mg mL^{-1}) ont été ajouté et la solution est placée dans un appareil micro-onde (Monowave 300, Anton Paar GmbH) pendant 30 minutes à 80°C à l'aide d'un thermomètre en rubis. L'augmentation de température jusqu'à 80°C doit être rapide puis maintenu pendant 30 minutes avec une agitation à 1200 rpm durant les deux étapes. Les solutions comportant les nanoparticules sont ensuite purifiées par un système de dialyse (Spectra.Por Float-A-Lyzer G2).

b. Mesure de la photothermie induite par irradiation laser

Le profil de chauffage en solution aqueuse a été obtenu en plaçant un Eppendorf de 0,5 mL, avec 50 µL d'une suspension de nanoparticules diluée dans de l'eau à pH 7 à des concentrations allant de [Pt] = 0.125 à 6.7 mM, sous le faisceau laser à une distance de 4,5cm de la surface du liquide. Les échantillons sont irradiés avec un laser à 808 nm (Laser components) à la puissance de 1 W/cm^2 pendant 10 minutes. L'élévation de température a été mesurée en temps réel en utilisant une caméra thermique infrarouge (FLIR A615) et en traitant les données avec le logiciel FLIR ResearchIR.

Pour les expériences en cellule, un seul sphéroïde a été placé au fond d'un Eppendorf de 0,5 mL avec 100 µL de milieu de culture. Le sphéroïde est alors irradié à une densité de puissance de 1 W/cm² pendant 10 minutes

c. Culture cellulaire

Les cellules U-87 MG human glioblastoma (ATCC) ont été cultivées dans le milieu de culture Dulbecco's Modified Eagle Medium (DMEM, Gibco) complémenté avec 10% de sérum fœtal bovin et 1% de penicillin-streptomycin (Thermo Fisher Scientific) dans un incubateur humidifié avec 5% de CO_2 à 37°C. Après avoir atteint 80% de confluence, les cellules sont détachées en utilisant une solution à 0,05% trypsin-EDTA (Gibco). 200 000 cellules sont dispersées dans 1 mL de milieu deculture dans un tube Falcon de 15 mL et centrifugées à 1100 rpm pendant 5 minutes pour former un culot de cellule. Ce culot est laissé dans l'incubateur avec le bouchon ouvert pour maturer pendant un jour et forme systématiquement un sphéroïde cohésif.

d. Incubation des cellules

Après avoir atteint 70-80% de confluence, une solution de nanoparticules est dispersée dans du milieu de culture complet à des concentrations de [Pt] = 0,2 à 1,25 mM. Le milieu de culture des cellules est alors aspiré et remplacé par ce milieu contenant les nanoparticules. Les cellules sont laissées à incuber pendant 24 heures. Les cellules sont ensuite rincées 2 fois au PBS afin d'éliminer les nanoparticules non internalisées. Les cellules sont détachées et suivent le processus de formation de sphéroïde.

e. Imagerie par microscopie électronique à transmission

Les sphéroïdes ont été analysés sous microscope électronique à transmission pour observer les nanoparticules dans les cellules à l'échelle nanométrique. Pour ce faire, les sphéroïdes sont lavés avec un tampon cacodylate (0.2M), puis fixés avec 5% de glutaraldéhyde dans 0.1 M de cacodylate tampon pour 30 minutes à température ambiante puis rincés à nouveau dans le même tampon. Les échantillons sont ensuite contrastés à l'aide de Oolong Tea Extract (OTE) dilué à 0.5% dans le tampon cacodylate, et post-fixés dans 1% osmium tetroxide contenant 1.5% de ferrogrenat de potassium puis déshydratés dans des bains d'éthanol croissant. Les échantillons sont ensuite inclus dans une résine Epon epoxy, sectionnés (70 nm) et déposés sur une grille de cuivre pour une observation avec un microscope électronique HITACHI HT 7700 opérant à 120kV (INRA, France).

f. Quantification du Platine

La quantité totale de platine dans les échantillons a été déterminée par un ICP-AES (inductively coupled plasma atomic emission spectroscopy - Spectrogreen, SPECTRO, Germany) pour

quantifier l'internalisation des nanoparticules en cellules. Pour chaque mesure, le nombre de cellule a été compté à l'aide d'une chambre de Malassez, et les échantillons ont été digérés par de l'eau régale constitué d'un mélange d'acide chlorhydrique concentré (2/3) et d'acide nitrique à 69% (1/3). La mixture est alors placée sur une plaque chauffante pour évaporation, puis re-suspendue dans 200 µL de HCl concentré (Sigma, trace metal basic grade) pendant deux jours. La solution est alors diluée avec de l'eau filtrée ultra pure pour obtenir une solution finale à 2% HCl.

g. Spectroscopie d'absorption des rayons X (XAS)

Les mesures au XAS ont été réalisé à CLÆSS beamline (BL22) au synchrotron Espagnol ALBA-CELLS (Barcelona, Spain). Tous les spectres ont été acquis à température ambiante et à pression atmosphérique en mode de transmission et de fluorescence à Pt L3-edge. Chaque spectre XAS est une accumulation de 5 à 10 acquisitions moyennées afin d'améliorer le ratio signal-bruit. La calibration de l'énergie a été réalisée par une feuille de métal de platine pure standard. La normalisation des données, l'énergie de calibration et les analyses de XAS ont été réalisées en utilisant le pack de logiciel Demeter (Athena). Le Signal XAS a été obtenu en normalisant l'amplitude de l'oscillation aux abords du saut, en soustrayant le bruit de fond avec un ajustement polynomial.

CHAPITRE 3
Biosynthèse d'oxyde de fer dans les cellules souches

Dans le premier chapitre, nous avons cherché à comprendre l'influence de différents éléments impliqués dans la dégradation intracellulaire des nanoparticules magnétiques d'oxyde de fer, pour pouvoir mettre en place un contrôle sur leur devenir après leurs actions thérapeutiques.

Dans ce chapitre, nous avons abordé une toute autre approche. En effet, le fer est l'un des métaux les plus répandu dans le métabolisme humain. Il est impliqué dans de multiples interactions, fondamentales au bon fonctionnement de l'organisme. De plus, c'est un métal de transition, avec une régulation très fine de ses processus d'oxydation et de réduction afin d'éviter, entre autres, tout risque de toxicité. On vient de voir dans le premier chapitre que l'internalisation de nanoparticule d'oxyde de fer constitue un apport important et quasi-instantané de fer, que la cellule doit prendre en charge via les différentes voies d'assimilation du fer.

Tandis que le métabolisme du fer dans l'organisme est très largement documenté, la présence spontanée d'une forme magnétique reste singulière. En effet, malgré l'observation dans les années 90 de la présence d'oxyde de fer magnétique dans le corps, notamment au niveau du cerveau et du cœur (Chez les patients atteint de la maladie d'Alzheimer notamment)[155,156], sa présence est encore inexpliquée etpeu explorée.

Ces observations montrent que les cellules humaines sont capables de contenir du biomagnétisme. Récemment, cette capacité de biosynthèse magnétique a été démontrée dans des cellules souches mésenchymateuses humaines qui ont été capables de re-cristalliser de nouvelles nanoparticules d'oxyde de fer magnétiques, après avoir internaliséet dégradé des nanoparticules d'oxyde de fer magnétiques synthétiques. Nos cellules souches sont donc capables de synthétiser un matériel magnétique biogénique.

Un être vivant est constitué de cellules souches différenciées qui ont, le plus souvent, perdues leur capacité à se diviser mais possèdent à la place des fonctions spécifiques. Les cellules souches sont des cellules indifférenciées, non fonctionnelles, qui se renouvellent dans le but de se maintenir dans l'organisme et qui vont se différencier en cellules spécialisées en cas de besoin. Les cellules souches mésenchymateuses humaines (hMSC) sont des cellules multipotentes, c'est-à-dire capables de se différencier en un nombre restreint de types cellulaires, principalement en adipocytes (cellules adipeuses), en chondrocytes (cellules du cartilage) ou en ostéocytes (cellules osseuses). Elles sont principalement retrouvées dans la moelle osseuse. Les cellules souches représentent l'élément central de la médecine

régénérative, car elles peuvent être utilisées pour créer des tissus fonctionnels dans le but de remplacer ou de réparer des tissus endommagés. Elles permettraient d'éviter le rejet d'organe, par exemple grâce à une greffe autologue, constituée à partir des cellules souches du patient. Les cellules souches peuvent être prélevées, cultivées in vitro, subir une différenciation avant d'être implantées de nouveau.

Dans ce but, l'utilisation de cellules souches magnétisées permettrait d'envisager la formation de nouveaux tissus en facilitant l'interactions entre cellules à l'aide d'un champ magnétique. C'est le principe de l'ingénierie tissulaire magnétique[95,157]. Elles pourraient aussi être guidées magnétiquement directement vers une lésion afin de reformer le tissu endommagé et permettant même un suivi via IRM. Cependant, après réparation tissulaire, la question du devenir des nanoparticules préalablement introduites dans ces cellules souches reste un problème potentiel à une application clinique.

Imaginons alors des cellules souches bio-magnétisées, sans jamais avoir été en contact avec des nanoparticules magnétiques synthétisées par voie chimique. Cela pourrait apporter un nouveau souffle de « biocompatibilité » au domaine de l'ingénierie tissulaire magnétique.

La capacité cellulaire à bio-synthétiser des nanoparticules magnétiques fait écho aux nanoparticules biologiques produites par les bactéries magnétotactiques : les magnétosomes. Ces bactéries sont des procaryotes à gram négatif, qui biosynthétisent des nanocristaux magnétiques d'oxyde ou de sulfure de fer. Ces magnétosomes sont entourés d'une membrane et alignés en chaine dans le cytoplasme, ce qui permet à la bactérie de s'orienter le long des lignes du champ magnétique terrestre. Ces bactéries ont été très largement étudiés pour cette spécificité, et un cluster d'un grand nombre de gènes[158] comme mms6, spécifiques à cette bactérie, ont été identifiés comme impliqués dans ce mécanisme.

Les hMSC semblent donc avoir également la capacité à produire des nanoparticules d'oxyde de fer magnétiques. Nous avons donc décidé d'explorer cet aspect en appliquant le même protocole d'incubation de précurseur d'ions fer appliqué à la bactérie magnétotactique, aux cellules souches humaines (hMSC) et de souris (mMSC), dans le but de déterminer si des nanoparticules magnétiques d'oxyde de fer totalement issues d'une synthèse biologique pourraient être obtenues à partir de précurseur d'ions fer non magnétiques uniquement.

Typiquement, le protocole de base appliqué a été le suivant : une incubation en continue des cellules souches avec 34 µM de Quinate de Fer ($(C_7H_{11}O_6)_3Fe$ – Précurseur de Fe (III)) complété avec du citrate dans le milieu de culture. Ces premiers tests ont été réalisés sur cellules souches de souris pour des raisons de croissance plus rapide et de culture facilitée, permettant d'explorer davantage de conditions. Ces tests ont mis en évidence une internalisation du fer en continu sans atteindre une saturation pour cette concentration, ainsi que la formation de

cristaux magnétiques en quantité faible via l'apparition d'un moment magnétique mesuré par magnétométrie, après presque un mois d'incubation (28 jours). Ces résultats sont une preuve de concept de la capacité de ces cellules à biosynthétiser des nanoparticules magnétiques à partir d'un précurseur d'ion Fe^{3+} (Quinate de Fer).

Nous avons ensuite caractérisé ces produits de biosynthèse, tout d'abord par microscopie électronique (TEM). Le Fe^{3+} est capté par la cellule, puis stocké dans la ferritine, et forme un cristal d'une taille moyenne d'environ 6 nm, qui correspond au diamètre interne de la ferritine (6 à 8 nm). Nous avons ensuite pu mesurer le niveau d'expression des gènes impliqués dans le métabolisme du fer pendant la biosynthèse, avec une surexpression obtenue, par exemple pour la ferritine, néanmoins faible.

Cette capacité de biosynthèse a également été observée dans les mêmes conditions à partir de cellules souches humaines (hMSC) non différenciées ou en adipogénèse. Un signal faible après un temps d'incubation long est obtenu, du même ordre que pour les cellules souches de souris.

La suite de l'étude a eu vocation à mettre en place d'autres protocoles pour améliorer cette biosynthèse. L'idée initiale était d'augmenter la quantité de fer internalisée afin de remplir davantage les ferritines. Les différentes pistes explorées sont résumées ci-dessous :

- Ajout de citrate libre dans le milieu d'incubation car le citrate intervient dans le métabolisme du fer chez le mammifère pour éviter la production d'espèces réactives, ou la précipitation du Fe^{3+} en formant un complexe. Il a aussi montré son importance chez des patients avec un excès en fer, en ayant ce rôle de ligand. Son rôle de chélateur restait donc à être exploré dans la biosynthèse magnétique cellulaire.
- Incubation en continu à des concentrations différentes en quinate de fer, avec ou sans chélateur de fer dans le milieu. La concentration en sels de fer incubée a été augmentée jusqu'à atteindre une concentration toxique pour les cellules. Malgré une internalisation croissante, le signal magnétique n'est que très peu augmenté. Cependant, certains puits pouvaient présenter un signal magnétique important tandis que les répliquas restaient faiblement magnétiques. Cette variabilité a été régulièrement retrouvée, pour des conditions jamais identiques, sans que l'on n'ait su identifier sa cause.
- Reprenant le modèle d'incubation des nanoparticules qui s'apparente à un apport important et soudain de fer aux cellules, nous avons ainsi mis en place deux protocoles d'incubation de sels de fer de type « pulse » : 7 h ou 24 h avec 1 à 4 mM de fer. Dans le cas des 7 heures d'incubation, le milieu était renouvelé toutes les heures.
- Cette condition a été testée avec deux autres sels de fer : L'ascorbate de fer $(C_6H_7O_6)_2Fe$ et le Sel de Mohr $Fe(SO_4)_2(NH_4)_2 \cdot 6H_2O$. Le protocole de pulse pendant 7 h

avec milieu renouvelé a permis d'augmenter de manière conséquente la quantité de fer internalisée mais pas le signal biomagnétique.

- Transfection de gènes impliqués dans le métabolisme du fer pour une surexpression dans les mMSC, dans le but d'identifier leur possible rôle dans la biosynthèse et de l'augmenter. Les transfections ont été réalisées par Carine VIAS, avec qui j'ai eu la chance de participer à leur élaboration. Malgré des lignées surexprimant les gènes DMT1, mms6, la ferritine et la sous unité H de la ferritine, aucune n'a montré d'augmentation significative de la production de nanoparticules bio-magnétiques. La piste des transfections n'a cependant pas été abandonnée car elle avait prouvé son efficacité, notamment pour le gène mms6, et les études sont encore en cours.[159]
- Utilisation d'autres types cellulaires tels que des cellules endothéliales (HUVEC), ou cancéreuse (glioblastome), aucun n'ayant mis en évidence une biosynthèse.

Nous avons finalement ensuite eu l'opportunité d'avoir accès aux Synchrotrons de Grenoble (ESRF) puis de Barcelone (ALBA) grâce à la participation d'Ana ESPINOSA, afin d'étudier les propriétés structurales et la valence d'échantillons avec une incubation continu ou en mode de pulse. Le XANES apporte une information sur la coordination et l'état d'oxydation tandis que le EXAFS apporte une information sur l'environnement local, et les distances interatomique. Pour l'incubation en continu, nous avons pu observer l'apparition d'oxyde de fer pour certaines conditions ainsi qu'une valence en Fe^{3+} quel que soit la valence du précurseur au départ après 36 jours. Concernant l'incubation pulse de 7 heures, les valences sont elles aussi toutes présentes sous forme Fe^{3+} après 1 semaine, et les 3 sels présentent un mélange de ferrihydrite et d'oxyde de Fer.

Cette étude de biosynthèse magnétique par des cellules souches constitue les premiers pas d'une mise en lumière de cette capacité à biosynthétiser des nanoparticules magnétiques d'oxyde de fer à partir de précurseurs de fer non magnétiques. L'ensemble de l'étude est détaillé dans les pages suivantes sous la forme d'un article.

Abstract

Iron is one of the most common metal on earth and in the human body, with a largely described metabolism including numerous proteins involved in its transport, storage but also oxidation as well as reduction. A less explored and less understood singularity is the presence of magnetic iron in the human body. It has been shown, for quite some time now as the first proofs are from the 1990's, that iron oxides (magnetic) are present in various organs, such as the brain and heart. Recently, and for the first time, we demonstrated that human cells are capable of the synthesis of such iron oxides. These experiments were performed in a very specific case as chemically synthesized were first internalized in human stem cells, they were degraded by the cells in the first days of culture (days 1 to 3) and a recrystallization was then observed corresponding to the synthesis of new magnetic nanoparticles produced by the human cells themselves. This first proof of magnetic nanoparticles biosynthesis made by human cells answered to the question of the capacity of these cells to perform such synthesis. Herein, the goal was to go further and observe if this biosynthesis can be carried out from an ionic precursor instead of chemically synthesized magnetic nanoparticles. Mouse and also human stem cells were incubated with ionic iron for up to 36 days, and the biosynthesis of magnetic nanoparticles was here again observed. This synthesis for instance happens upon 14 to 21 days of continuous incubation with 34 µM ferric quinate, when the cells are loaded with iron, confirming that the biosynthesis takes place in case of important input of iron.

Introduction

Iron is one of the most preeminent metals on earth and is part of the few metals involved in human metabolism together with copper, manganese, cobalt, molybdenum, and zinc[160]. Among them, iron and copper are defined as transition metals; they can undergo oxidation and reduction processes and, remarkably, do so within the entire redox potential of the living systems, being approximately between -400 and +800 mV at pH 7. The implications are quite extraordinary as, with only one metal, it is possible to carry out biochemical reactions within almost 1 V of redox potential by modulating the coordination of iron (e.g. linked to sulfur in Fe-S clusters or cytochromes)[161]. Despite acknowledging the presence of iron in the cells as well as proteins and transporters associated to the regulation of this metal, cell behavior in presence of iron is not yet fully understood.

One of the singularities still poorly understood regarding iron in the human body, consists in its presence under a magnetic form. It has been shown, for quite some time now as the first proofs are from the 1990's, that iron oxides (magnetic) are present in various organs, such as the brain and heart. More recently, and for the first time, we demonstrated that human cells are capable of the synthesis of such iron oxides[12,13] . These experiments were performed in a

very specific case as chemically synthesized were first internalized in human stem cells, they were degraded by the cells in the first days of culture (days 1 to 3) and a recrystallization was then observed corresponding to the synthesis of new magnetic nanoparticles produced by the human cells themselves. This first proof of magnetic nanoparticles biosynthesis made by human cells answered to the question of the capacity of these cells to perform such synthesis.

In addition to bringing additional perception to the cellular handling of iron, this intrinsic biosynthesis of magnetic nanoparticles might be of interest in the nanomedicine context. Indeed, iron oxide nanoparticles have attracted interest for biomedical applications due to their magnetic properties that can be exploited for cell tracking/imaging (e.g. via magnetic resonance imaging (MRI) or magnetic particle imaging (MPI)), cell targeting, magnetic cell sorting (magnet-assisted cell separation (MACS)), tissue engineering, or again anti-cancer therapy (e.g. hyperthermia, photothermia)[162]. For such applications to be made possible, a first step is to magnetize the cells with magnetic nanoparticles. An increasing number of approaches are being developed to do so. The most common one consists in the use of synthetically produced magnetic nanoparticles, which are either incorporated in the cells or attached to their surface [163]. The main advantage of this approach is the possibility to tune the features of the nanoparticles, such as enhancing their potential for specific applications. The heating potential via magnetic hyperthermia /photothermia can for example be enhanced by tuning the shape of the nanoparticles (e.g. nanospheres vs. nanoflowers)[164]. These nanoparticles can be coated with specific polymers or metals allowing the regulation of their degradation speed[14]. Nanohybrids can also be designed, allowing the combination of the magnetic properties of iron oxides with for example heating of copper. A second approach consists in the use of magnetic nanoparticles from biological origin[165]. Indeed, certain organisms possess a natural intrinsic metabolism capable of such synthesis. Among them, there is the well-known case of the magnetotactic bacteria, for which numerous genes encoding for specific proteins have been described as being part of this synthesis mechanism[182]. In this case, using iron ions only. The properties of these biological nanoparticles can even be tuned, in vitro, using one or several recombinant proteins of the magnetotactic bacteria[166]. In vitro again, but this time within mammalian cells, genes of the magnetotactic bacteria have been transfected, such as mms6. By feeding of these cells with iron ions, magnetic cells were obtained[159].

The recent evidence that human stem cells are able to produce magnetic nanoparticles was obtained upon internalization of external magnetic nanoparticles from synthetic or biological origin, which were first degraded before being reshaped by the cells. Herein, the goal was to go further and observe if this biosynthesis can be carried out from an ionic precursor instead of external magnetic nanoparticles. To do so, mouse and human stem cells (mMSC and hMSC) were continuously incubated with ionic iron for up to 36 days, and cellular management of

this iron was assessed. Total iron content analyses showed a progressive internalization of iron over the 36 days, accompanied with the appearance of a magnetic signal corresponding to a biosynthesis of magnetic nanoparticles. This signal remains low in comparison to the amount of iron per cell; it is a secondary but still existent biomineralization that takes place upon a minimum of 14 days of culture, when the cells are loaded with iron.

Material and Methods

Cell culture

Murine mesenchymal stem cell line C3H/10T1/2, Clone 8 (ATCC CCL-226) were cultured in DMEM medium supplemented with 10% FBS and 1% penicillin streptomycin (Thermo Fischer Scientific) at 37 °C with 5% CO_2. Cells were grown until passage 10 to 25 and at 80% confluence prior to seeding.

Human mesenchymal stem cells (Lonza) were cultured in MSCGM medium (Lonza) at 37 °C with 5% CO_2. Cells were grown until passage 5 to 6 and at 80% confluence prior to seeding. These human MSC were subjected to adipogenic differentiation, which was shown as the most efficient differentiation pathway (when compared to osteogenesis and chondrogenesis, or to keeping the MSC in an undifferentiated state) for the neo-production of biomagnetic nanoparticles in the initial re-magnetization experiments[176]. Cells were seeded in six-well plates ($2x10^5$ cells/well) and their adipogenic differentiation was induced as previously described[176] . Briefly, two independent media were used. First, cells were cultured in Adipogenic Induction Medium (AIM) that consisted of high glucose DMEM (Dulbecco's Modified Eagle Medium) (Thermo Fischer Scientific) supplemented with 10% FBS, 1% penicillin and streptomycin (Thermo Fischer Scientific), 10 ng/mL insulin (Sigma), 1 µM dexamethasone (Sigma), 200 µM indomethacin (Sigma), and 500 µM isobutyl methylxanthine (Sigma). After three to four days, medium was changed to Adipogenic Differentiation Medium (ADM) for three days, which was composed of high glucose DMEM supplemented with 10% FBS, 1% penicillin-streptomycin, and 10 ng/mL insulin. The treatment was repeated three times (AIM for three to four days followed by ADM for three days) then cells were maintained in ADM until day 36, with media replenished twice a week.

Incubation with ferric quinate, ferrous ascorbate, or Mohr's salt

Cells were seeded in six-well plates ($2x10^5$ cells/well) and, the following day, were incubated with three types of iron-based solutions that vary in the valence state of their iron ions, being Fe^{3+} for ferric quinate while Fe^{2+} for ferrous ascorbate and Mohr's salt. Iron solutions were prepared maximum 10 minutes prior use. Stock solutions were made from 270 mg iron (III) chloride hexahydrate (#236489, Sigma) with 190 mg D-quinic acid (#138622, Sigma) diluted in

10 mL distilled H_2O for 100 mM ferric quinate stock, from 406 mg iron ascorbate (Sigma) diluted in 10 mL distilled H_2O for 100 mM ferrous ascorbate (Sigma) stock, and from 392 mg ammonium iron(II) sulfate hexahydrate (#215406, Sigma) diluted in 10 mL distilled H_2O for 100 mM Mohr's salt stock. Solutions were filtered with a 0.20 µm filter and added to the medium at concentrations ranging from 17 µM ($1/2C_0$) to 544 µM ($16C_0$), without or with 2 mM of citrate (Sigma). Iron internalization was performed by incubation with these solutions at 37 °C and 5% CO_2 either continuously for the $1/2C_0$, C_0, $2C_0$, $4C_0$, $16C_0$, $32C_0$, and $100C_0$ conditions (C_0 = 34 µM) or as pulse of 7 or 24 hours for the 1, 2, 3, and 4 mM conditions. For the 7-hours pulse, medium containing iron was replenished every hour. For the continuous incubations, iron and citrate were added to the medium when the medium was replenished (twice a week).

Iron quantification and imaging

For each sample, cell number was counted using a Malassez chamber, and samples were digested in 290 µL of 69% nitric acid (Sigma). Upon minimum two days of digestion, samples were diluted in filtered ultrapure water such as obtaining a final solution at 2% nitric acid. Total iron content was measured by inductively coupled plasma – Atomic Emission Spectroscopy (ICP-AES) (Spectrogreen, SPECTRO, Germany), and reported to the number of cells.

Samples magnetometry

Cells were counted using a Malassez chamber and samples were fixed in 4% paraformaldehyde then rinsed in phosphate-buffered saline (PBS). Magnetism values of fixed samples were analyzed at days 7, 14, 21, 28, and 36 using a vibrating sample magnetometer (VSM) (Quantum Design, Versalab or PPMS). Field-dependent magnetization curves were measured at 300 K as a function of the external field. A low range of -150 to +150 mT was first performed to obtain precise measurements. A higher range of 0 to 3000 mT provided magnetization at saturation.

Transmission Electron Microscopy (TEM)

Cells were rinsed with PBS and fixed in 5% glutaraldehyde and 0.1 mol/L sodium cacodylate buffer (Sigma-Aldrich). Post-fixation was achieved with 1% osmium tetroxide solution (Sigma) containing 1.5% potassium cyanoferrate (Sigma). Gradually dehydration was performed in ascending concentrations of ethanol and cells were embedded in Epon resin. Thin sections (70 nm) were examined with a HITACHI HT 7700 operating at 120kV (INRA, France). Size of the nanostructures was analyzed using ImageJ.

Quantitative RT-PCR

Expression levels of four genes involved in iron metabolism were analyzed by RT-qPCR. Total RNA was extracted from mMSC according to the manufacturer's instructions using the NucleoSpin® RNA kit (Machery-Nagel). An incubation with 10U of DNase for 15 min was performed to avoid DNA contamination. Complementary DNA (cDNA) was then obtained by reverse transcription, using SuperScript II Reverse Transcriptase kit (Thermo Fisher Scientific) according to the manufacturer's instructions. Real-time PCR was carried out using QuantStudio3 (Applied Biosystem) and SYBR green PCR Master Mix (Applied Biosystems). Results were analyzed by the software QuantStudio. The expression of 60S acidic ribosomal protein P0 (RPLP0) was used as reference transcript and results were normalized to day 0. The sequences of primers used are presented in Table 1.

Table 1*: List of primer sequences for gene expression analyses by quantitative real-time PCR.*

Genes	Primers sequences (5' → 3')
RPLP0	Fwd: GCTTCGTGTTCACCAAGGAGGA
	Rev: GTCCTAGACCAGTGTTCTGAGC
FTH1	Fwd: GCCGAGAAACTGATGAAGCTGC
	Rev: GCACACTCCATTGCATTCAGCC
FTL1	Fwd: CCTCGAGTTTCAGAACGATCGC
	Rev: CCTGATTCAGGTTCTTCTCCATG
TRF	Fwd: GTCACTGCCATTCGGAATCAGC
	Rev: CAGTGGTCTCTGCTGACTCACA
SLC40A1	Fwd: CCATAGTCTCTGTCAGCCTGCT
	Rev: CTTGCAGCAACTGTGTCACCGT

RPLP0: Ribosomal protein large subunit P0; FTH1: Ferritin Heavy Chain 1; FTL1: Ferritin Light Chain 1; TRF: Transferrin; SLC40A1: Ferroportin.

Viability assay/Alamar Blue metabolic assay

We chose to combine the number of cells with the metabolic activity as an image of the viability; therefore we used Alamar Blue assay as Metabolic Assay. The assay was performed 24h or 1 week after the first incubation. Alamar blue reagent was added (10%) to DMEM for 2h. At the end, 100uL of each medium is transferred in a 96-well plate and read by fluorescence using an Enspire Multimode Plate Reader (Perkin Elmer, Villebon-sur-Yvette, France) at 570 nm excitation wavelength and 585 nm emission wavelength.

X-ray absorption spectroscopy (XAS)/Synchrotron measurements

XAS measurements were performed on dry solutions of iron salt or on a pull of enough cells to have a good signal-to-noise ratio. Measurements were achieved in the X-ray absorption near edge structure (XANES) and extended X-ray absorption fine structure (*EXAFS*) regimes at the BM23 beamline of the European Synchrotron Radiation Facilities (ESRF, Grenoble, France)

and at the CLÆSS beamline (BL22) of the Spanish synchrotron ALBA-CELLS (Barcelona, Spain). All spectra were acquired at room temperature and atmospheric pressure in transmission and fluorescence modes at the Fe K-edge (7112 eV). Each XAS spectrum of cells was an average accumulation of 5-10 acquisitions merged to improve the signal-to-noise ratio. The energy calibration was performed by a metal Fe foil standard. Data normalization, energy calibration, and XAS analysis were performed using the Demeter software package (Athena program)[167]. XAS signal was obtained by normalizing the magnitude of the oscillations to the edge jump, removing the background with a cubic spline-fitting polynomial. Iron oxides (as maghemite and ferrihydrite) were chosen as iron oxide-based reference standards.

Statistical Analysis

Values are presented as mean ± standard deviation (SD). Significance between two groups was determined using independent Student's T-test. P Values were considered significant with a minimum of 95% confidence level: *$p < 0.05$, **$p < 0.01$ and ***$p < 0.001$.

Results

Management of iron by mouse MSC upon continuous exposure to Fe^{3+} ions

mMSC were incubated with a low concentration (34 µM) of ferric quinate over 36 days to assess iron management by the cells over time. Cell samples were harvested along their incubation with iron (days 0, 3, 7, 14, 21, 28, and 36), counted, and analyzed either by ICP-AES to determine total iron per cell, or VSM to determine the magnetic moment. Results showed an increased cell count over time, an indicator of their viability (**Figure S1**). Total iron analyses indicated a linear internalization of iron over these 36 days, without reaching saturation (**Figure 1A**). VSM analyses performed on cell bulks (200 000 cells or more) allowed the recording of the appearance of a low magnetic moment, as shown in **Figure 1C**. These data indicated that increase in iron amount per cell was accompanied with the production of a low magnetic signal, which was detectable after 14 days of incubation (**Figure 1B**).

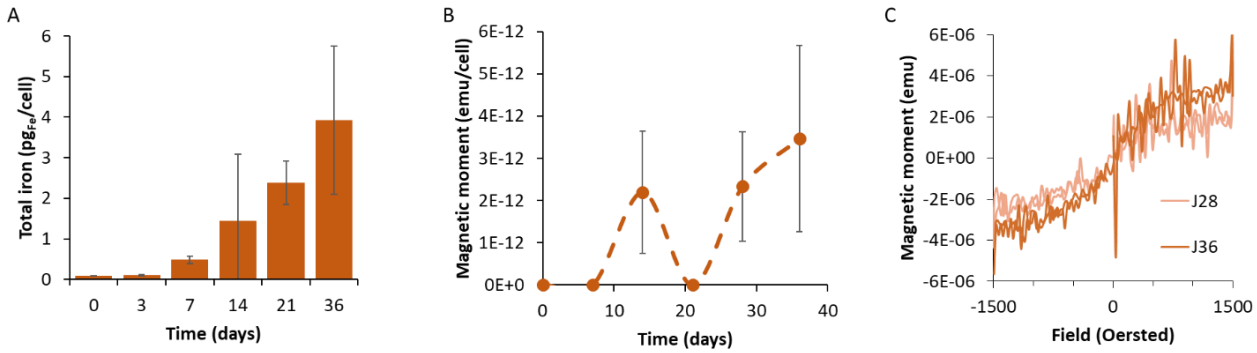

Figure 1*: Iron management by mouse MSC (mMSC) along continuous exposure to 34 µM ferric quinate and 2 mM citrate. A) ICP-AES analyses of total iron on cell bulks (200 000 cells or more), reported to total cell number, indicate a linear internalization of ferric iron over the 36 days of culture, without reaching saturation (n≥3). B) Magnetic properties were measured, on 200 000 cells or more, and the magnetic moment obtained was reported to total cell number. A detectable magnetic moment was obtained upon 14 days of culture (days 0-21, n≤2; days 28&36, n≥3). C) Typical magnetization curves obtained for the cell bulks at days 28 and 36.*

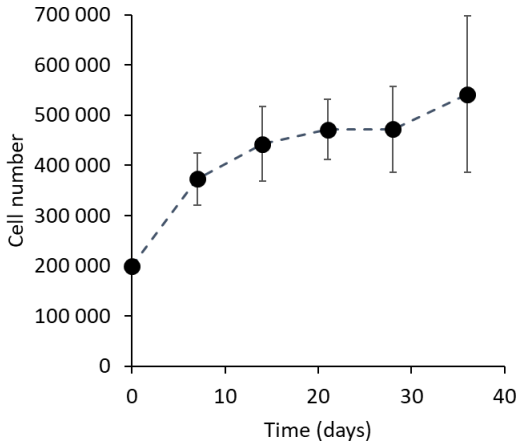

Figure S1*: Number of mMSC continuously exposed to 34 µM ferric quinate and 2 mM citrate progressively increase over time, an indicator of the cellular viability (n≥3).*

TEM images on 70 nm-thick sections of cells along their continuous culture with 34 µM ferric quinate showed the presence of iron mostly within intracellular endosomes (**Figure 2A**). This is consistent with the transport of iron under its Fe^{3+} form as transferrin is a biological chelator capable of binding two Fe^{3+} atoms and interacting with the cell surface transferrin receptor 1 (TfR1), iron is then imported by endocytosis [168]. Size of formed nanostructures were extracted from these TEM images and showed an average particle diameter around 6 nm, with no statistical differences over time (**Figure 2B**). This size fits the internal diameter of the ferritin protein, responsible for iron storage within the cell and known to have a 6-8 nm core[169]. This

protein is made of two types of subunits, light (L) and heavy (H), with varying ratios depending on cell type. The H-subunit has a ferroxidase activity, meaning is responsible for the conversion of iron from its ferrous (Fe^{2+}) to its ferric (Fe^{3+}) form, while the L-subunit may be responsible for electron transfer across the protein cage. Analyses of the genes coding for these subunits showed a progressive increase of both L and H subunits gene expression over time, with the H-subunit reaching up to 20x higher expression at day 36 while 10x more for the L subunit (**Figure 2C**). Genes coding for proteins that regulate intracellular iron import (transferrin) and export (ferroportin) were also upregulated; however, this upregulation remained low as it was only 6 times higher for transferrin receptor and 4 times higher for ferroportin at day 36. Interestingly, there was no balance shift indicating only an export of iron, which could have been expected following a continuous incubation with iron. Instead, iron import seems to keep on taking place at day 36, this is consistent with iron internalization data (**Figure 1**), which doesn't appear to saturate at day 36 when reaching 4 pg of iron per cell.

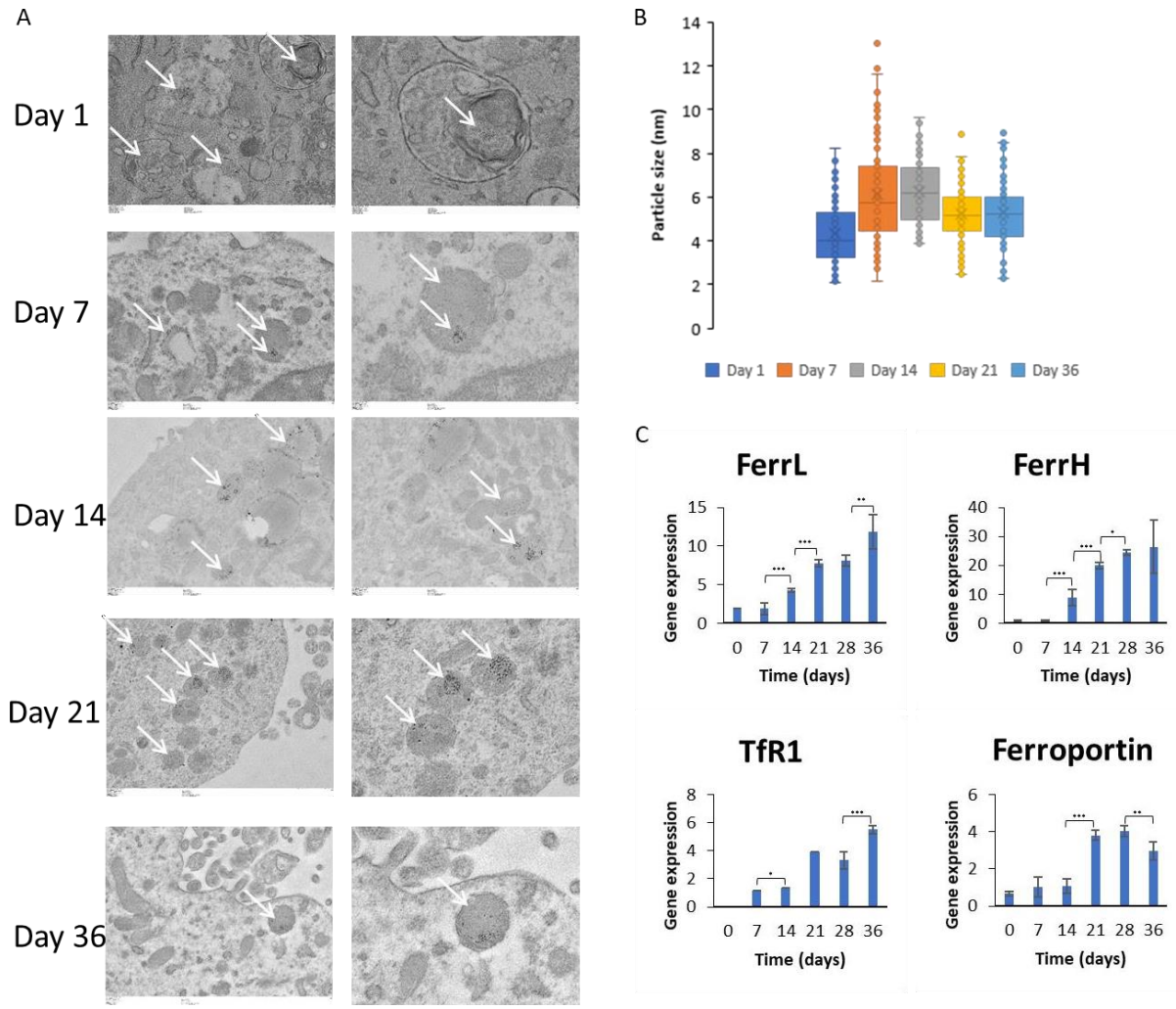

Figure 2: *Features of the bioproduced nanostructures. A) Transmission electron microscopy (TEM) images taken 1, 7, 14, 21, and 36 days upon incubation with 34 µM ferric quinate and 2 mM citrate evidence the presence of dark dots, mostly within the endosomal compartments of the cells. B) Size analyses of the dark dots observed in TEM indicate an average diameter of 6 nm. C) Expression of genes coding for proteins involved in iron metabolism (storage: L-subunit of Ferritin (FerrL), H-subunit of Ferritin (FerrH); import: Divalent Metal Transporter 1 (DMT1), Transferrin receptor protein 1 (TfR1)), and reported to RPLP0, increase over time.*

As a comparison standpoint, similar iron incubation was performed on human MSC (hMSC), in particular over their differentiation along the adipogenic pathway. Indeed, in hMSC, adipogenesis was shown as the most efficient differentiation pathway for the neo-production of biomagnetic nanoparticles in the initial re-magnetization experiments[176]. Here again, a low magnetic moment was detectable after 14 days of culture under constant ferric iron supplementation with citrate (**Figure 3A**). Values are in this case represented for the global cell population, of 200 000 cells (day prior to iron incubation) or more. Size of produced nanostructures, analyzed from TEM images (**Figure 3B**), showed an average diameter around 6 nm, without significant difference over time (**Figure 3C**). This size is here also consistent with the storage of iron within the core of the ferritin protein, being 6-8 nm in diameter[186].

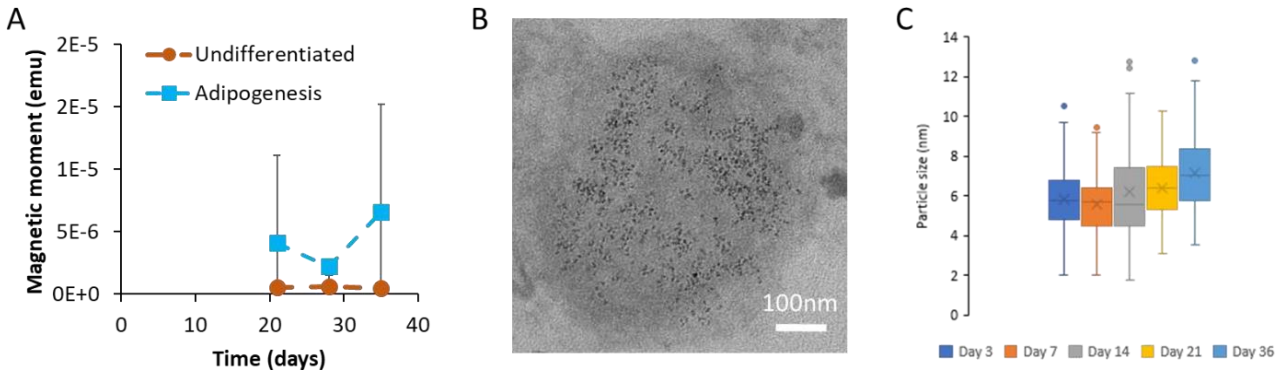

Figure 3: *Initial data (n=1 or 2 for undifferentiated hMSC and n≥3 for hMSC differentiated under the adipogenic pathway) showing the appearance of a low magnetic signal and nanostructures in human MSC, differentiated or not as adipocytes, and continuously incubated with 34 µM ferric quinate and 2 mM citrate. A) Magnetic moment measured on the whole cell content of individual wells of 6-well plates. The initial seeding density was 200 000 cells. B) Representative TEM image showing dark dots within a cellular endosome for the adipogenic condition. C) Size analysis indicated these nanostructures are 6-8 nm in diameter.*

Effect of extracellular ferric citrate concentration on iron internalization and biomagnetic synthesis

In the first part of this study, iron incubations were achieved with 34 µM ferric quinate, as it is a standard source of iron for magnetobacterial culture and magnetosome formation, also tested for the production of intrinsically magnetic MSC upon transfection with two *Magnetospirillum magneticum* AMB-1 genes (mms6 and mmsF)[170]. Additional incubation doses, ranging from 17 µM ($0.5C_o$, C_o initial concentration) to 544 µM ($16C_0$), were tested on mMSC. Following 36 days of continuous iron supplementation with these different iron doses, without or with 2 mM citrate, total iron internalized by the cells, cellular biomagnetism, and cell number were measured (**Figure 4**). Results indicate that an increase in extracellular iron concentration tends to increase the amount of internalized iron, both with and without citrate (**Figure 4A,B**). Interestingly, this increased intracellular iron content does not necessarily correlate with an increased biosynthesis of magnetic nanoparticles (**Figure 4C,D**). Within the range of iron incubations assessed, increased iron dose does not impact cell proliferation, which is however lower in the presence of citrate (**Figure 4E** compared to **4F**). Higher incubations doses of $32C_o$ and $100C_o$ were also tested and, at $100C_o$, cell death was observed (data not shown).

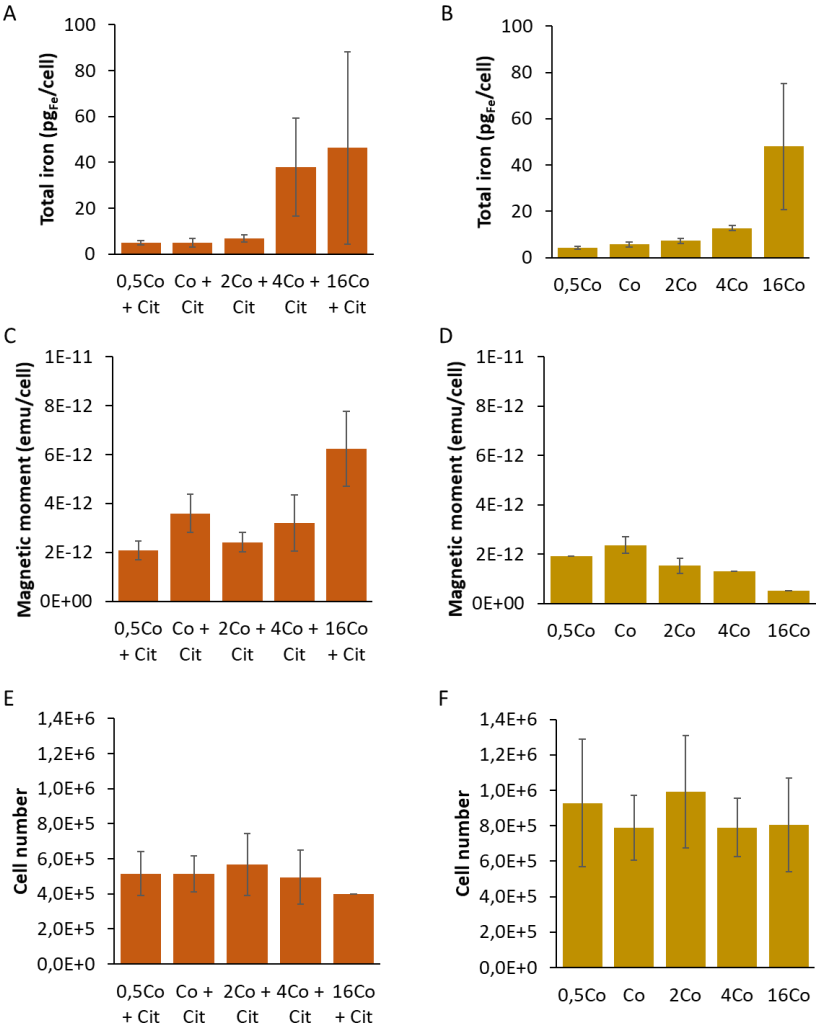

Figure 4: *Management of iron by mMSC upon 36 days of continuous incubation with varying concentrations of ferric quinate (1/2C_0, C_0, 2C_0, 4 C_0, or 16 C_0, C_o initial concentration), with (A,C,E) or without (B, D, F) 2 mM citrate. A-B) Total iron content per cell upon 36 days of incubations (n≥4). C-D) Magnetic moment per cell (n≤2). E-F) Cell number (n≥4).*

Finally, two additional iron salts were tested to assess the influence of initial iron state (Fe^{2+} vs. Fe^{3+}) and surrounding molecules on iron management by the cells. With the goal of controlling this iron valence as most as possible, iron incubations were here applied as short pulses (7h or 24h) instead of continuously on the long term. Indeed, iron might become oxidized in the medium, a phenomenon that would be more pronounced over longer incubations. Pulses of 1, 2, 3, or 4 mM of either ferrous ascorbate (Fe^{2+}), Mohr's salt (Fe^{2+}), or ferric quinate (Fe^{3+}) all with 2 mM citrate were thus applied for 24h. Always with the objective of limiting oxidation before internalization, a 7h hour pulse, during which medium was replenished with freshly prepared iron-supplemented medium every hour, was also achieved for the 4 mM condition with 2 mM citrate. Effects of these incubations on cell metabolic

activity and iron internalization were assessed (**Figure 5**). Cells metabolic activity was measured for the 24h pulses, one week after the incubation (**Figure 5A**). Results demonstrate that this activity clearly decreases with extracellular iron concentration increasing from 1 to 4 mM and, interestingly, that at a given iron concentration, the metabolic activity varies depending on the iron salt used. Ferrous ascorbate engenders most cytotoxicity, while Mohr's salt the least. Also, total iron content per cell was assessed and indicated the highest content for ferrous ascorbate and the least for Mohr's salt (**Figure 5B**). It suggests that the toxicity comes from different internalization kinetics between the salts and not from the salt composition itself. Shorter (7h) pulses with 4 mM of the iron salt-supplemented media replenished every hour indicated similar data (**Figure 5C, 5D**). This last condition was, in addition to the continuous incubations, the one used for further analyses by XAS to follow the intracellular evolution of iron state. The rational was that repeated incubations with fresh iron-supplemented medium every hour might engender least oxidative events in the medium. Representative photographs of these incubation conditions show color change of the cell pellets (**Figure 5E**). First, a difference of color of the cell pellet between the three iron salts can be observed, and a slight color change also occurs within time, the ferric quinate cell pellet for instance becoming more brownish at day 7 than at the end of the 7h pulse.

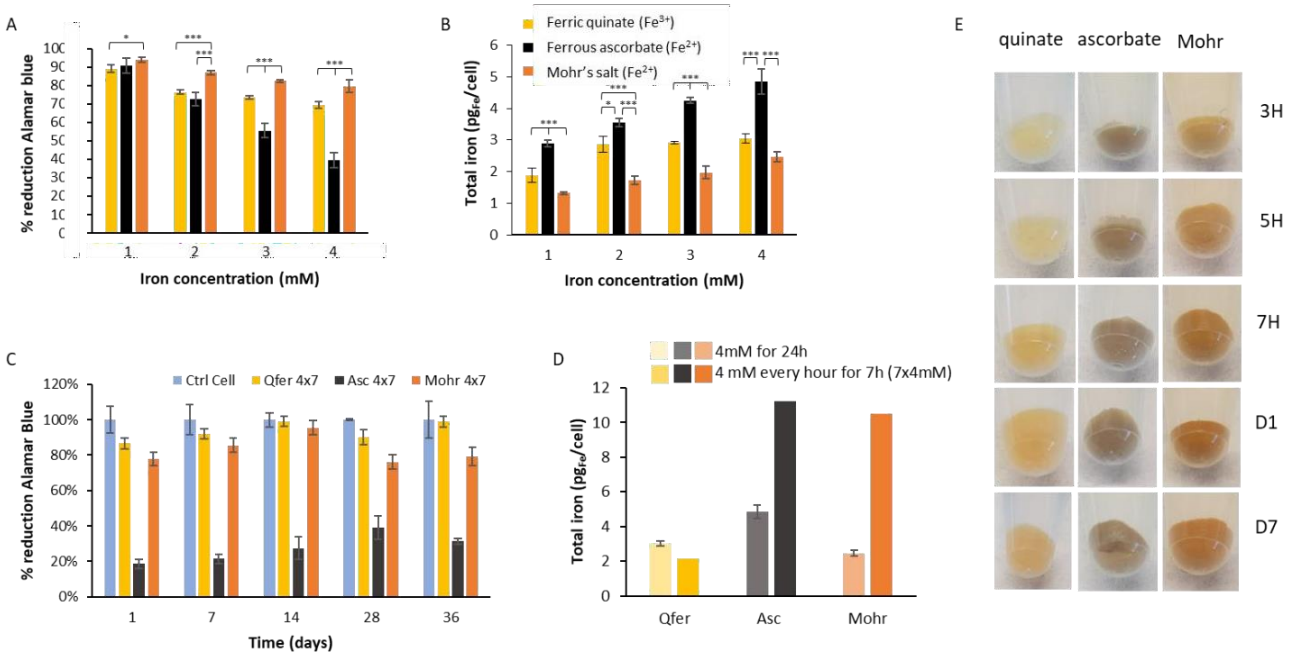

Figure 5: *Iron salts uptake and cytotoxicity on mMSC upon a pulse. Alamar Blue analysis was performed 1 week after the incubation pulse of ferric quinate, ferrous ascorbate or Mohr's salt at 1 to 4 mM supplemented with 2 mM citrate during 24h. (A) and the cellular iron uptake per cell was measured after 36 days via ICP-ES analysis. (B) Metabolic activity was followed during*

36 days after an iron salt incubation pulse at 4 mM with 2 mM citrate during 7 h with medium refreshed every hour. (C) and iron uptake at d ay 36 were compared to the one previously obtained at day 36 for a 4 mM incubation with 2 mM citrate during 24 h. (D) Images following the 7h incubation at 4 mM of iron salt were taken after 3h, 5h, 7h, 1 day and 7 days after the 7h pulse incubation (E).

Monitoring of biotransformations and biosynthesis of iron oxide-based nanoparticles in cells using X-ray absorption spectroscopy (XAS)

The biotransformations of iron within the cellular environment were monitored over time using X-ray absorption spectroscopy (XAS). XAS spectra at the near-edge structure (XANES) and extended X-ray absorption fine structure (EXAFS) regimes were measured at Fe (7112 eV) K-edges. Spectra of iron-loaded cells along their culture were determined in fluorescence mode and compared with initial iron-based precursors in solution and with reference samples (Fe_3O_4 (magnetite), γ-Fe_2O_3 (maghemite), $Fe_2O_3{\cdot}0.5H_2O$ (ferrihydrite)). *In situ* biotransformations of iron precursors were first assessed upon 36 days of continuous supplementation with 34 µM of either ferric quinate, ferrous ascorbate, or Mohr's salt, all with 2 mM citrate (**Figure 6**). Results show that only when incubated with Mohr's salt, the signal obtained for intracellular iron fully fits the ferrihydrite, being the main storage form of iron in the ferritin protein. Interestingly, the two other salts (ferric quinate and ferrous ascorbate), led to formation of a signal that resemble proportions of ferrihydrite accompanied with iron oxides. This result coincides with the formation of magnetic nanoparticles previously observed with the continuous incubation with ferric quinate. Overall, whichever the precursor (Fe^{2+} or Fe^{3+}), a change of iron valence toward Fe^{3+} is evidenced in cells.

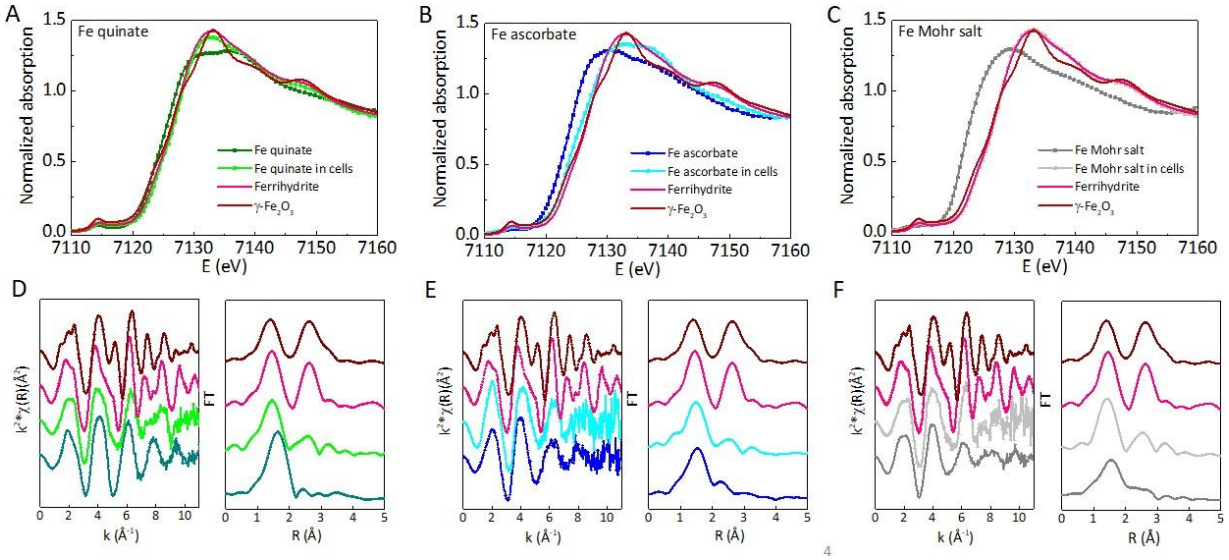

Figure 6: *X-ray absorption spectroscopy (XAS). XAS spectra at the near-edge structure (XANES) and extended X-ray absorption fine structure (EXAFS) regimes were measured at Fe (7112 eV)*

to study the evolution of different iron oxide-based nanomaterials within cells that were previously confined at different stages of maturation. Continuous incubation with either 34 µM ferric quinate, 34 µM ferrous ascorbate, or 34 µM Mohr's salt, all with 2 mM citrate. (A-C) XANES absorption spectra at the Fe K-edge of initial solutions (quinate, ascorbate, Mohr's salt). They display a shift of energy edge of iron in cells revealing an oxidation state of 3+ (on average) that matches with the existence of different proportions of maghemite and/or ferrihydrite (and other phases based on N, C, etc). (D-F) EXAFS signal and modulus of the FT of previous compounds.

XAS analyses were also achieved along and upon cell exposure to the 7 h pulse under repeated medium change every hour for 7h. Interestingly, in this second type of iron incubation, results obtained after 7 days of culture are quite different. *In situ* biotransformations of the initial iron precursors here seem to lead to formation of new structures, which could include iron oxide-compounds (magnetic), inside the cells already after 5 hours.

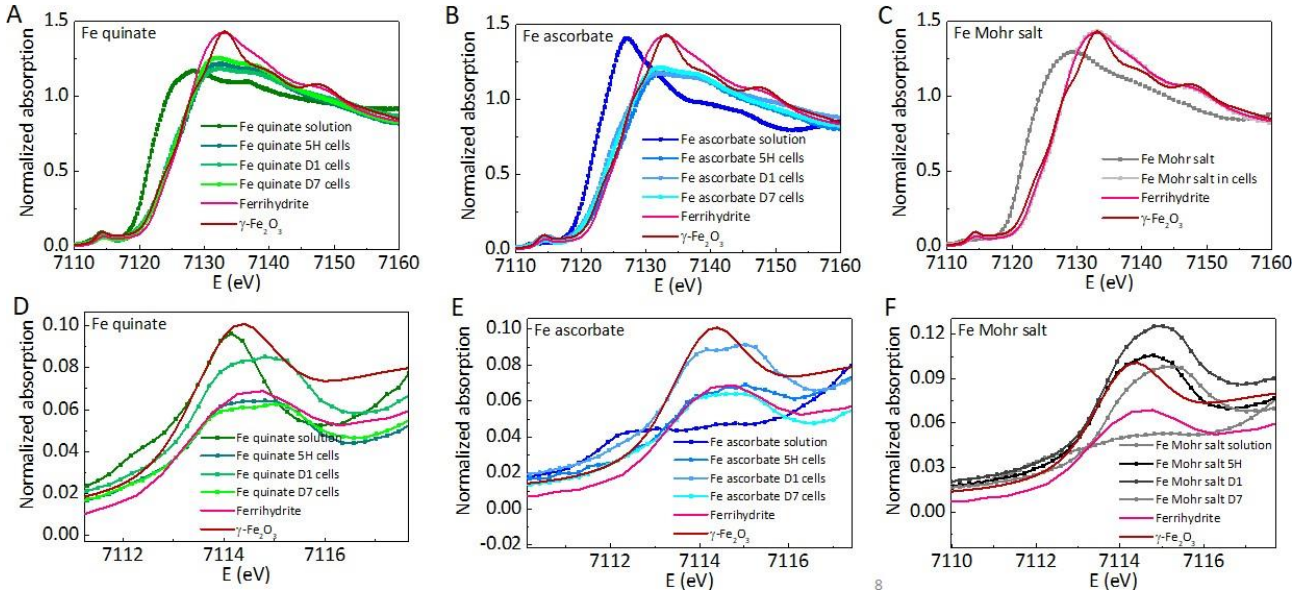

Figure 7: *XANES spectra at the Fe K-edge (7112 eV) of cells at different stages of the iron salt incubation pulse. Pulse incubation occurred with 4mM of ferric quinate (A,D), ferrous ascorbate (B,E) and Mohr's salt (C,F) supplemented with 2 mM Citrate for 7 hours, with medium repeated every hour. Initial solutions were compared to cells containing iron salt after 3h, 5h or 7hours of incubation and 1 or 7 days after these 7h incubation. They exhibit biotransformation in situ of the initial precursor.*

Discussion

The recent evidence that human stem cells are able to reshape magnetic nanoparticles, from synthetic or biological origin, into new magnetic nanoparticles, produced directly by the human cells, opens up to the question of a possible totally biological synthesis, using iron ions as precursors. Indeed, magnetic crystals have been identified in several organisms, including the magnetotactic bacteria, fishes, mollusks, birds, honeybees, and even humans[11,171]. In humans, they have been localized in specific organs[172,173]. The reason behind their presence is however still debated. They could be a remaining evolutionary feature allowing us to sense the geomagnetic field, as it has recently been demonstrated that Earth-strength magnetic fields do affect human alpha brain waves[174]. Several hypotheses have been emitted regarding magnetic nanoparticles as magnetoreceptors. Recently, a rotating magnetocaloric effect has been proposed, with heat generated by magnetizing nanoparticles that could activate nearby thermoreceptors[175].

In this present study, iron management by mouse and human MSC upon varying iron inputs and resulting biomineralization phenomena have been explored. Results emphasize that iron biomineralization and the formation of magnetic crystals can indeed be achieved from iron ions by mouse and also human stem cells. With such setup, the time to obtain magnetic cells is long, as it requires 21 days of culture for the human stem cells and 28 for the mouse ones, before reaching detectable magnetism values, remaining still low. It is however a first proof-of-concept that such a biosynthesis is possible. Moreover, a detailed analysis of iron entrance kinetics in mammalian stem cells is achieved. For instance, the role of citrate is explored.

Citrate is a molecule intertwined with iron metabolism in mammals as, to avoid adverse effects due to free iron ions such as Fenton reaction and the production of reactive oxygen species (ROS), or again to impede precipitation of Fe^{3+} as $Fe(OH)_3$, Fe^{3+} can complex with citrate[176]. Its presence has been reported in human blood plasma in concentrations of 0.1 mM, and it has been shown as an important iron ligand in patients suffering from iron overload[195]. Herein, the supplementation with citrate (2 mM) had a direct effect on cell growth, decreasing proliferation. Similar observations have been made in cancer cells; studies described a mitochondria-mediated apoptosis induced by high citrate concentration[177,178]. Citrate also resulted in higher magnetic moment per cell after 36 days of continuous incubation for the 16 C_o incubation. However, exact mechanism underlying these effects has not been resolved.

XANES and EXAFS experiments were performed at the Fe K-edge to quantitatively investigate the valence states and structural properties of the metal ions and the evolution of the ferrite

phases with time as a probe of the biotranformations that can occur in the biological environment. These two complimentary techniques, considered non-damaging, can thus reveal the short-range geometry and identify the phases[179,180,12]. Analyses were performed after 36 days of culture with continuous iron supplementation and upon a short 7h pulse of iron. For the pulses, analyses were performed on shorter time frames, up to day 7 only. Remarkably, in this case the signals never match the ferrihydrite, main storage structure within the ferritin. Instead, for all three salts and all times analyzed (5 hours, day 1, day 7), iron is under the oxidation state Fe^{3+} on average, and signal matches with the existence of different proportions of maghemite and ferrihydrite. Overall, these data demonstrate that iron is predominantly under the Fe^{3+} valence once within the cells, even with the Fe^{2+} ferrous ascorbate and Mohr's salt incubations. Analyses also confirm iron is not fully stored as ferrihydrite in the ferritin, except for the continuous incubation with Mohr's salt, but as mixed non-magnetic/magnetic forms. Such intracellular biotransformations seem to take place even on really short times (after 5 hours for the 4 mMrepeated pulse). This would have to be confirmed with additional magnetometry analyses oncell samples.

Acknowledgements

We thank Laure Cordier for the ICP-AES analyses at the Institut de Physique du Globe de Paris platform (IPGP), Christine Longin from INRA in Jouy-en-Josas for TEM preparation and analysis. We thank BM23 (ESRF, France) and CLAESS (ALBA, Spain) beamline staff for the support during the experiments.

Conclusion et Perspectives

Cette thèse s'est intéressée aux nanoparticules destinées à la médecine et plus particulièrement aux interactions qu'elles peuvent avoir sur leur environnement et réciproquement. Puisque ces nanomatériaux sont destinés à être en contact avec un environnement biologique, ils se doivent d'être robustes afin de mettre en action leurs propriétés thérapeutiques ou diagnostiques, mais aussi d'avoir une bonne biocompatibilité (prise en charge/élimination) pour éviter au maximum les effets néfastes à long terme sur le de reste de l'organisme.

Durant cette thèse, nous nous sommes intéressés en particulier aux transformations subies par les nanoparticules en milieu cellulaire notamment en réponse à une photothérapie, ainsi qu'à la mise en place et à l'optimisation de la production de nanoparticules biosynthétisées.

Malgré un nombre élevé d'essais précliniques impliquant les nanoparticules, peu aboutissent en essais cliniques. Cela peut s'expliquer par le manque d'informations sur le devenir de ces nanoparticules et leur impact à long terme dans le corps car les études se limitent généralement à la durée de l'action thérapeutique. Les nanoparticules d'oxyde de fer étudiées ici avaient pour but d'être le plus génériques possibles, pour pouvoir généraliser au mieux les résultats obtenus sur leur devenir, notamment la prise en charge par le métabolisme d'assimilation du fer de l'organisme, qui est parfaitement connue. Ces nanoparticules d'oxyde de fer de 7 à 9 nm de diamètre sont stabilisées par un recouvrement d'ions citrate, et leur cœur de maghémite ou de magnétite, est synthétisé soit par co-précipitation, soit par voie sol-gel non aqueuse[181]. Ces deux types de cœur ont déjà démontré une biodégradation progressive au sein des cellules. La première étape de la thèse a été de mettre en place un moyen rapide et fiable pour le suivi de la dégradation des nanoparticules, ce qui a été réalisé en participant au développement d'un senseur magnétique, équivalent à un magnétomètre de paillasse et qui permet de suivre l'évolution du magnétisme des nanoparticules en cellules vivantes, qui est la représentation des transformations subies par les nanoparticules.

Nous avons ensuite décrypté la dégradation de nos nanoparticules d'oxydes de fer en environnement aqueux, afin de déterminer dans un premier temps les conditions responsables de la biodégradation en cellule dans le but ultime de la contrôler. Le pH et la quantité d'agent chélateur ont été identifiés comme acteurs déterminants de la dégradation des nanoparticules, tandis que l'augmentation de la température agit comme activateur de celle-ci, ce qui a ouvert la piste intéressante quant à un contrôle à distance de la dégradation lié à l'utilisation des propriétés optiques que présentent nos nanoparticules d'oxyde de fer de magnétite, leur permettant d'agir comme source de chaleur en réponse à

une irradiation laser. Cette observation de l'accélération de la dégradation a également pu être identifié après internalisation de ces nanoparticules en cellules permettant ainsi un contrôle de la dégradation en cellule à distance par l'action d'un laser, tout en affectant peu la réaction d'hyperthermie sur les temps d'exposition réalisés (31min).

Cette dégradation accélérée de la nanoparticule implique aussi un relargage important d'ions ferreux issus de la dégradation, qui peuvent avoir une activité cytotoxique si la cellule n'arrive pas à les prendre en charge entièrement. C'est ce que nous avons également mis en évidence, après dégradation forcée de nanoparticules de magnétite, et un relargage massif d'ions Fe^{2+}, conduisant donc à une thérapie thermique, contrôlé spatialement et temporellement par le laser, qui peut être couplée à une réaction cytotoxique de Fenton à partir des ions ferreux issus de la dégradation.

Nous avons dans un deuxième temps voulu transposer cette dégradation sous laser à d'autres cœurs inorganiques. Nous nous sommes alors focalisés sur de nouvelles structures de nanoparticules àbase de platine (chapitre 2). En effet, l'une des caractéristiques que peut apporter le platine est sa stabilité en cellule. Une dégradation déclenchée par un laser serait donc totalement contrôlée. De plus, si cette dégradation relâche des ions Pt^{2+} cela pourrait mimer l'action de la chimiothérapie à base de cis-platine, très utilisée en cancérologie. Nous avons donc commencé par caractériser la nanoparticule de platine de deux types de structures : de petitesnanoparticules sphériques mono-cœurs et des nano-framboises multi-cœurs. Ces nanoparticules ont montré des capacités thermiques très différentes en solution, faibles pour les petites, très efficaces pour les framboises. Néanmoins, leurs chauffages identiques pour les deux types de nanomatériaux en environnement cellulaire s'expliquent par le confinement des petites nanoparticules mono-cœur dans les endosomes qui conduit à une agrégation///. Cette agrégation intra-endosomale ressemble en effet à la structure même de la nano-framboise. Enfin, nous avons pu observer des réarrangements au sein des nanoparticules de platine lié à l'irradiation laser à 808nm et 1 W/cm^2, signature d'un remodelage, mais pas nécessairement d'unerelargage d'ions platine.

Finalement, la troisième partie de cette thèse a été centrée autour des capacités récemment observées des cellules souches à bio-synthétiser des nanoparticules magnétiques biogéniques (chapitre 3). Ces premières observations de biosynthèse magnétique avaient été obtenues à partir des ions fer issues de la dégradation de nanoparticules synthétiques préalablement internalisées. Cette capacité des cellules souches à re-magnétiser des néo-nanoparticules avaient été alors associés à un possible mécanisme de détoxification des ions ferreux. L'émergence de magnétisme en cellule souche à partir de nanoparticules synthétiques de fer non magnétiques nous a incité à étudier la capacité des cellules souches à réaliser cette biosynthèse à partir uniquement de précurseurs de fer non magnétiques, comme peut le faire certains microorganismes. Inspirés par le modèle de la bactérie

magnétotactique, qui est capable d'une telle prouesse, nous avons mis en place des conditions d'internalisations de différents sels de fer pour tenter de comprendre cette capacité qu'ont les cellules souches à remobiliser le fer en excès en formant de petites nanoparticules d'oxyde de fer magnétiques, probablement au cœur de la ferritine. L'objectif était également d'optimiser cette biosynthèse afin d'obtenir des nanoparticules totalement biologiques, directement au cœur des cellules souches, utilisables en médecine régénératrice. Si cette partie a bien permis de démontrer que les cellules souches étaient capables de se magnétiser sous exposition à des précurseurs non magnétiques, cette biomagnétisation reste faible. De plus, pour l'instant, l'état d'oxydation du précurseur ou l'augmentation de la quantité de fer incubée n'ont montré que peu d'effets sur la bioproduction. Cependant, nous avons pu voir que différents protocoles pouvaient agir sur le comportement de la cellule à traiter cet afflux de Fer.

Pour conclure, cette thèse a mis en avant l'utilisation d'une irradiation laser pour le contrôle du traitement par hyperthermie et des transformations subies par la nanoparticule une fois dans l'environnement cellulaire. En effet, l'environnement interagit avec la nanoparticule, et on a pu voir que le confinement peut provoquer une augmentation de la réponse thermique liée à l'exposition à un laser, ou encore que l'environnement puisse induire la dégradation des nanoparticules. Ainsi, en connaissant mieux les environnements que côtoient les nanoparticules lors de leur internalisation cellulaire et leurs effets, il devient possible de manipuler l'état structurel des nanoparticules. Les perspectives de nouvelles nanoparticules biosynthétisées ouvrent de nouvelles perspectives biomédicales, notamment pour l'utilisation de nanoparticules biocompatibles à très long terme. Plusieurs perspectives se dégagent de ce travail de thèse :

Au niveau de la dégradation sous stimulation laser, la suite logique serait d'essayer d'optimiser les nanoparticules à base de Pt pour le traitement du cancer, pour délivrer une action tout-en-un qui combinerait la mort cellulaire de type ferroptose et la thérapie photothermique sous exposition laser. Cela constituerait une première dans l'utilisation de nanomatériaux à base de Pt, qui pourrait faire lien avec les traitements chimio-thérapeutiques à base de Pt (cis-platine délivrant des Pt^{2+} cytotoxique). Cependant, la dégradation laser des nanoparticules de magnétite pourrait également être poursuivie, en étudiant par exemple l'impact de la taille, de la structure ou de formes différentes afin de pouvoir optimiser l'action d'hyperthermie avec un relargage plus important d'ions fer, toujours dans le but d'une double action thérapeutique directement dirigée vers une tumeur. Et finalement, notre collaborateur Yoann LALATONNE est actuellement en train de mettre en place une synthèse de nanoparticules quasiment identique aux magnétites et maghémites qu'il a produit pour cette thèse, mais constituées d'un cœur de fer métallique (Fe0). De manière remarquable, ces nanoparticules

ont un pouvoir chauffant encore meilleur que celles de magnétite, et l'on pourrait supposer que leur dégradation pourrait conduire à des cascades d'oxydation du Fer(0) au Fer(III) avec une action ferrotoxique amplifiée.

Au niveau de la biosynthèse magnétique, ces études continuent avec le démarrage de la thèse de Guilhem CURE, actuellement en stage de Master 2, thèse qui sera co-dirigée par Claire WILHELM et Aurore VAN DE WALLE. Un des objectifs sera de transposer la biosynthèse étudiée ici en cellules souches de souris vers des cellules souches humaines, soit mésenchymateuses (hMSC) soit induites (iPS). L'autre but sera de continuer les transfections pour la surexpression permanente ou transitoire de gènes impliqués dans le métabolisme du Fer comme de gènes analogues de la bactérie magnétotactique, non seulement pour obtenir des lignées de cellules souches biomagnétiques, mais aussi pour disséquer le mécanisme responsable de cette biosynthèse en identifiant des gènes impliqués. Une étape importante dans la suite de ce projet sera d'adapter le senseur magnétique à un bioréacteur qui permette le suivi magnétique en temps réel mais sur des temps longs, pendant la culture et la maturation des cellules souches, exposées à différents types, différentes concentrations, et différents temps d'incubation de sels de fer. C'est l'objectif du projet ERC Proof of Concept BioMag porté par Claire WILHELM et Aurore VAN DE WALLE, et qui démarre en octobre 2022. L'objectif final de l'étude sur la production de nanoparticules biosynthétisées reste double : mieux appréhender d'une part le devenir à long terme des nanoparticules d'oxyde de fer dans l'organisme et d'autre part de produire des cellules biomagnétiques de biocompatibilité maximale pour la médecine régénératrice.

-

Références

[1] Wu, W., He, Q. & Jiang, C. Magnetic Iron Oxide Nanoparticles: Synthesis and Surface Functionalization Strategies. Nanoscale Res Lett 3, 397–415 (2008).

[2] Wu, W., Wu, Z., Yu, T., Jiang, C. & Kim, W.-S. Recent progress on magnetic iron oxide nanoparticles: synthesis, surface functional strategies and biomedical applications. Sci Technol Adv Mater 16, 023501 (2015)

[3] Arami, H., Khandhar, A., Liggitt, D. & Krishnan, K. M. In vivo delivery, pharmacokinetics, biodistribution and toxicity of iron oxide nanoparticles. Chem. Soc. Rev. 44, 8576–8607 (2015)

[4] Reddy, L. H., Arias, J. L., Nicolas, J. & Couvreur, P. Magnetic nanoparticles: design and characterization, toxicity and biocompatibility, pharmaceutical and biomedical applications. Chem. Rev. 112, 5818–5878 (2012).

[5] Ventola, C. L. Progress in Nanomedicine: Approved and Investigational Nanodrugs. P T 42, 742– 755 (2017).

[6] Anselmo, A. C. & Mitragotri, S. A Review of Clinical Translation of Inorganic Nanoparticles. AAPS J 17, 1041–1054 (2015).

[7] Vallabani, N. V. S. & Singh, S. Recent advances and future prospects of iron oxide nanoparticles in biomedicine and diagnostics. 3 Biotech 8, (2018).

[8] Aisen, P., Wessling-Resnick, M., Leibold, E. A. Iron Metabolism. Curr. Opin. Chem. Biol. 1999, 3 (2), 200−206.

[9] Kohgo, Y., Ikuta, K., Ohtake, T. *et al.* Body iron metabolism and pathophysiology of iron overload. *Int J Hematol* **88,** 7–15 (2008).

[10] Aisen, P., Enns, C., Wessling-Resnick, M., 2001. Chemistry and biology of eukaryotic iron metabolism. Int. J. Biochem. Cell Biol. 33, 940–959

[11] Kirschvink JL, Kobayashi-Kirschvink A, Woodford BJ (1992) Magnetite biomineralization in the human brain. Proc Natl Acad Sci USA 89(16):7683–7687

[12] A. Curcio, et al., Transformation Cycle of Magnetosomes in Human Stem Cells: from Degradation to Biosynthesis of Magnetic Nanoparticles Anew. ACS Nano 14, 1406–1417 (2019).

[13] A. Van de Walle, et al., Biosynthesis of magnetic nanoparticles from nano-degradation products revealed in human stem cells. Proc. Natl. Acad. Sci. U.S.A. 116, 4044–4053 (2019).

[14] Sangnier, A. P., Van de Walle, A. B., Curcio, A., Le Borgne, R., Motte, L., Lalatonne, Y., Wilhelm, C. Impact of Magnetic Nanoparticle Surface Coating on Their Long-Term Intracellular Biodegradation in Stem Cells. Nanoscale 2019, 11, 16488– 16498

[15] Barosi, A., Dunkel, P., Guénin, E., Lalatonne, Y., Zeitoun, P., Fitton, I., Journé, C., Bravin, A., Maruani, A., Dhimane, H., Motte, L., Dalko, P. I. Synthesis and Activation of an Iron Oxide Immobilized Drug-Mimicking Reporter under Conventional and Pulsed X-Ray Irradiation Conditions. RSC Adv. 2020, 10, 3366– 3370

[16] Mazuel, F ; Espinosa, A , Luciani, N , Reffay, M , Borgne, RL , Motte, L , et al. Massive intracellular biodegradation of iron oxide nanoparticles evidenced magnetically at single-endosome and tissue levels. ACS Nano. 2016 ,10:7627–38

[17] Kolosnjaj-Tabi, J, et al. Biotransformations of magnetic nanoparticles in the body. Nano Today 2016, 11:280–284.

[18] Van de Walle, A., Kolosnjaj-Tabi, J., Lalatonne, Y., Wilhelm, C. Ever-Evolving Identity of Magnetic Nanoparticles within Human Cells, the Interplay of Endosomal Confinement, Degradation, Storage, and Neo-Crystallization. Acc. Chem. Res. 2020, 53 (10), 2212– 2224,

[19] Luzio, J. P., Pryor, P. R. & Bright, N. A. Lysosomes: fusion and function. Nature Reviews Molecular Cell Biology 8, 622–632 (2007)

[20] Volatron, J. et al. Ferritin Protein Regulates the Degradation of Iron Oxide Nanoparticles. Small 13, (2017).

[21] Soenen, S. J., Parak, W. J., Rejman, J. & Manshian, B. (Intra)Cellular Stability of Inorganic Nanoparticles: Effects on Cytotoxicity, Particle Functionality, and Biomedical Applications. Chem. Rev. 115, 2109–2135 (2015).

[22] Levy, M., Lagarde, F., Maraloiu, V.-A., Blanchin, M.-G., Gendron, F., Wilhelm, C., Gazeau, F. Degradability of Superparamagnetic Nanoparticles in a Model of Intracellular Environment: Follow-up of Magnetic, Structural and Chemical Properties. Nanotechnology 2010, 21 (39), 395103

[23] Gutiérrez, L., Romero, S., da Silva, G.B., Costo, R., Vargas, M.D., Ronconi, C.M., Serna, C.J., Veintemillas-Verdaguer, S., del Puerto Morales, M. Degradation of magnetic nanoparticles mimicking lysosomal conditions followed by AC susceptibility. Biomed. Eng./Biomed. Tech. 2015, 60, 417–425.

[24] Soukup, D., Moise, S., Cespedes, E., Dobson, J., Telling, N. D.´ In Situ Measurement of Magnetization Relaxation of Internalized Nanoparticles in Live Cells. ACS Nano 2015, 9, 231−240

[25] Knovich, M. A., Storey, J. A., Coffman, L. G. & Torti, S. V. Ferritin for the Clinician. Blood Rev 23, 95–104 (2009)

[26] Horvathova, M., Ponka, P. & Divoky, V. Molecular basis of hereditary iron homeostasis defects. Hematology 15, 96–111 (2010).

[27] Zarjou, A. et al. Ferritin ferroxidase activity: A potent inhibitor of osteogenesis. Journal of Bone and Mineral Research 25, 164–172 (2010).

[28] Harrison, P. M., & Arosio, P. (1996). The ferritins: molecular properties, iron storage function and cellular regulation. Biochimica et Biophysica Acta (BBA)-Bioenergetics, 1275(3), 161-203.

[29] Naqvi, S. et al. Concentration-dependent toxicity of iron oxide nanoparticles mediated by increased oxidative stress. Int J Nanomedicine 5, 983–989 (2010).

[30] Hussain, S. M., Hess, K. L., Gearhart, J. M., Geiss, K. T. & Schlager, J. J. In vitro toxicity of nanoparticles in BRL 3A rat liver cells. Toxicol In Vitro 19, 975–983 (2005).

[31] Jeng, H. A. & Swanson, J. Toxicity of metal oxide nanoparticles in mammalian cells. J Environ Sci Health A Tox Hazard Subst Environ Eng 41, 2699–2711 (2006).

[32] Karlsson, H. L., Gustafsson, J., Cronholm, P. & Möller, L. Size-dependent toxicity of metal oxide particles-a comparison between nano- and micrometer size. Toxicol. Lett. 188, 112–118 (2009)

[33] Kunzmann, A. et al. Efficient internalization of silica-coated iron oxide nanoparticles of different sizes by primary human macrophages and dendritic cells. Toxicol. Appl. Pharmacol. 253, 81–93 (2011).

[34] Beik, J, Abed, Z, Ghoreishi, FS, Hosseini-Nami, S, Mehrzadi, S, Shakeri-Zadeh, A. et al. Nanotechnology in hyperthermia cancer therapy: from fundamental principles to advanced applications. J Control Release. 2016, 235:205–21

[35] Espinosa, A., Kolosnjaj-Tabi, J., Abou-Hassan, A., Sangnier, A. P., Curcio, A., Silva, A. K. A., Di Corato, R., Neveu, S., Pellegrino, T., Liz-Marzán, L. M. et al. Magnetic (Hyper)thermia or photothermia? Progressive comparison of iron oxide and gold nanoparticles heating in water, in cells, and in vivo. Adv. Funct. Mater. 2018, 28, 1803660.

[36] Plan Sangnier, A., Preveral, S., Curcio, A., Silva, A. K. A., Lefèvre, C. T., Pignol, D., Lalatonne, Y., Wilhelm, C. Targeted thermal therapy with genetically engineered magnetite magnetosomes@RGD: Photothermia is far more efficient than magnetic hyperthermia. J. Control. Release 2018, 279, 271–281.

[37] Chu, M. Q., Shao, Y. X., Peng, J. L., Dai, X. Y., Li, H. K., Wu, Q. S., Shi, D. L. Near-infrared laser light mediated cancer therapy by photothermal effect of Fe3O4 magnetic nanoparticles. Biomaterials 2013, 34, 4078–4088.

[38] Zhou, Z. G., Sun, Y. N., Shen, J. C., Wei, J., Yu, C., Kong, B., Liu, W., Yang, H., Yang, S. P., Wang, W. Iron/iron oxide core/shell nanoparticles for magnetic targeting MRI and near-infrared photothermal therapy. Biomaterials 2014, 35, 7470–7478

[39]Shen, S., Wang, S., Zheng, R., Zhu, X. Y., Jiang, X. G., Fu, D. L., Yang, W. L. Magnetic nanoparticle clusters for photothermal therapy with near-infrared irradiation. Biomaterials 2015, 39, 67–74.

[40] Brites, C. D. S., Lima, P. P., Silva, N. J. O., Millan, A., Amaral, V.́ S., Palacio, F., Carlos, L. D., A Luminescent Molecular Thermometer for Long-Term Absolute Temperature Measurements at the Nanoscale. Adv. Mater. 22, (40), 4499-4504.

[41] Polo-Corrales, L., Rinaldi, C. Monitoring iron oxide nanoparticle surface temperature in an alternating magnetic field using thermoresponsive fluorescent polymers. J. Appl. Phys. 2012, 111 (7), 07B334.

[42] Espinosa, A., Castro, G. R., Reguera, J., Castellano, C., Castillo, J., Camarero, J., Wilhelm, C., García, M. A., Muñoz-Noval, Á. Photoactivated Nanoscale Temperature Gradient Detection Using X-Ray Absorption Spectroscopy as a Direct Nanothermometry Method. Nano Lett. 2020, 21, 769– 777

[44] Souza, G. R., Molina, J. R., Raphael, R. M., Ozawa, M. G., Stark, D. J., Levin, C. S., Bronk, L. F., Ananta, J. S., Mandelin, J., Georgescu, M. M. et al. Three-dimensional tissue culture based on magnetic cell levitation. Nat. Nanotechnol, 2010, 5, 291–296.

[45] Mattix, B., Olsen, T. R., Gu, Y., Casco, M., Herbst, A., Simionescu, D. T., Visconti, R. P., Kornev, K. G., Alexis, F. Biological magnetic cellular spheroids as building blocks for tissue engineering. Acta Biomater. 2014, 10, 623–629.

[46] Du, V. Du, Luciani, N, Richard, G. Mary, G, Gay,C, Mazuel,F, Reffay,M, Menasché,P, Agbulut, O, Wilhelm,C, A 3D magnetic tissue stretcher for remote mechanical control of embryonic stem cell differentiation, Nat. Commun., 2017, 8, 400

[47] Fayol, D., Frasca, G., Le Visage, C., Gazeau, F., Luciani, N., Wilhelm, C. Use of Magnetic Forces to Promote Stem Cell Aggregation During Differentiation, and Cartilage Tissue Modeling. Adv. Mater. 2013, 25, 2611−2616.

[48] Mattix, B. M., Olsen, T. R., Casco, M., Reese, L., Poole, J. T., Zhang, J., Visconti, R. P., Simionescu, A., Simionescu, D. T., Alexis, F. Janus Magnetic Cellular Spheroids for Vascular Tissue Engineering. Biomaterials 2014, 35, 949−960.

[49] Du, V., Fayol, D., Reffay, M., Luciani, N., Bacri, J., Gay, C., Wilhelm, C. Magnetic Engineering of Stable Rod-Shaped Stem Cell Aggregates: Circumventing the Pitfall of Self-Bending. Integr. Biol. 2015, 7, 170−177.

[50] Cazares-Cortes, E., Cabana, S., Boitard, C., Nehlig, E., Griffete, N., Fresnais, J., Wilhelm, C., Abou-Hassan, A., Ménager, C. Recent insights in magnetic hyperthermia: From the “hot-spot” effect for local delivery to combined magneto-photo-thermia using magneto-plasmonic hybrids. Adv. Drug Deliv. Rev. 2019, 138, 233–246.

[51] Carregal-Romero, S., Guardia, P., Yu, X., Hartmann, R., Pellegrino, T., Parak, W. J. Magnetically triggered release of molecular cargo from iron oxide nanoparticle loaded microcapsules. Nanoscale 2015, 7, 570–576.

[52] Tong, S., Zhu, H., Bao, G. Magnetic iron oxide nanoparticles for disease detection and therapy. *Mater. Today* **2019**, *31*, 86–99

[53] Wang, YX, Hussain, SM, Krestin, GP (2001) Superparamagnetic iron oxide contrast agents: Physicochemical characteristics and applications in MR imaging. Eur Radiol 11:2319–2331.

[54] Blanco-Andujar, C., Walter, A., Cotin, G., Bordeianu, C., Mertz, D., Felder-Flesch, D., Begin-Colin, S. Design of iron oxide-based nanoparticles for MRI and magnetic hyperthermia. Nanomedicine 2016, 11, 1889–1910.

[55] Schwenk, MH, Ferumoxytol: A new intravenous iron preparation for the treatment of iron deficiency anemia in patients with chronic kidney disease. Pharmacotherapy 2010, 30:70–79.

[56] Mejías, R., Gutierrez, L., Salas, G., Pe´ rez-Yagu´ e, S., Zotes, T. M., Lazaro, F. J., Morales, M. P., Barber, D. F. Long Term´ Biotransformation and Toxicity of Dimercaptosuccinic Acid-Coated Magnetic Nanoparticles Support Their Use in Biomedical Applications. J. Controlled Release 2013, 171, 225−233.

[57] Feliu, N., Docter, D., Heine, M., del Pino, P., Ashraf, S., Kolosnjaj-Tabi, J., Macchiarini, P., Nielsen, P., Alloyeau, D., Gazeau, F., et al. In Vivo Degeneration and the Fate of Inorganic Nanoparticles. Chem. Soc. Rev. 2016, 45, 2440−2457.

[58] 19. Roy, S., Liu, Z., Sun, X., Gharib, M., Yan, H., Huang, Y., Megahed, S., Schnabel, M., Zhu, D., Feliu, N. Assembly and Degradation of Inorganic Nanoparticles in Biological Environments. Bioconjugate Chem. 2019, 30 (11), 2751−2762.

[59] Ostaszewska,T, Śliwiński, J, Kamaszewski, M, Sysa, P, Chojnacki, M, Environ. Sci. Pollut. Res. Int., 2018, 25, 908–915, (b) A. M. Alkilany, P. K. Nagaria, C. R. Hexel, T. J. Shaw, C. J. Murphy and M. D. Wyatt, Small, 2009, 5, 701–708

[60] Nel, A., Xia, T., Madler, L., Li, N. Toxic Potential of Materials at the Nanolevel. Science 2006, 311, 622−627

[61] Stepien, G., Moros, M., Pérez-Hernández, M., Monge, M., Gutiérrez, L., Fratila, R.M., las Heras, M.d., Menao Guillen, S., Puente Lanzarote, J.J., Solans, C. Effect of surface chemistry and associated protein corona on the long-term biodegradation of iron oxide nanoparticles in vivo. ACS Appl. Mater. Interfaces 2018, 10, 4548–4560.

[62] Ashraf, S., Taylor, A., Sharkey, J., Barrow, M., Murray, P., Wilm, B., Poptani, H., Rosseinsky, M.J., Adams, D.J., Lévy, R. In vivo fate of free and encapsulated iron oxide nanoparticles after injection of labelled stem cells. Nanoscale Adv. 2019, 1, 367–377.

[63] Van de Walle, A., Fromain, A., Sangnier, A. P., Curcio, A., Lenglet, L., Motte, L., Lalatonne, Y., Wilhelm, C. Real-Time in Situ Magnetic Measurement of the Intracellular Biodegradation of Iron Oxide Nanoparticles in a Stem Cell-Spheroid Tissue Model. *Nano Res.* 2020, *13*, 467–476

[64] Pham, B. T. T., Colvin, E. K., Pham, N. T. H., Kim, B. J., Fuller, E. S., Moon, E. A., Barbey, R., Yuen, S., Rickman, B. H., Bryce, N. S. et al. Biodistribution and clearance of stable superparamagnetic maghemite iron oxide nanoparticles in mice following intraperitoneal administration. Int. J. Mol. Sci. 2018, 19, 205.

[65] Bargheer, D., Giemsa, A., Freund, B., Heine, M., Waurisch, C., Stachowski, G. M., Hickey, S. G., Eychmüller, A., Heeren, J., Nielsen, P. The distribution and degradation of radiolabeled superparamagnetic iron oxide nanoparticles and quantum dots in mice. Beilstein J. Nanotechnol. 2015, 6, 111–123.

[66] Freund, B., Tromsdorf, U. I., Bruns, O. T., Heine, M., Giemsa, A., Bartelt, A., Salmen, S. C., Raabe, N., Heeren, J., Ittrich, H. et al. A simple and widely applicable method to 59Fe-radiolabel monodisperse superparamagnetic iron oxide nanoparticles for in vivo quantification studies. ACS Nano 2012, 6, 7318–7325.

[67] Laskar, A, Ghosh, M, Khattak, SI, Li, W, Yuan, X-M Degradation of superparamagnetic iron oxide nanoparticle-induced ferritin by lysosomal cathepsins and related immune response. Nanomedicine (Lond) 2012, 7:705–717.

[68] Weissleder, R, et al. Superparamagnetic iron oxide: Pharmacokinetics and toxicity. AJR Am J Roentgenol 1989, 152:167–173

[69] Lartigue, L , et al. Biodegradation of iron oxide nanocubes: High-resolution in situ monitoring. ACS Nano 2013, 7:3939–3952.

[70] Ruiz, A, et al. Biotransformation of magnetic nanoparticles as a function of coating in a rat model. Nanoscale 2015, 7:16321–16329.

[71] Liu, X., Theil, E. C. Ferritins: Dynamic Management of Biological Iron and Oxygen Chemistry. Acc. Chem. Res. 2005, 38, 167− 175

[72] Liu, G., Gao, J., Ai, H., Chen, X. Applications and Potential Toxicity of Magnetic Iron Oxide Nanoparticles. Small 2013, 9 (9−10), 1533−1545.

[73] Sabella, S., Carney, R. P., Brunetti, V., Malvindi, M. A., Al-Juffali, N., Vecchio, G., Janes, S. M., Bakr, O. M., Cingolani, R., Stellacci, F. A General Mechanism for Intracellular Toxicity of Metal-Containing Nanoparticles. Nanoscale 2014, 6 (12), 7052−7061.

[74] Angele-Martinez, C, Nguyen, KV, Ameer, FS, Anker, JN, Brumaghim, JL. Reactive oxygen species generation by copper (II) oxide nanoparticles determined by DNA damage assays and EPR spectroscopy. Nanotoxicology. 2017, 11:278–88

[75] Robertson, CA, Evans, DH, Abrahamse, H. Photodynamic therapy (PDT): a short review on cellular mechanisms and cancer research applications for PDT. J Photochem Photobiol. 2009, 96:1–8

[76] Shan, X., Li, S., Sun, B., Chen, Q., Sun, J., He, Z., Luo, C. Ferroptosis-Driven Nanotherapeutics for Cancer Treatment. J. Controlled Release 2020, 319, 322−332.

[77] Liang, C., Zhang, X., Yang, M. & Dong, X. Recent progress in ferroptosis inducers for cancer therapy. Adv. Mater. Weinh. 2019, 31, 1904197

[78] Xu, T., Ding, W., Ji, X., Ao, X., Liu, Y., Yu, W., Wang, J. Molecular Mechanisms of Ferroptosis and Its Role in Cancer Therapy. J. Cell. Mol. Med. 2019, 23, 4900−4912

[79] Blanco-Andujar, C., Teran, F. J., Ortega, D. Current outlook and perspectives on nanoparticle-mediated magnetic hyperthermia. In Iron Oxide Nanoparticles for Biomedical Applications. Mahmoudi, M., Laurent, S., Eds., Metal Oxides: Elsevier, 2018, pp 197–245.

[80] Sandre, O., Genevois, C., Garaio, E., Adumeau, L., Mornet, S., Couillaud, F. In vivo imaging of local gene expression induced by magnetic hyperthermia. Genes 2017, 8, 61.

[81] Skotland, T., Sontum, P. C., Oulie, I. In Vitro Stability Analyses as a Model for Metabolism of Ferromagnetic Particles (Clariscan), a Contrast Agent for Magnetic Resonance Imaging. J. Pharm. Biomed. Anal. 2002, 28, 323−329.

[82] Richard, S , Eder, V , Caputo, G , Journé, C , Ou, P , Bolley, J , Louedec, L , Guenin, E , Motte, L , Pinna, N. et al. USPIO size control through microwave nonaqueous sol-gel method for neoangiogenesis T2 MRI contrast agent. Nanomedicine (Lond) 2016, 11, 2769–2779

[83] Espinosa, A., Bugnet, M., Radtke, G., Neveu, S., Botton, G. A., Wilhelm, C., Abou-Hassan, can magneto-plasmonic nanohybrids efficiently combine photothermia with magnetic hyperthermia? A. Nanoscale 2015, 7, 18872–18877

[84] Benyettou, F., Guenin, E., Lalatonne, Y., Motte, Microwave assisted nanoparticle surface functionalization L. Nanotechnology 2011, 22, 055102.

[85] Saeed, M, Ren, W, Wu, A. Therapeutic applications of iron oxide-based nanoparticles in cancer: basic concepts and recent advances. Biomat Sci. 2018, 6:708–25

[86] Dong, J., Zink, J. I. Taking the temperature of the interiors of magnetically heated nanoparticles. ACS Nano 2014, 8 (5), 5199− 5207.

[87] Riedinger, A., Guardia, P., Curcio, A., Garcia, M. A., Cingolani, R., Manna, L., Pellegrino, T. Subnanometer local temperature probing and remotely controlled drug release based on azofunctionalized iron oxide nanoparticles. Nano Lett. 2013, 13 (6), 2399−2406.

[88] Cazares-Cortes, E., Espinosa, A., Guigner, J.-M., Michel, A., Griffete, N., Wilhelm, C., Menager, C. Doxorubicin intracellulaŕ remote release from biocompatible oligo (ethylene glycol) methyl ether methacrylate-based magnetic Nanogels triggered by magnetic hyperthermia. ACS Appl. Mater. Interfaces 2017, 9 (31), 25775− 25788

[89] Yang, J.-M., Yang, H., Lin, L. Quantum Dot Nano Thermometers Reveal Heterogeneous Local Thermogenesis in Living Cells. ACS Nano 2011, 5 (6), 5067−5071.

[90] Okabe, K., Inada, N., Gota, C., Harada, Y., Funatsu, T., Uchiyama, S. Intracellular temperature mapping with a fluorescent polymeric thermometer and fluorescence lifetime imaging microscopy. Nat. Commun. 2012, 3 (705), 1−9.

[91] Dias, J. T., Moros, M., del Pino, P., Rivera, S., Grazu, V., de lá Fuente, J. M. DNA as a molecular local thermal probe for the analysis of magnetic hyperthermia. Angew. Chem., Int. Ed. 2013, 52 (44), 11526−11529.

[92] Creixell, M., Bohorquez, A. C., Torres-Lugo, M., Rinaldi, C.́ EGFR-Targeted Magnetic Nanoparticle Heaters Kill Cancer Cells without a Perceptible Temperature Rise. ACS Nano 2011, 5 (9), 7124−7129.

[93] Hirschhaeuser, F., Menne, H., Dittfeld, C., West, J., MuellerKlieser, W., Kunz-Schughart, L. A. Multicellular Tumor Spheroids: An Underestimated Tool Is Catching up Again. J. Biotechnol. 2010, 148, 3−15.

[94] Xu, X., Farach-Carson, M. C., Jia, X. Three-Dimensional In Vitro Tumor Models for Cancer Research and Drug Evaluation. Biotechnol. Adv. 2014, 32, 1256−1268.

[95] Perez, J.E., Nagle, I., Wilhelm, C. Magnetic molding of tumor spheroids: Emerging model for cancer screening. Biofabrication 2020, 13, 015018

[96] Gilazieva, Z., Ponomarev, A., Rutland, C., Rizvanov, A., Solovyeva, V. Promising applications of tumor spheroids and organoids for personalized medicine. Cancers 2020, 12, 2727

[97] Schweiger, C., Hartmann, R., Zhang, F., Parak, W. J., Kissel, T., Rivera Gil, P. Quantification of the Internalization Patterns of Superparamagnetic Iron Oxide Nanoparticles with Opposite Charge. J. Nanobiotechnol. 2012, 10, 28.

[98] Lynch, I , Dawson, KA. Protein-nanoparticle interactions. Nanotoday. 2008 ,3(1–2):40–47

[99] Patila S, Sandberg A, Heckert E, Self W, Sea S. Protein adsorption and cellular uptake of cerium oxide nanoparticles as a function of zeta potential. Biomaterials 2007 , 28: 4600–4607.

[100] Lee, J.M., Choi, J.W., Ahrberg, C.D., Choi, H.W., Ha, J.H., Mun, S.G., Mo, S.J., Chung, B.G. Generation of tumor spheroids using a droplet-based microfluidic device for photothermal therapy. Microsyst. Nanoeng. 2020, 6, 1–10.

[101] Emami, B, Song, CW, Physiological mechanisms in hyperthermia: a review. *Int J Radiat Oncol Biol Phys.* 1984,10:289–295.

[102] Dixon, SJ , Lemberg, KM , Lamprecht, MR, Skouta, R, Zaitsev, EM, Gleason, CE, et al. Ferroptosis: an iron-dependent form of nonapoptotic cell death. *Cell*. 2012,129:1060-72

[103] Singh, N , Jenkins, GJS , Asadi, R, Doak, SH, Potential toxicity of superparamagnetic iron oxided nanoparticles (SPION). *Nano Rev*. 2010,1:5358

[104] Zheng, H , Jiang, J , Xu, S, Liu, W, Xie, Q, Cai, X, et al. Nanoparticle-induced ferroptosis : detection methods, mechanisms and applications. Nanoscale. (2021) 13 2266-2285.10.1039

[105] Stepanov, A. L., Golubev, A. N., Nikitin, S. I., Osin, Y. N. A review on the fabrication and properties

[106] Huang, X., El-Sayed, I. H., Qian, W. & El-Sayed, M. A. *J. Am. Chem. Soc*. 128, 2115–2120 (2006).

[107] Hirsch, L. R. et al. *Proc. Natl. Acad. Sci*. U. S. A. 100, 13549–13554 (2003).

[108] D. Chen, S. Gao, W. Ge, Q. Li, H. Jiang and X. Wang, *RSC Adv.*, 2014, **4**, 40141–40145

[109] D. Chen, C. Zhao, J. Ye, Q. Li, X. Liu, M. Su, H. Jiang, C. Amatore, M. Selke and X. Wang, *ACS Appl. Mater. Interfaces*, 2015, **7**, 18163–18169

[110] X. Zheng, W. Chen, P. Cui, Z. Wang and W. Zhang, *RSC Adv.*, 2014, **4**, 58489–58494

[111] W. Chen, X. Zheng, S. Li, W. Zhang, X. Wen, L. Yue and J. Wang, *J. Nanopart. Res.*, 2015, **17**, 1–10

[112] A. Higuchi, Y.-D. Siao, S.-T. Yang, P.-V. Hsieh, H. Fukushima, Y. Chang, R.-C. Ruaan and W.-Y. Chen, *Anal. Chem.*, 2008, **80**, 6580–6586

[113] I. Taurino, G. Sanzó, F. Mazzei, G. Favero, G. De Micheli and S. Carrara, *Sci. Rep.*, 2015, **5**, 15277

[114] S. Hrapovic, Y. Liu, K. B. Male and J. H. T. Luong, *Anal. Chem.*, 2004, **76**, 1083–1088

[115] M. Moglianetti, E. De Luca, D. Pedone, R. Marotta, T. Catelani, B. Sartori, H. Amenitsch, S. F. Retta and P. P. Pompa, *Nanoscale*, 2016, **8**, 3739–3752

[116] H. Hosaka, R. Haruki, K. Yamada, C. Böttcher and T. Komatsu, *PLoS One*, 2014, **9**, e110541

[117] S. Shibuya, Y. Ozawa, K. Watanabe, N. Izuo, T. Toda, K. Yokote and T. Shimizu, *PLoS One*, 2014, **9**, e109288

[118] J. W. J. Bergs, M. G. Wacker, S. Hehlgans, A. Piiper, G. Multhoff, C. Rödel and F. Rödel, *Biochim. Biophys. Acta, Rev. Cancer*, 2015, **1856**, 130–143

[119] X.-D. Zhang, D. Wu, X. Shen, J. Chen, Y.-M. Sun, P.-X. Liu and X.-J. Liang, *Biomaterials*, 2012, **33**, 6408–6419

[120] P. Liu, Z. Huang, Z. Chen, R. Xu, H. Wu, F. Zang, C. Wang and N. Gu, *Nanoscale*, 2013, **5**, 11829–1183

[121] W. N. Rahman, N. Bishara, T. Ackerly, C. F. He, P. Jackson, C. Wong, R. Davidson and M. Geso, *Nanomedicine*, 2009, **5**, 136–142

[122] Z. Bao, M. He, H. Quan, D. Jiang, Y. Zheng, W. Qin, Y. Zhou, F. Ren, M. Guo and C. Jiang, *RSC Adv.*, 2016, **6**, 35124–35134

[123] Q. Li, Y. Tanaka, Y. Saitoh, H. Tanaka and N. Miwa, *Life Sci.*, 2015, **127**, 106–114

[124] J. Gao, G. Liang, B. Zhang, Y. Kuang, X. Zhang and B. Xu, *J. Am. Chem. Soc.*, 2007, **129**, 1428–1433

[125] P. V. Asharani, N. Xinyi, M. P. Hande and S. Valiyaveettil, *Nanomedicine*, 2010, **5**, 51–64

[126] M. Kutwin, E. Sawosz, S. Jaworski, M. Hinzmann, M. Wierzbicki, A. Hotowy, M. Grodzik, A. Winnicka and A. Chwalibog, *Arch. Med. Sci.*, 2016

[127] H. Gehrke, J. Pelka, C. Hartinger, H. Blank, F. Bleimund, R. Schneider, D. Gerthsen, S. Bräse, M. Crone, M. Türk and D. Marko, *Arch. Toxicol.*, 2011, **85**, 799–812

[128] J. Pelka, H. Gehrke, M. Esselen, M. Türk, M. Crone, S. Bräse, T. Muller, H. Blank, W. Send, V. Zibat, P. Brenner, R. Schneider, D. Gerthsen and D. Marko, *Chem. Res. Toxicol.*, 2009, **22**, 649–659

[129] C. Xu, Z. Yuan, N. Kohler, J. Kim, M. A. Chung and S. Sun, *J. Am. Chem. Soc.*, 2009, **131**, 15346–15351

[130] Y. Tian, W. Zi, X. Li, L. Yanji, K. Bian, W. Cao, Y. He, H. Liu, K. Niu and D. Gao, *New J. Chem.*, 2017, **41**, 2941–2948

[131] P. J. Shiny, A. Mukherjee and N. Chandrasekaran, *RSC Adv.*, 2016, **6**, 27775–27787

[132] A. A. Alshatwi, J. Athinarayanan and P. Vaiyapuri Subbarayan, *J. Mater. Sci.: Mater. Med.*, 2015, **26**, 5330

[133] T. López, M. Alvarez, R. D. González, M. J. Uddin, J. Bustos, S. Arroyo and A. Sánchez, *Adsorption*, 2011, **17**, 573–581

[134] T. Lopez, F. Figueras, J. Manjarrez, J. Bustos, M. Alvarez, J. Silvestre-Albero, F. Rodriguez-Reinoso, A. Martinez-Ferre and E. Martinez, *Eur. J. Med. Chem.*, 2011, **45**, 1982–1990

[135] H. Sun, X. Chen, D. Chen, M. Dong, X. Fu, Q. Li, X. Liu, Q. Wu, T. Qiu, T. Wan and S. Li, *Int. J. Nanomed.*, 2012, **7**, 3295–3307

[136] M. Kutwin, E. Sawosz, S. Jaworski, N. Kurantowicz, B. Strojny and A. Chwalibog, *Nanoscale Res. Lett.*, 2014, **9**, 1–6

[137] C. T. Chien, J. Y. Yan, W. C. Chiu, T. H. Wu, C. Y. Liu and S. Y. Lin, *Adv. Mater.*, 2013, **25**, 5067–5073

[138] V. De Matteis, M. A. Malvindi, A. Galeone, V. Brunetti, E. De Luca, S. Kote, P. Kshirsagar, S. Sabella, G. Bardi and P. P. Pompa, *Nanomedicine*, 2014, **11**, 731–739

[139] Y.-P. Jia, B.-Y. Ma, X.-W. Wei, Z.-Y. Qian *Chin Chem Lett*, 28 (2017), pp. 691-702

[140] H. Y. Jia, Y. Liu, X. J. Zhang, L. Han, L. B. Du, Q. Tian and Y. C. Xut, *J. Am. Chem. Soc.*, 2009, **131**, 40–41

[141] M. Manikandan, N. Hasan and H.-F. Wu, *Biomaterials*, 2013, **34**, 5833–5842

[142] Y. Yamagishi, A. Watari, Y. Hayata, X. Li, M. Kondoh, Y. Yoshioka, Y. Tsutsumi and K. Yagi, *Nanoscale Res. Lett.*, 2013, **8**, 395

[143] H. Buchtelova, S. Dostalova, P. Michalek, S. Krizkova, V. Strmiska, P. Kopel, D. Hynek, L. Richtera, A. Ridoskova, P. Adam, J. Kynicky, M. Brtnicky, Z. Heger and V. Adam, *Food Chem. Toxicol.*, 2017, **105**, 337–346

[144] N. C. Bigall, T. Härtling, M. Klose, P. Simon, L. M. Eng and A. Eychmüller, *Nano Lett.*, 2008, **8**, 4588–4592

[145] E. Gharibshahi and E. Saion, *Int. J. Mol. Sci.*, 2012, **13**, 14723–14741

[146] N. C. Bigall, T. Härtling, M. Klose, P. Simon, L. M. Eng and A. Eychmüller, *Nano Lett.*, 2008, **8**, 4588–4592

[147] E. Gharibshahi and E. Saion, *Int. J. Mol. Sci.*, 2012, **13**, 14723–14741

[148] Plan Sangnier, A. et al. Raspberry-like multicore gold nanoparticles with plasmonic resonance spanning in the near infrared for efficient photothermal conversion. Submitted to *Chemical Communications*

[149] Sangnier, A.P., Van De Walle, A., Aufaure, R., Fradet, M., Motte, L., Guénin, E., Lalatonne, Y., Wilhelm, C. *Adv. Biosyst*. 2020, 4, e1900284

[150] Espinosa, A. et al. *Adv. Healthc. Mater*. 5, 1040–1048 (2016).

[151] Iben Ayad, A., Belda Marín, C., Colaco, E., Lefevre, C., Méthivier, C., Ould Driss, A., Landoulsi, J., Guénin, E. *Green Chem.* **2019**, *21*, 6646–6657.

[152] Taniguchi, K., Shinoda, K., Cuya Huaman, J.L., et al. *SN Appl. Sci*. **1**, 124 (2019).

[153] Iversen, T.-G., Skotland, T. & Sandvig, K. *Nano Today* 6, 176–185 (2011).

[154] Pearson, R. M., Hsu, H., Bugno, J. & Hong, S. *MRS Bull*. 39, 227–237 (2014).

[155] Kirschvink, J. L., Kobayashi-Kirschvink, A. & Woodford, B. J. Magnetite biomineralization in the human brain. *Proc. Natl. Acad. Sci.* **89**(16), 7683–7687 (1992).

[156] Hammond, J., Maher, B.A., Ahmed, I.A.M. *et al.* Variation in the concentration and regional distribution of magnetic nanoparticles in human brains, with and without Alzheimer's disease, from the UK. *Sci Rep* **11,** 9363 (2021). https://doi.org/10.1038/s41598-021-88725-3

[157] Van de Walle, A., Perez, J. E., Abou-Hassan, A., Hémadi, M., Luciani, N., & Wilhelm, C. (2020). Magnetic nanoparticles in regenerative medicine: what of their fate and impact in stem cells? *Materials Today Nano*, *11*, 100084.

[158] Dirk Schüler, Genetics and cell biology of magnetosome formation in magnetotactic bacteria, *FEMS Microbiology Reviews*, Volume 32, Issue 4, July 2008, Pages 654–672

[159] Elfick, A., Rischitor, G., Mouras, R., Azfer, A., Lungaro, L., Uhlarz, M., ... & Salter, D. M. (2017). Biosynthesis of magnetic nanoparticles by human mesenchymal stem cells following transfection with the magnetotactic bacterial gene mms6. *Scientific reports*, *7*(1), 1-8.

[160] M. A. Zoroddu, et al., The essential metals for humans: a brief overview. Journal of Inorganic Biochemistry 195, 120–129 (2019).

[161] J. Liu, et al., Metalloproteins Containing Cytochrome, Iron–Sulfur, or Copper Redox Centers. Chem. Rev. 114, 4366–4469 (2014).

[162] V. F. Cardoso, et al., Advances in Magnetic Nanoparticles for Biomedical Applications. Advanced Healthcare Materials 7, 1700845 (2018).

[163] M. I. Anik, et al., Recent progress of magnetic nanoparticles in biomedical applications: A review. Nano Select 2, 1146–1186 (2021).

[164] S. Cabana, A. Curcio, A. Michel, C. Wilhelm, A. Abou-Hassan, Iron Oxide Mediated Photothermal Therapy in the Second Biological Window: A Comparative Study between Magnetite/Maghemite Nanospheres and Nanoflowers. Nanomaterials 10, 1548 (2020).

[165] A. Pekarsky, O. Spadiut, Intrinsically Magnetic Cells: A Review on Their Natural Occurrence and Synthetic Generation. Frontiers in Bioengineering and Biotechnology 8 (2020).

[166] A. Peigneux, et al., Tuning properties of biomimetic magnetic nanoparticles by combining magnetosome associated proteins. Sci Rep 9, 8804 (2019).

[167] B. Ravel and M. Newville, ATHENA, ARTEMIS, HEPHAESTUS: data analysis for X-ray absorption spectroscopy using IFEFFIT, J. Synchrotron Radiat., 2005, 12, 537

[168] K. Gkouvatsos, G. Papanikolaou, K. Pantopoulos, Regulation of iron transport and the role of transferrin. Biochim Biophys Acta 1820, 188–202 (2012).

[169] F. F. A. Kerans, L. Lungaro, A. Azfer, D. M. Salter, The Potential of Intrinsically Magnetic Mesenchymal Stem Cells for Tissue Engineering. Int J Mol Sci 19, 3159 (2018).

[170] N. Jian, M. Dowle, R. D. Horniblow, C. Tselepis, R. E. Palmer, Morphology of the ferritin iron core by aberration corrected scanning transmission electron microscopy. Nanotechnology 27 (2016).

[171] J. Shaw, *et al.*, Magnetic particle-mediated magnetoreception. *J R Soc Interface* **12** (2015).

[172] H. Sant'Ovaia, G. Marques, A. Santos, C. Gomes, A. Rocha, Magnetic susceptibility and isothermal remanent magnetization in human tissues: a study case. *Biometals* **28**, 951–958 (2015).

[173] F. Brem, et al., Magnetic iron compounds in the human brain: a comparison of tumour and hippocampal tissue. J R Soc Interface 3, 833–841 (2006).

[174] C. X. Wang, et al., Transduction of the Geomagnetic Field as Evidenced from alpha-Band Activity in the Human Brain. eNeuro 6, ENEURO.0483-18.2019 (2019).

[175] A. M. Bell, J. T. Robinson, The rotating magnetocaloric effect as a potential mechanism for natural magnetic senses. PLoS One 14, e0222401 (2019).

[176] D. Galante, E. Cavallo, A. Perico, C. D'Arrigo, Effect of ferric citrate on amyloid-beta peptides behavior. Biopolymers 109, e23224 (2018).

[177] C. Caiazza, et al., Effects of Long-Term Citrate Treatment in the PC3 Prostate Cancer Cell Line. Int J Mol Sci 20, E2613 (2019).

[178] T.-A. Wang, S.-L. Xian, X.-Y. Guo, X.-D. Zhang, Y.-F. Lu, Combined 18F-FDG PET/CT imaging and a gastric orthotopic xenograft model in nude mice are used to evaluate the efficacy of glycolysis-targeted therapy. Oncol Rep 39, 271–279 (2018).

[179] A. Espinosa, et al., On the discrimination between magnetite and maghemite by XANES measurements in fluorescence mode. Meas. Sci. Technol. 23, 015602 (2011)

[180] C. Piquer, et al., Fe K-Edge X-ray Absorption Spectroscopy Study of Nanosized Nominal Magnetite. J. Phys. Chem. C 118, 1332–1346 (2014).

[181] Niederberger, M. Nonaqueous sol–gel routes to metal oxide nanoparticles. *Accounts of chemical research*, *40*(9), 793-800 (2007).

Annexe A

Using Magnetometry to Monitor Cellular Incorporation and Subsequent Biodegradation of Chemically Synthetized Iron Oxide Nanoparticles. A Van de Walle, A Fromain, C Wilhelm, Y Lalatonne. ***Jove*** (**2021**)

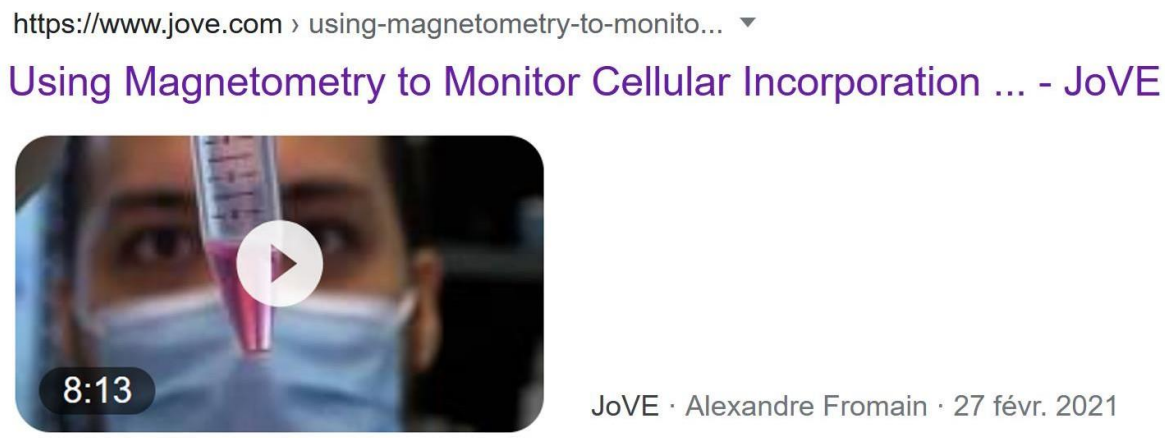

jove

Using Magnetometry to Monitor Cellular Incorporation and Subsequent Biodegradation of Chemically Synthetized Iron Oxide Nanoparticles

Aurore Van de Walle[1], **Anouchka Plan Sangnier**[1,2], **Alexandre Fromain**[1], **Claire Wilhelm**[1], **Yoann Lalatonne**[2,3]

[1] Laboratoire Matière et Systèmes, Complexes MSC, UMR 7057, CNRS & University Paris Diderot [2] Université Sorbonne Paris Nord, Laboratory for Vascular Translational Science, LVTS, INSERM, UMR 1148 [3] Services de Biochimie et Médecine Nucléaire, Hôpital Avicenne Assistance Publique-Hôpitaux de Paris

Corresponding Authors

Aurore Van de Walle
avandewallep7@gmail.com

Claire Wilhelm
claire.wilhelm@univ-paris-diderot.fr

Yoann Lalatonne
yoann.lalatonne@aphp.fr

Citation

Van de Walle, A., Plan Sangnier, A., Fromain, A., Wilhelm, C., Lalatonne, Y. Using Magnetometry to Monitor Cellular Incorporation and Subsequent Biodegradation of Chemically Synthetized Iron Oxide Nanoparticles. *J. Vis. Exp.* (168), e61106, doi:10.3791/61106 (2021).

Date Published

February 27, 2021

DOI

10.3791/61106

URL

jove.com/video/61106

Abstract

Magnetic nanoparticles, made of iron oxide, present a peculiar interest for a wide range of biomedical applications for which they are often internalized in cells and then left within. One challenge is to assess their fate in the intracellular environment with reliable and precise methodologies. Herein, we introduce the use of the vibrating sample magnetometer (VSM) to precisely quantify the integrity of magnetic nanoparticles within cells by measuring their magnetic moment. Stem cells are first labeled with two types of magnetic nanoparticles; the nanoparticles have the same core produced via a fast and efficient microwave-based nonaqueous sol gel synthesis and differ in their coating: the commonly used citric acid molecule is compared to polyacrylic acid. The formation of 3D cell-spheroids is then achieved via centrifugation and the magnetic moment of these spheroids is measured at different times with the VSM. The obtained moment is a direct fingerprint of the nanoparticles' integrity, with decreasing values indicative of a nanoparticle degradation. For both nanoparticles, the magnetic moment decreases over culture time revealing their biodegradation. A protective effect of the polyacrylic acid coating is also shown, when compared to citric acid.

Introduction

There is increased interest in the magnetic features of iron oxide nanoparticles for a wide range of biomedical applications. Their response to magnetic resonance makes them reliable contrast agents for magnetic resonance imaging (MRI), an advantage in regenerative medicine where cells labeled with magnetic nanoparticles can be tracked in vivo

following implantation[1]. Using magnetic fields, cells can also be guided at a distance; this way, cellular spheroids[2,3], rings[4], or sheets[5] can be engineered magnetically and also remotely stimulated[6], an asset in the development of scaffold-free tissues. The range of possibilities for these nanoparticles also includes drug delivery systems[7,8] and magnetic and photoinduced hyperthermal treatment to kill cancerous cells[9,10,11]. For all these applications, the nanoparticles are integrated in the biological environment either by intravenous injection or via direct internalization in cells and are then left within, which brings into question their intracellular fate.

In vivo analyses conveyed a general understanding of the nanoparticles' fate in the organism: upon injection in the blood stream, they are first captured mostly by the macrophages of the liver (Kupffer cells), spleen and bone marrow, are progressively degraded, and join the iron pool of the organism[12,13,14,15,16,17,18,19]. Qualitative observations are only possible due to the circulation of the nanoparticles throughout the organism. Typically, transmission electronic microscopy (TEM) can be used to directly observe the nanoparticles and the presence of iron in the organs can be determined via dosage. More recently, their fate has been assessed directly on a pool of cells, meaning in close circuit with no iron escape, allowing a quantitative measurement of their biotransformations at the cell-level[20,21,22]. Such measurements are possible via the analysis of the magnetic properties of the nanoparticles that are tightly linked to their structural integrity. Vibrating sample magnetometry (VSM) is a technique where the sample is vibrated periodically so that the coil-measurement of the flux induced provides the magnetic moment of the sample at the applied magnetic field. Such synchronous detection allows for a rapid measurement, which is an asset for determining the magnetic moments of a large number of samples[20,21,22,23]. The macroscopic magnetic signature retrieved by VSM then gives a quantitative overview of the entire biological sample directly correlated to the nanoparticles' size and structure. In particular, it provides the magnetic moment at saturation (expressed in emu) of the samples, which is a direct quantification of the number of magnetic nanoparticles present in the sample, respectively to their specific magnetic properties.

It has been shown that the intracellular processing of magnetic nanoparticles is tightly linked to their structural features[20]. These features can be controlled via optimal synthesis protocols. Each protocol presents advantages and limitations. Iron oxide nanoparticles are commonly synthesized in aqueous solutions via coprecipitation of iron ions[24]. To overcome the limitations of nanoparticles size polydispersity, other synthesis methods such as polyol-mediated sol-gel methods have been developed[25]. Nonaqueous approaches by thermal decomposition leads to the production of very well-calibrated iron oxide nanoparticles[26]. However, the use of massive amounts of surfactants like oleylamine or oleic acid complicates their functionalization and water transfer for biomedical applications. For this reason, we synthesize such magnetic nanoparticles through a nonaqueous sol gel route leading to high crystallinity, purity and reproducibility[27]. This protocol produces well-controlled size nanoparticles that can be tuned through temperature variation[28]. Nevertheless, the microwave-assisted non-aqueous sol-gel route has an upper size limit of the obtained nanoparticles of around 12 nm. This procedure would not be adapted for applications using ferromagnetic particles at room temperature. In addition to the core synthesis, another main feature to be considered is the coating. Lying at the surface of the nanoparticle, the coating acts as an anchoring molecule, helping the targeted

internalization of the nanoparticles, or it can protect the nanoparticle from degradation. Since benzyl alcohol acts as an oxygen source and a ligand at the same time, bare nanoparticles are produced without the need for additional surfactants or ligands. The nanoparticles are then easily surface functionalized after synthesis without a surfactant exchange process.

Herein, two types of nanoparticles are assessed that possess the same core and differ in the coating. The core is synthesized using a fast and highly efficient microwave based technique. The two coatings compared consist of citric acid, one of the most used as coating agent in biomedical applications[29, 30], and polyacrylic acid (PAA), a polymeric coating with a high number of chelating functions. VSM magnetometry measurements are then used first to quantify the nanoparticle uptake by the cells, and then as a direct assessment of the nanoparticle structural integrity upon internalization in stem cells. Results demonstrate that the incubation concentration impacts nanoparticle uptake and that the coating influences their degradation, with the large number of anchoring molecules of PAA protecting the core from degradation.

Protocol

1. Synthesis of magnetic nanoparticles

1. Core synthesis – microwave-assisted
    1. Dissolve 400 mg of iron(III) acetylacetonate (>99.9%) in 10 mL of benzyl alcohol (BA, 99.8%) within a 30 mL monowave glass vial.
    2. Increase the temperature of the suspension from 25 to 250 °C in 20 min (at a rate of 11.25 °C/min) and maintain it at 250 °C for 30 min using a microwave reactor.
    3. Transfer the resulting nanoparticles suspended in benzyl alcohol to a glass vial and separate the nanoparticles using a neodymium magnet for 30 min.
    4. Wash the precipitate in the previous 100 mL glass vial with 10 mL of dichloromethane, 1 M sodium hydroxide, ethanol, pH 7 water (three times) using a neodymium magnet for 5 min each step to pelletize nanoparticles and remove the supernatant.
    5. Adjust the nanoparticle suspension in water to pH 2 using 1 M hydrochloric acid, and then centrifuge in 100 kDa ultracentrifugal filters at 2,200 x *g* for 10 min.
    6. Remove the filtrate, add 12 mL of 10^{-2} M hydrochloric acid to the nanoparticles solution and centrifuge in 100 kDa ultracentrifugal filters at 2,200 x *g* for 10 min (three times). Then dilute the nanoparticles solution within 10 mL of 10^{-2} M hydrochloric acid before coating.
2. Coating
    1. Dilute 175 mg of citric acid and polyacrylic acid in water at pH 2 in a 100 mL glass vial and adjusted the pH to 2 with a 1 M hydrochloric acid solution.
    2. Add the 10 mL nanoparticles aqueous dispersion to the coating molecule solution, corresponding to a mass ratio of 5 between the coating molecule and the nanoparticles. Agitate for 2 h under magnetic stirring at room temperature.
    3. After the reaction, adjust the pH to 7 with 1 M sodium hydroxide.

4. Centrifuge the nanoparticle solution 3 times with deionized (DI) water in 100 kDa ultracentrifugal filters at 2,200 x *g* for 10 min; remove the filtrate and dilute the nanoparticles solution in 12 mL of DI water.

2. Culture and magnetic labeling of stem cells

1. Culture human mesenchymal stem cells (MSC) in complete Mesenchymal Stem Cell Growth Medium (MSCGM) at 37 °C and 5% CO_2. When the cells are at 90% confluence, add 10 mL of trypsin-EDTA pre-warmed at 37°C per 150 cm² flask and leave for 2-3 minutes to detach the cells.
    1. To know when the cells are detached, observe them with a bright-field microscope. Resuspend the detached cells in MSCGM and divide them in four 150 cm² flasks. Amplify the cells this way until passage 4 to 5.
2. Prepare the solution of magnetic nanoparticles for cell labeling: disperse the chosen concentration of iron oxide nanoparticles in serum free Roswell Park Memorial Institute medium (RMPI-1640) without glutamine. RPMI is used for nanoparticle incubation (and the related rinsing steps) as it has a lower ionic strength than DMEM and better prevents nanoparticle aggregation events.
3. When the cells are at passage 4 or 5 and 90% confluent, remove the MSCGM medium, rinse the cells with serum free RPMI (without glutamine) and add 10 mL of iron oxide nanoparticles solution per 150 cm² culture flask, which is the minimum volume required to cover all the cells.
4. Incubate at 37 °C and 5% CO_2 for 30 min and then discard the nanoparticle solution. Wash once with serum free RPMI-1640 (no glutamine) and incubate with Dulbecco's Modified Eagle Medium (DMEM) supplemented with 10% FBS and 1% penicillin-streptomycin (25 mL per 150 cm² flask) overnight at 37 °C and 5% CO_2 to allow a complete internalization of the nanoparticles.

3. Formation of stem cell-spheroids

1. Freshly prepare cell-spheroid culture medium composed of DMEM high glucose with L-glutamine supplemented with 50 µM L-ascorbic acid 2-phosphate, 0.1 µM dexamethasone, 1 mM sodium pyruvate, 0.35 mM L-proline, and 1% universal culture supplement containing Insulin, human Transferrin and Selenous acid (ITS-Premix).
2. Detach the magnetic MSCs by adding 10 mL of 0.05% trypsin-EDTA pre-warmed at 37 °C per 150 cm² flask for 2-3 minutes. When the cells are detached, immediately inactivate the trypsin by adding 1/3 of the volume of DMEM supplemented with 10% FBS and 1% penicillin-streptomycin pre-warmed at 37 °C.
3. Centrifuge the dissociated cells at 260 x *g* for 5 min, aspirate the media and re-suspend the cells in a small volume (less than 1 mL per 150 cm² flask) of cell-spheroid culture medium such as having 200,000 cells in about 50 µL of medium. Count the cell number using a hemocytometer and adjust the volume if needed.
4. Add 1 mL of freshly prepared cell-spheroid culture medium in a 15 mL sterile conical centrifuge tube and add the volume of resuspended solution corresponding to 200,000 cells.
5. Centrifuge these magnetically labeled cells at 180 x *g* for 3 min such as forming a cell pellet at the bottom of the

tube and keep the supernatant, which is the cell culture medium.

6. Slightly open the tubes to allow air exchange and incubate at 37 °C with 5% CO_2 for up to 21 days, culture time along which the cells form a cohesive 3D structure that results in a fully formed spheroid. Change the medium twice a week.

7. On given days, wash the spheroids twice with cacodylate buffer made of 0.2 M cacodylate diluted in demineralized water and fix them using 2% glutaraldehyde in 0.1 M cacodylate buffer diluted in distilled water for 30 min at room temperature. Store the fixed spheroids in PBS until used for VSM measurement or TEM imaging. This fixation step stops all biological processes and allows long-term conservation.

4. Quantification of magnetic nanoparticles in solution and in cellulo using a vibrating sample magnetometer (VSM)

1. Place either a given volume of magnetic nanoparticle solution (maximum 10 µL) or a single cell-spheroid into the sample holder specifically designed to fit in the VSM.

2. Insert the sample in the VSM and scan for sample offset. Place the sample at the position corresponding to the magnetization maximum.

3. Perform the first measurement at a low magnetic field (between -1500 Oe and +1500 Oe) with a 20 Oe/s rate.

4. Perform a second measurement at a high magnetic field (between -30 000 Oe and +30 000 Oe) with a 200 Oe/s rate.

5. Transmission Electron Microscopy (TEM) analysis

1. For the nanoparticle solutions, deposit 10 µL of the aqueous solution onto a carbon-coated copper grid and let it dry at room temperature.

2. For the nanoparticles internalized in cells, contrast the fixed cell-spheroids with Oolong Tea Extract (OTE) at 0.5% diluted in 0.1 M cacodylate buffer, post fix with 1% osmium tetroxide containing 1.5% potassium cyanoferrate and then dehydrate in graded ethanol baths, included in Epon. Slice ultrasections of 70 nm and deposit them onto cooper grids.

3. Take images using an electron microscope at 80 kV with a magnification from 1k for the observation of entire cells to 40k for the observation of endosomal compartments.

Representative Results

Using the microwave-assisted synthesis, magnetic nanoparticles with a monodisperse 8.8 ± 2.5 nm core size are produced and coated with either citrate or PAA (**Figure 1A**). Stem cells are then incubated with these nanoparticles dispersed in culture medium at a given concentration for 30 minutes, resulting in their endocytosis and confinement within the cellular endosomes (**Figure 1B**). The magnetic stem cells are then suspended in medium, centrifuged, and the cell pellet formed is cultured for up to 21 days (**Figure 1C**). The spheroids obtained are fixed, such as stopping biological processes, and kept in PBS until being measured via VSM.

First, the magnetic moment of the nanoparticle solution is measured using the VSM: 10 µL of the nanoparticle aqueous dispersion containing 7 µg of iron is measured, and the obtained curve is displayed in **Figure 2A**. Due to the presence of water in this solution, and to the

sample holder, a diamagnetic signal is captured in addition to the superparamagnetic signal of the nanoparticles. A diamagnetic constant (M_{dia}) corresponding to the slope of the second part of the curve can be measured, as shown in **Figure 2A**, and this constant can be subtracted such as obtaining the magnetic moment of the nanoparticles only ($M_{sample} = M - M_{dia}$). The saturation magnetization of the nanoparticles (M_S) can then be extracted; it corresponds to 518 µemu for the aqueous dispersion, meaning that the solution is at 74 emu/g of iron (Fe) corresponding to 52 emu/g of nanoparticles (Fe_3O_4).

The magnetic moment of cell spheroids can similarly be obtained. In this case, a cell-spheroid (made of 200,000 cells) is inserted in the sample holder, placed in the VSM, and measured (**Figure 2B**). The magnetic moment values obtained are here much lower than the ones of the initial nanoparticle solution; however, they remain within the detection range. The saturation magnetization of this particular sample is of 69 µemu. Besides, this spheroid contains 1.3 µg of nanoparticles (6.7 pg of nanoparticles per cell), consistent with the saturation value at 52 emu/g_{Fe3O4}. This value can thus be used to determine the amount of nanoparticles in cellular samples. In **Figure 2C**, spheroids corresponding to cells labelled with three concentrations of citrate-coated nanoparticles are measured one day after labelling. Results clearly show that the uptake of the nanoparticles depends on the incubation concentration, with concentrations of 0.125, 0.25 and 0.5 mM leading to uptakes of 0.3, 0.7 and 1.3 µg of iron per spheroid, meaning 1.3, 3,3 and 6.7 pg of iron per cell, respectively.

Attention has been brought on the importance of the surface coating, which directly interacts with the biological environment[20]. Two coatings have here been produced: a citrate coating, commonly used for biomedical applications, and a PAA coating, with a higher number of chelating functions. Stem cells are labeled with these two types of nanoparticles and centrifuged such as forming a cell pellet that then becomes a cohesive cell-spheroid (**Figure 3A**). Magnetism of these cell-spheroids is measured via VSM at day 1 and day 21 (**Figure 3B** and **Figure 3C**). Results demonstrate a decrease in magnetism upon the 21 days of culture, indicating the biodegradation of the nanoparticles, this degradation being more important for the citrate-coated nanoparticles (**Figure 3B**) than the PAA-coated ones (**Figure 3C**). TEM images confirm the degradation of the nanoparticles and show the appearance of smaller (6 nm in size) light grey dots, typical of ferritin loaded with iron. Some nanoparticles remaining intact can also be observed, particularly with the PAA coating.

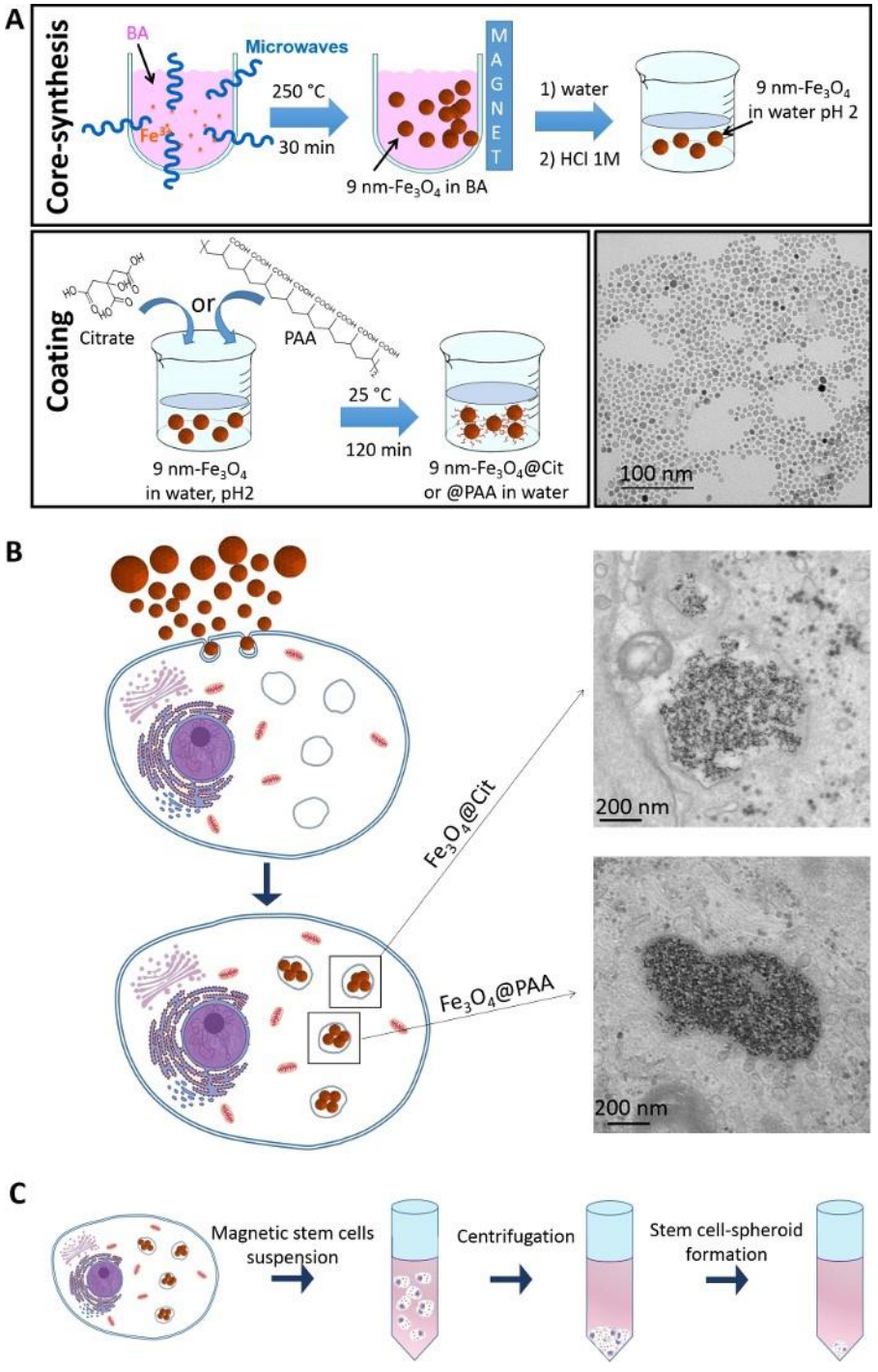

Figure 1: Microwave-assisted synthesis of iron oxide (Fe_3O_4) nanoparticles, their internalization in stem cells and the subsequent culture of the cells as spheroids. (**A**) Schematic of the various steps of the nanoparticle synthesis. First, the core is synthesized via a non-aqueous sol gel procedure. The coating molecule, either Citrate (Cit) or polyacrylic acid (PAA), is then grafted at the surface of the iron oxide core. A representative TEM image shows the synthesized nanoparticles with a citrate coating. (**B**) Schematic of the nanoparticle internalization within stem cell, showing the nanoparticles confined in

the endosomes upon internalization. Representative TEM images also show the citrate and PAA coated nanoparticles inside the cells, confined in the endosomes. (**C**) Schematic of stem cell-spheroids formation. Please click here to view a larger version of this figure.

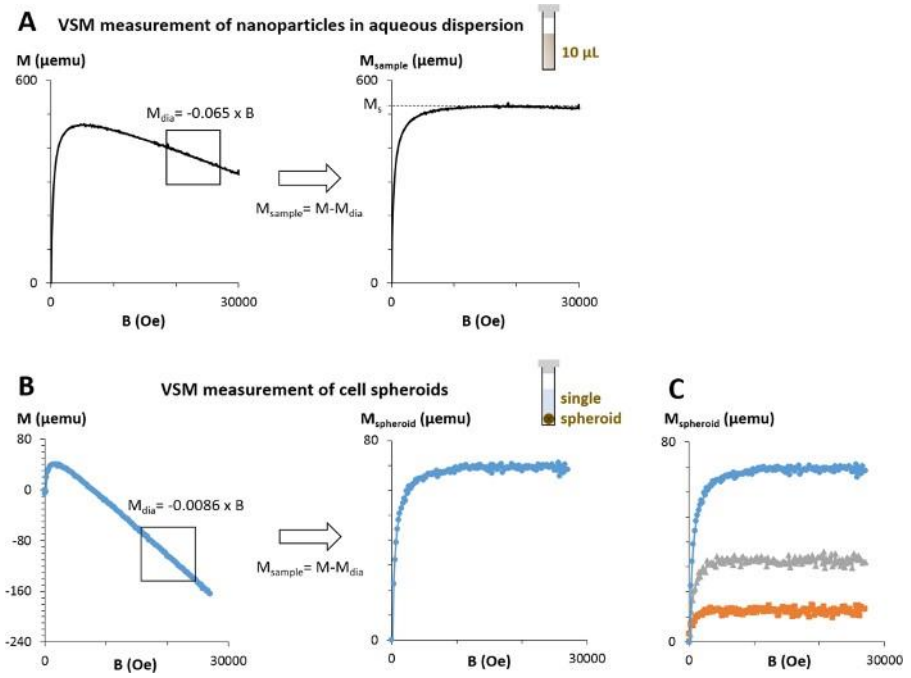

Figure 2: Measurement of the samples magnetic moment via VSM. (**A**) 10 µL of nanoparticles dispersed in an aqueous solution are measured via the VSM. The signal obtained represents the magnetic moment of this nanoparticle solution in function of the magnetic field (B). The diamagnetism coming from the presence of water and the sample holder can then be measured as it corresponds to the slope of the second part of the curve and subtracted such as obtaining the magnetic moment of the nanoparticles only. The magnetic moment at saturation (M_S) can then be determined. (**B**) The magnetic moment of cell spheroids can similarly be obtained; In this case a single cell-spheroid is measured at a given time period. (**C**) Curves of spheroids corresponding to cells labeled with citrate-coated nanoparticles at three independent concentrations of 0.125 mM (orange), 0.25 mM (grey) and 0.5 mM (blue). Please click here to view a larger version of this figure.

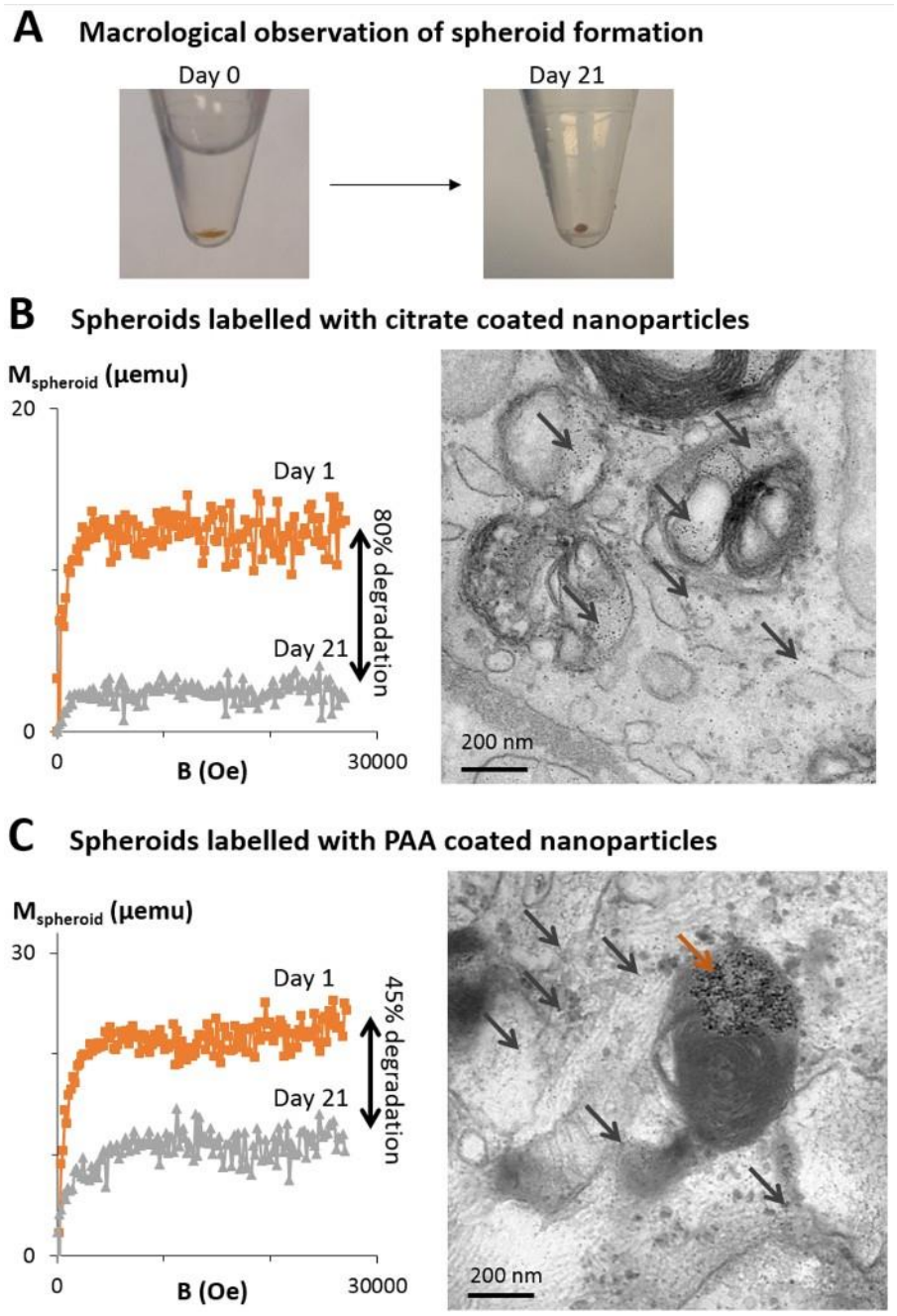

Figure 3: Quantification of magnetic nanoparticle degradation in cellulo via VSM. (**A**) Upon cell labeling with magnetic nanoparticles, a cell pellet is formed by centrifugation (day 0). The cells then form a cohesive structure resulting in an easy to handle cell-spheroid that can be kept in culture without cell loss for extended time periods (months). (**B, C**) Herein, two types of magnetic nanoparticles, coated with citrate (**B**) or PAA (**C**), are internalized in stem cells and the cells are cultured as spheroids for up to 21 days. Magnetism of spheroids cultured for 1 day (orange curves) and 21 days (grey curves) are measured with the VSM, with a decrease in magnetism indicating a degradation of the nanoparticles. Representative TEM

images taken at day 21 show light grey dots about 6 nm is size within the endosomes and the cytoplasm of the cells, typical size and shape of ferritin, the iron storage protein (black arrows). Some intact nanoparticles can also be observed, mostly for the PAA-coated nanoparticles (brown arrow). Please click here to view a larger version of this figure.

Discussion

Using a fast and efficient microwave-based synthesis, magnetic nanoparticles can easily be synthesized, with controlled size, and further coated with given molecules. A critical step is to stock the iron salt and the benzyl alcohol under vacuum to keep a small dispersion in size. The benzyl alcohol acts as both as solvent and ligand at the same time allowing to directly obtain calibrated bare iron oxide without the need of additional ligands. After nanoparticles transfer in water the bare magnetic nanoparticles can be easily coated with a large variety of ligands. This coating confers inter-nanoparticle and nanoparticle-cell interacting properties that can influence their cellular internalization, a parameter that needs to be tightly controlled as a minimum internalization is required for biomedical applications while a too high internalization could be damaging to the cells and potentially originate cytotoxic events[31]. Magnetometry is a powerful tool to assess this internalization as well as the fate of magnetic nanoparticles in cellulo. Upon the incorporation of magnetic nanoparticles into stem cells, spheroids can be formed via a simple centrifugation followed by culture in a medium that stops the proliferation of the cells and drives extracellular matrix production. The cells become highly cohesive and start creating a tissue. The spheroids are then very easy to handle and can be cultured for extended time periods (months) that allows for long-term tracking of magnetic nanoparticles' fate in a biological environment. By stopping cell division, there is no dilution of the nanoparticles from mother to daughter cell; moreover, it has been verified that, with this cell-spheroid model, there is no iron escape over a month of culture[21,22,23]. As a consequence, a decrease in magnetism values can only correspond to a degradation of the nanoparticles and not to iron being exported out of the cells.

Magnetism of the cell spheroids is here measured via VSM that provides a fast and precise quantification. Other methods have also been explored to measure cellular magnetism, such as using a Superconducting Interface Device (SQUID), a machine typically more precise than the VSM with a sensitivity around 10^{-7} emu compared to 10^{-6} emu for the VSM, but operational cost is higher[32]. The sensitivity of the VSM allowing measurements of magnetic iron dose inferior to 2 pg/cell in the experimental setup is herein sufficiently precise as iron doses inferior to 2 pg/cell would be too low for the aimed applications, such as cell attraction toward a magnetic for cell guidance and tissue engineering purposes. Both VSM and SQUID magnetometry, in addition to allowing a quantification of cell magnetism, can give additional details on the nanoparticles' features. By analysis of the signal obtained, the size of the nanoparticles can be deducted[22,23] and also general notion of their magnetic features can be obtained, hysteresis and coercivity of nanomaterials can for example be revealed. Alternative magnetometry approaches also exist, such as magnetophoresis that consists in measuring the velocity of individual cells when attracted toward a magnet and the magnetism of single cells is extrapolated[33,34]. The magnetism at the single cell level can this way be obtained; however, no additional nanoparticle features can be determined. Additionally, a small magnetic sensor that provides a signal proportional to the sample magnetism has recently been used with a similar cell spheroid model.

This magnetic sensor allowed the tracking of magnetic nanoparticles' biodegradation in real-time, continuously, over 7 days[35]. However, the signal of this magnetic sensor cannot be directly translated into a magnetic moment as it depends on the size of the nanoparticles. For this reason, a calibration curve needs to be performed for each nanoparticle design, curve that can be realized using the VSM.

Measurements performed herein with the VSM demonstrate a progressive degradation of the magnetic nanoparticles in the cellular environment, indicated by a decrease in magnetism. They also evidence that a same core coated with different molecules is degraded at varying rates depending on the coating. When comparing a PAA and a citrate coating, PAA leads to higher core protection to degradation, most probably due to its strong anchoring to the magnetic core[20]. The fate of magnetic nanoparticles in the intracellular environment is assessed on cell spheroids; however, the method is not limited to it. Indeed, it can be extrapolated to cell suspensions, which has already been used to assess the effect of stem cell differentiation on the fate of the nanoparticles[22]. It revealed that, depending on the differentiation pathway, the magnetic nanoparticles are processed differently by the cells, with, in some cases, the neo-crystallization of iron upon its dissolution. VSM magnetometry is thus a useful tool to further explore the influence of both nanoparticle and cell features on the intracellular processing of iron oxide nano-objects.

Disclosures

The authors have nothing to disclose.

Acknowledgments

This work was supported by the European Union (ERC-2014-CoG project MaTissE #648779). The authors would like to acknowledge the CNanoMat physico-chemical characterizations platform of University Paris 13.

References

1. Azevedo-Pereira, R.L. et al. Superparamagnetic iron oxide nanoparticles as a tool to track mouse neural stem cells in vivo. *Molecular Biology Reports.* **46** (1), 191-198 (2019).
2. Fayol, D., Frasca, G., Le Visage, C., Gazeau, F., Luciani, N., Wilhelm, C. Use of magnetic forces to promote stem cell aggregation during differentiation, and cartilage tissue modeling. *Advanced Materials (Deerfield Beach, Fla.).* **25** (18), 2611-2616 (2013).
3. Kim, J.A. et al. High-throughput generation of spheroids using magnetic nanoparticles for three-dimensional cell culture. *Biomaterials.* **34** (34), 8555-8563 (2013).
4. Yamamoto, Y. et al. Preparation of artificial skeletal muscle tissues by a magnetic force-based tissue engineering technique. *Journal of Bioscience and Bioengineering.* **108** (6), 538-543 (2009).
5. Gonçalves, A.I., Rodrigues, M.T., Gomes, M.E. Tissue-engineered magnetic cell sheet patches for advanced strategies in tendon regeneration. *Acta Biomaterialia.* **63**, 110-122 (2017).
6. Du, V. et al. A 3D magnetic tissue stretcher for remote mechanical control of embryonic stem cell differentiation. *Nature Communications.* **8** (1), 400 (2017).
7. Amiri, M., Salavati-Niasari, M., Pardakhty, A., Ahmadi, M., Akbari, A. Caffeine: A novel green precursor for synthesis of magnetic CoFe2O4 nanoparticles and pH-sensitive magnetic alginate beads for drug delivery. *Materials Science and Engineering: C.* **76**, 1085-1093 (2017).

8. Vangijzegem, T., Stanicki, D., Laurent, S. Magnetic iron oxide nanoparticles for drug delivery: applications and characteristics. *Expert Opinion on Drug Delivery.* **16** (1), 69-78 (2019).

9. Cazares-Cortes, E. et al. Recent insights in magnetic hyperthermia: From the “hot-spot” effect for local delivery to combined magneto-photo-thermia using magneto-plasmonic hybrids. *Advanced Drug Delivery Reviews.* **138**, 233-246 (2019).

10. Espinosa, A. et al. Magnetic (Hyper)Thermia or Photothermia? Progressive Comparison of Iron Oxide and Gold Nanoparticles Heating in Water, in Cells, and in vivo. *Advanced Functional Materials.* **28** (37), 1803660 (2018).

11. Plan Sangnier, A. et al. Targeted thermal therapy with genetically engineered magnetite magnetosomes@RGD: Photothermia is far more efficient than magnetic hyperthermia. *Journal of Controlled Release.* **279**, 271-281 (2018).

12. Pham, B.T.T. et al. Biodistribution and Clearance of Stable Superparamagnetic Maghemite Iron Oxide Nanoparticles in Mice Following Intraperitoneal Administration. *International Journal of Molecular Sciences.* **19** (1) (2018).

13. Kolosnjaj-Tabi, J. et al. Biotransformations of magnetic nanoparticles in the body. *Nano Today.* **11** (3), 280-284 (2016).

14. Bargheer, D. et al. The distribution and degradation of radiolabeled superparamagnetic iron oxide nanoparticles and quantum dots in mice. *Beilstein Journal of Nanotechnology.* **6**, 111-123 (2015).

15. Freund, B. et al. A simple and widely applicable method to 59Fe-radiolabel monodisperse superparamagnetic iron oxide nanoparticles for in vivo quantification studies. *ACS Nano.* **6** (8), 7318-7325 (2012).

16. Singh, S.P., Rahman, M.F., Murty, U.S.N., Mahboob, M., Grover, P. Comparative study of genotoxicity and tissue distribution of nano and micron sized iron oxide in rats after acute oral treatment. *Toxicology and Applied Pharmacology.* **266** (1), 56-66 (2013).

17. Levy, M. et al. Long term in vivo biotransformation of iron oxide nanoparticles. *Biomaterials.* **32** (16), 3988-3999 (2011).

18. Briley-Saebo, K. et al. Hepatic cellular distribution and degradation of iron oxide nanoparticles following single intravenous injection in rats: implications for magnetic resonance imaging. *Cell and Tissue Research.* **316** (3), 315-323 (2004).

19. Gu, L., Fang, R.H., Sailor, M.J., Park, J.H. In vivo Clearance and Toxicity of Monodisperse Iron Oxide Nanocrystals. *ACS Nano.* **6** (6), 4947-4954 (2012).

20. Sangnier, A.P. et al. Impact of magnetic nanoparticle surface coating on their long-term intracellular biodegradation in stem cells. *Nanoscale.* (2019).

21. Mazuel, F. et al. Magneto-Thermal Metrics Can Mirror the Long-Term Intracellular Fate of Magneto-Plasmonic Nanohybrids and Reveal the Remarkable Shielding Effect of Gold. *Advanced Functional Materials.* **27** (9), 1605997 (2017).

22. Van de Walle, A. et al. Biosynthesis of magnetic nanoparticles from nano-degradation products revealed in human stem cells. *Proceedings of the National*

Academy of Sciences of the United States of America. **116** (10), 4044-4053 (2019).

23. Mazuel, F. et al. Massive Intracellular Biodegradation of Iron Oxide Nanoparticles Evidenced Magnetically at Single-Endosome and Tissue Levels. *ACS Nano.* **10** (8), 7627-7638 (2016).
24. Bee, A., Massart, R., Neveu, S. Synthesis of very fine maghemite particles. *Journal of Magnetism and Magnetic Materials.* **149** (1), 6-9 (1995).
25. Feldmann, C., Jungk, H.O. Polyol-Mediated Preparation of Nanoscale Oxide Particles. *Angewandte Chemie International Edition.* **40** (2), 359-362 (2001).
26. Hyeon, T., Lee, S.S., Park, J., Chung, Y., Na, H.B. Synthesis of Highly Crystalline and Monodisperse Maghemite Nanocrystallites without a Size-Selection Process. *Journal of the American Chemical Society.* **123** (51), 12798-12801 (2001).
27. Pinna, N., Grancharov, S., Beato, P., Bonville, P., Antonietti, M., Niederberger, M. Magnetite Nanocrystals: Nonaqueous Synthesis, Characterization, and Solubility. *Chemistry of Materials.* **17** (11), 3044-3049 (2005).
28. Richard, S. et al. USPIO size control through microwave nonaqueous sol-gel method for neoangiogenesis T2 MRI contrast agent. *Nanomedicine.* **11** (21), 2769-27797 (2016).
29. Ngo, A.T., Pileni, M.P. Assemblies of Ferrite Nanocrystals: Partial Orientation of the Easy Magnetic Axes. *The Journal of Physical Chemistry B.* **105** (1), 53-58 (2001).
30. Li, L. et al. Effect of synthesis conditions on the properties of citric-acid coated iron oxide nanoparticles. *Microelectronic Engineering.* **110**, 329-334 (2013).
31. Sun, X. et al. Tracking stem cells and macrophages with gold and iron oxide nanoparticles – The choice of the best suited particles. *Applied Materials Today.* **15**, 267-279 (2019).
32. Buchner, M., Höfler, K., Henne, B., Ney, V., Ney, A. Tutorial: Basic principles, limits of detection, and pitfalls of highly sensitive SQUID magnetometry for nanomagnetism and spintronics. *Journal of Applied Physics.* **124** (16), 161101 (2018).
33. Wilhelm, C., Gazeau, F., Bacri, J.C. Magnetophoresis and ferromagnetic resonance of magnetically labeled cells. *European Biophysics Journal.* **31** (2), 118-125 (2002).
34. Jing, Y. et al. Quantitative intracellular magnetic nanoparticle uptake measured by live cell magnetophoresis. *The FASEB Journal.* **22** (12), 4239-4247 (2008).
35. Van de Walle, A. et al. Real-time in situ magnetic measurement of the intracellular biodegradation of iron oxide nanoparticles in a stem cell-spheroid tissue model. *Nano Research.* (2020).

Annexe B

Real-time in situ magnetic measurement of the intracellular biodegradation of iron oxide nanoparticles in a stem cell-spheroid tissue model.

Van de Walle A, Fromain A, Plan Sangnier A, Curcio A, Lenglet L, Motte L,Lalatonne Y, Wilhelm C. ***Nano Research*** **13**, 467-476 (**2020**)

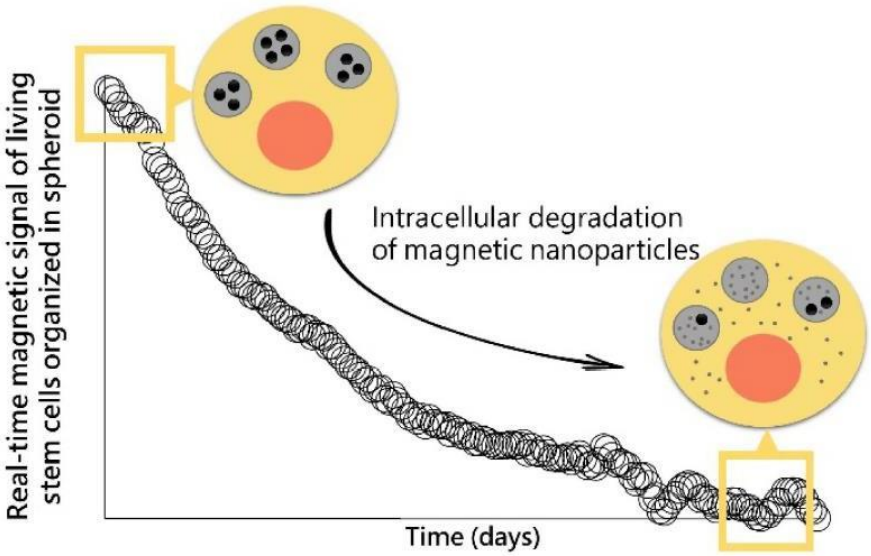

The internalization and progressive degradation of magnetic nanoparticles within stem cells is assessed at the single spheroid level, in real-time, in the biological environment, on alive samples, using a benchtop-size magnetic sensor, without impacting cell functionality.

Nano Research

ISSN 1998-0124 CN 11-5974/O4
https://doi.org/10.1007/s12274-020-2631-1

Research Article

Real-time *in situ* magnetic measurement of the intracellular biodegradation of iron oxide nanoparticles in a stem cell-spheroid tissue model

Aurore Van de Walle[1] (✉), Alexandre Fromain[1], Anouchka Plan Sangnier[1,2], Alberto Curcio[1], Luc Lenglet[3], Laurence Motte[2] (✉), Yoann Lalatonne[2,4] (✉), and Claire Wilhelm[1] (✉)

[1] *Laboratoire Matière et Systèmes, Complexes MSC, UMR 7057, CNRS & University Paris Diderot, 75205, Paris Cedex 13, France*
[2] *Inserm, U1148, Laboratory for Vascular Translational Science, Université Paris 13, Sorbonne Paris Cité, F-93017 Bobigny, France*
[3] *Normafin Sàrl, 8 rue Mathilde Girault, 92300 Levallois-Perret, France*
[4] *Services de Biochimie et Médecine Nucléaire, Hôpital Avicenne Assistance Publique-Hôpitaux de Paris F-93009 Bobigny, France*

Received: 21 November 2019 / **Revised:** 19 December 2019 / **Accepted:** 27 December 2019

ABSTRACT

The use of magnetic nanoparticles in nanomedicine keeps expanding and, for most applications, the nanoparticles are internalized in cells then left within, bringing the need for accurate, fast, and easy to handle methodologies to assess their behavior in the cellular environment. Herein, a benchtop-size magnetic sensor is introduced to provide real-time precise measurement of nanoparticle magnetism within living cells. The values obtained with the sensor, of cells loaded with different doses of magnetic nanoparticles, are first compared to conventional vibrating sample magnetometry (VSM), and a strong correlation remarkably validates the use of the magnetic sensor as magnetometer to determine the nanoparticle cellular uptake. The sensor is then used to monitor the progressive intracellular degradation of the nanoparticles, over days. Importantly, this real-time *in situ* measure is performed on a stem cell-spheroid tissue model and can run continuously on a same spheroid, with cells kept alive within. Besides, such continuous magnetic measurement of cell magnetism at the tissue scale does not impact either tissue formation, viability, or stem cell function, including differentiation and extracellular matrix production.

KEYWORDS

magnetic nanoparticles, magnetometry, real-time in operando measures, biodegradation, stem cells

1 Introduction

Magnetic nanoparticles provide extended feature for a vast range of biomedical applications. They were first developed as magnetic resonance imaging (MRI) contrast agents [1–4], for some already at disposition in the clinic [5]. They have since been developed as cancer treatment agent, for killing diseased cells via magnetic hyperthermal [3, 4, 6–15] or photothermal [9, 16–19] procedures, and as carriers for drug delivery [10, 12, 20–23]. More recently, their use has been implemented in tissue regeneration [24–26], for cell guidance at a distance and the possibility of creating cellular tissues whose fate upon implantation can be monitored by MRI [27]. In this context, the nanoparticles' integration within the body and progressive clearance from it have been extensively studied. Along their circulation in the bloodstream they are first captured mainly by the macrophages of the liver (Kupffer cells), spleen, and bone marrow, where iron content peaks within hours and are then progressively degraded [28–32]. These *in vivo* results provide a general understanding about how nanoparticles behave in the body. Nonetheless, precise quantitative monitoring of their degradation at the heart of cells is still an open challenge. Some *in vitro* studies completed the initial *in vivo* observations by assessing the fate of the nanoparticles upon internalization within cells, on fixed cells, at given time points [33–35]. They confirmed that, upon incorporation within cells, magnetic nanoparticles are progressively degraded over the course of a month. For these studies, the cell samples harvested at different time intervals were analyzed by conventional magnetometry measurements (e.g. vibrating sample magnetometry (VSM), superconducting quantum interference device (SQUID)) and correlated with total iron quantifications, obtained via inductively coupled plasma mass spectrometry (ICP-MS) [33–35].

The magnetometry signal is then considered as a direct representation of the integrity of the nanoparticles: When the magnetic signal decreases while total iron remains constant, it is the signature of the nanoparticle degradation [33]. Despite bringing additional knowledge on the nanoparticle fate, these methods do not allow real-time analyses due to the impossibility of keeping cells viable along the experiments. Results are thus obtained on discrete samples and, as such, due to the multitude of samples needed, are either performed once a day on a short time period, or every few days or even weeks when on a longer time frame. Oppositely, probing properties at the nanoparticle level in real-time is important for monitoring their structure upon their potential degradation, or over their therapeutic action

Address correspondence to Aurore Van de Walle, aurore.vandewalle@univ-paris-diderot.fr; Laurence Motte, laurence.motte@univ-paris13.fr; Yoann Lalatonne, yoann.lalatonne@aphp.fr; Claire Wilhelm, claire.wilhelm@univ-paris-diderot.fr

(in operando). Such systems are being developed and the impact of magnetic nanoparticles heating on a thermosensitive surface coating has for example been monitored upon real-time magnetic hyperthermia application [36].

Standard magnetometry methods require the use of specific equipment that are often large scale and not readily available. Consequently, analysis of cell labeling efficiency on living cells right upon labeling is usually impossible. This remains an important limitation for any further biomedical application as nanoparticle type (core structure [37] and coating [38]), concentration, incubation time but also cell type [38] and donor [39] clearly influence the internalization rate. As a consequence, variations in labeling efficiency are not evaluated even though a tightly regulated "dose" of nanoparticles per cell is required as it might otherwise affect cellular functionality. Indeed, it has been shown that a high dose of nanoparticles can inhibit mesenchymal stem cell differentiation and even lead to cellular apoptosis [40–44].

A solution for a fast and effective quantification of nanoparticles' internalization within cells can be provided by a benchtop magnetic device first developed by Nikitin et al. and further explored for applications ranging from electrical engineering to life science [45, 46]. The physical concept is to expose the superparamagnetic nanoparticles to a two-frequency magnetic field and the resulting nonlinear magnetization of the nanoparticles generates a response signal which is strictly proportional to the quantities of magnetic nanoparticles.

Herein, thanks to this magnetic sensor system, we managed not only to quantify in real-time the internalization of magnetic nanoparticles within human stem cells, but also to monitor their integrity over days in a stem cells-derived spheroid-like tissue model [33–35], without impacting stem cells viability and differentiation capacity. It is a consequent advance compared to previous works where the use of conventional magnetometry precluded any measurement on living cells and thus only allowed discrete evaluation at time intervals very distant considering the kinetics of the degradation process. Moreover, the use of discrete sample was introducing the risk of biological variability. Besides being a technical challenge, the measurement of magnetic nanoparticles integrity in operando (in real time, *in situ*, on living cells, and upon degradation) could become a unique companion test to non-invasively characterize magnetically engineered tissues prior to implantation for regenerative medicine.

2 Material and Methods

2.1 Magnetic nanoparticles' synthesis

Magnetic nanoparticles were synthesized as previously described [47]. Briefly, 400 mg of iron(III) acetylacetonate (> 99.9%) (Sigma Aldrich) were dissolved in 10 mL of benzyl alcohol anhydrous (99.8%) (Sigma Aldrich). This solution was placed in a Monowave 300 from Anton Paar and the temperature of the suspension was increased up to 250 °C in 20 min then maintained constant for 30 minutes. The resulting suspension was precipitated using a neodymium magnet and washed successively with dichloromethane, sodium hydroxyde, ethanol, and water (pH = 7). A last washing step was performed in acidic water (pH = 2) and the nanoparticles were separated by ultracentrifugation using an Amicon® ultra centrifugal filters (30 kD). Finally, the magnetic nanoparticles were resuspended in acidic water (pH = 2) for further coating.

2.2 Magnetic nanoparticles' coating

Citric acid (from Sigma Aldrich) and polyethylene glycol (PEG) phosphonic carboxylic acid (from Specific Polymers, SP-1P-10-002, MW 2,500 g/mol) were dissolved in water at pH = 2. Coating must be in excess with mass ratio 5-times higher than nanoparticles. The coating molecule solution and nanoparticle dispersion were mixed and left for 2 hours under magnetic stirring. At the end of the reaction, pH was adjusted at 7, and the system is left to equilibrate for 2 h. Finally, nanoparticles were magnetically purified 3 times in water (pH = 2) then ultra-centrifuged at pH = 7 in Amicon® ultra centrifugal filters (30 kD). The two coatings are named in the following citrate and PEG.

2.3 Cell culture and nanoparticles' internalization

Human mesenchymal stem cells (Lonza) were cultured in MSCBM medium (Lonza) with the provided kit containing serum, glutamine and antibiotics, at 37 °C with 5% CO_2. Cells were amplified until passage 4–5 then were allowed to grow until near confluence prior to labelling. Cells were washed first with RPMI then incubated with the labelling solution for 24 h for PEG coating and for 30 min for citrate coating due to their faster internalization rate provided by the negative surface charge [34]. The labelling solution was composed of nanoparticles dispersed in serum-free RPMI-1640 medium (ThermoFischer Scientific) at iron concentrations between 0.1 and 4 mM. In the case of the experiments performed on citrate-coated nanoparticles in real-time, the media was supplemented with 5 mM sodium citrate. Upon labelling, cells were rinsed with RPMI then media was replaced by MSCBM medium for 1 h to allow a complete internalization of the nanoparticles before further processing (Fig. 1(a)).

2.4 Cell spheroids' formation and culture

Cells loaded with nanoparticles were detached with Trypsin-EDTA (0.05%) phenol red (thermoFisher Scientifc), then 200,000 cells were dispersed in 1.5 mL of medium in 15 mL Falcon® tubes before being centrifuged for 5 min at 120 g to form a high-density pellet. Pellets remained in culture at 37 °C and 5% CO_2 in medium composed of DMEM high glucose supplemented with 1% penicillin streptomycin, 1% ITS premix (Corning), with final concentrations of: 0.1 µM of dexamethasone (Sigma), 1 mM sodium pyruvate (Sigma), 50 µM ascorbic acid-2 phosphate (Sigma) and 0.35 mM L-proline (Sigma). The media was replenished twice a week. To induce extracellular matrix production, the growth factor TGF-β3 (10 ng/ml) was added to the culture medium.

For magnetometry analyses of discrete samples, spheroids were washed with cacodylate buffer (0.1 M) then fixed with a solution of 2% glutaraldehyde in 0.1 M cacodylate buffer for 30 min at room temperature and stored in PBS in order to measure their macroscopic magnetization at different days of the maturation process (days 1, 4, 8, and 21).

For real-time magnetometry analyses, the same sample remained in culture along the measurements with the magnetic sensor. The impact of real-time measurements on cell viability was also assessed by studying if it had an effect on cell function and associated tissue formation. To do so, stem cell spheroids cultured in medium supplemented with the growth factor TGF-β3 were continuously kept in the magnetic sensor for 6 days, time during which tissue formation is initiated, and were then kept in standard incubator for 15 extra days, to allow further extracellular matrix production. This extracellular matrix production was then observed with TEM and histology, quantified via PCR, and compared to control spheroids cultured in incubator only.

2.5 Magnetometry measurements using the magnetic sensor

The magnetic sensor was developed by Magnisense SA for diagnostic tests. Here it was used to quantify the iron oxide nanoparticles in the cellular environment (see photograph in Fig. S1(a) in the Electronic Supplementary Material (ESM)). The analysis is based on the non-linear superparamagnetic magnetization of the nanoparticles [48]. Briefly, an alternating magnetic field is applied to the sample at two different frequencies f_1 = 100 kHz and f_2 = 100 Hz of different amplitudes 10 and 200 Oe, respectively. The signal measured represents the third derivative of the sample magnetization at zero magnetic field and room temperature, proportional to the amount of nanoparticles within the sample.

For real-time measurement of cell spheroids magnetization, a 5% CO_2 environment was achieved via direct injection of 5% CO_2 into a home-made chamber. Temperature was adjusted such as the final temperature within the sensor remained at 37 °C. Control samples were kept in standard incubator, at 5% CO_2 and 37 °C.

2.6. Measurements via vibrating sample magnetometry (VSM)

VSM (Quantum Design, Versalab; see photograph in Fig. S1(b) in the ESM) measurements directly provided the magnetic moment (expressed in emu) of sample composed of 200,000 cells when submitted to a magnetic field. Field-dependent magnetization curves were recorded as a function of the applied filed between 0 and 25,000 Oe and provide magnetization at saturation.

2.7 Histological analyses

After 21 days of culture, cell aggregates were washed twice with PBS before being fixed in 4% paraformaldehyde. Samples were then embedded in optimal cutting temperature (OCT) compound, frozen using isopentane cooled in a liquid nitrogen bath, and cryosectionned (8 µm-thick slices). The slices were stained with Fast green and Safranin O (0.1%) to reveal the presence of extracellular matrix components (glycosaminoglycans).

2.8 Transmission electron microscopy (TEM) imaging

For TEM imaging, cells labelled with citrate nanoparticles were harvested at days 1 and 21. Samples were rinsed and fixed using 2% glutaraldehyde in 0.1 M cacodylate buffer (Sigma). Samples were then contrasted with oolong tea extract (OTE) 0.5% in cacodylate buffer, post fixed with 1% osmium tetroxide containing 1.5% potassium cyanoferrate then dehydrated in graded ethanol baths and embedded in Epon resin. Ultrathin sections (70 nm) were deposited onto 200 mesh cooper grids and examined (Mima2 INRA platform) with a Hitachi HT 7700 TEM operated at 80 kV with image acquisition using a charge-coupled device camera (AMT).

2.9 Relative quantification of gene expression by quantitative RT-PCR

Total RNA was extracted from spheroids of the magnetic sensor and of the incubator conditions (for these two conditions the spheroids were cultured with growth factors, to drive extracellular matrix production and tissue formation) using the total RNA isolation kit (Machery-Nagel). The synthesis of complementary DNA (cDNA) was then achieved using SuperScript II Reverse Transcriptase (Invitrogen). Real-time quantitative polymerase chain reaction was performed using the SYBRGreen dye (Applied Biosystems) and conducted with the StepOnePlus detection system (Thermo Fisher Scientific), according to the manufacturer's protocol. The specificity of the reaction was confirmed by melting curves analysis and the fluorescence cycle threshold (Ct) value of each mRNA was obtained. Relative expression of each gene was performed using the comparative Ct method. First, levels of genes of interest (I) mRNA were normalized to the housekeeping gene ribosomal protein large subunit P0 (RPLP0) ($\Delta Ct = Ct_I - Ct_{RPLP0}$). The relative amount of mRNA levels between the conditions assessed (magnetic sensor or incubator) and the control (spheroids cultured without growth factors in the standard incubator) is then given by $2^{-\Delta\Delta Ct}$, where $\Delta\Delta Ct = [\Delta Ct_I \text{ condition assessed}] - [\Delta Ct_I \text{ control}]$. See Table S1 in the ESM for primer sequences.

2.10 Statistics

All values are presented as mean ± standard deviation. Significance between groups was determined using independent Student's t-test. For all values, a minimum of 95% confidence level was considered significant, with $^*p < 0.05$, $^{**}p < 0.01$ and $^{***}p < 0.001$.

3 Results

3.1 Magnetic quantification of nanoparticles internalization and degradation in stem cells spheroids with both VSM magnetometry and magnetic sensor (discrete assessments)

Human stem cells were incubated with varying iron concentrations (0.5, 1, 2 and 4 mM) of the magnetic nanoparticles (Fig. 1(a)). A total of 200,000 stem cells were then pooled and centrifuged into forming a spheroid which could be kept in culture for up to 21 days in conditions that promote 3D tissue formation (Fig. 1(a)) [35]. Importantly, in this specific spheroid model, the stem cells stop dividing as soon as they are confined in 3D and start differentiating. As a consequence, no tissue necrosis is detected over the whole process of spheroid tissue maturation, which is up to the three weeks of culture, as observed on hematoxylin and eosin staining shown in Fig. S2 in the ESM. For discrete magnetic measurements, spheroid samples were collected at days 1, 4, 8, and 21 ($n \geq 3$ for each day), fixed, and magnetism was analyzed via both the magnetic sensor and the VSM as a standard measurement approach (Fig. 1(b)). These discrete measurements require the use of multiple samples for the follow-up of the cell magnetism over days, contrasting with continuous measurements on a same spheroid if the samples were kept alive (Fig. 1(c)). With VSM magnetometry, the magnetic moment of the spheroid sample is directly measured at varying magnetic field, providing both the magnetic susceptibility and the saturation magnetization, directly proportional to the amount of intact nanoparticles in the sample. For the magnetic sensor, the detection method is based on the nonlinearities of superparamagnetic nanoparticles magnetization. The method consists in measuring the nanoparticles nonlinear response upon exposure to a two-frequency alternating magnetic field. The two frequencies are generated by two independent coils, and were selected as f_1 = 100 kHz and f_2 = 100 Hz, with respective magnetic field amplitudes of B_1 = 10 Oe and B_2 = 200 Oe, respectively. For the lower f_2 frequency, the field amplitude is high enough to provide the nanoparticles with a magnetization close to saturation. The capacity of the nanoparticles to be further magnetized (by the application of the second field at high frequency f_2) is thus switched on (minimum of the low

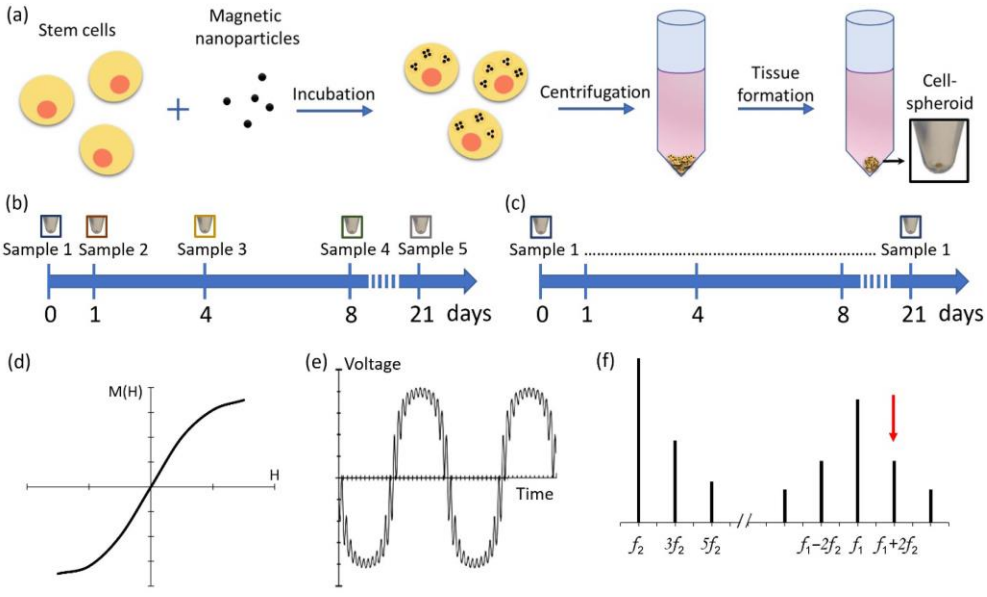

Figure 1 Experimental set-up. (a) Stem cells are incubated with magnetic nanoparticles and, upon internalization, the cells are centrifuged to form cohesive 3D spheroids. (b) Standard assessments of the integrity of magnetic nanoparticles in cells require the use of multiple independent samples due to the need of fixing them. (c) With the magnetic sensor, the cell spheroids can be kept viable and measurements can be performed on a same sample over long time-frames. (d) Typical non-linear magnetization curve of superparamagnetic nanoparticles showing the magnetic moment that flattens at high and low magnetic fields. (e) Time-dependent voltage of the samples when subjected to the two-frequency magnetic field in the magnetic sensor. This response signal flattens at the extrema due to the non-linear magnetization of the nanoparticles. (f) Specific combinatory frequencies in the Fourier-transformed response signal are proportional to the amount of magnetic nanoparticles (red arrow).

frequency high field) and off (maximum) sinusoidally. As a result, the voltage of the sensing coil is directly modulated by both frequencies. By performing the Fourier transform of this voltage, the response of the sample at the combinatorial frequency $f = f_1 \pm 2\ f_2$ is measured. Proportional to the third derivative of the sample magnetization around zero field and room temperature, this response (expressed here in arbitrary units) is then directly proportional to the amount of nanoparticles inside the sample. Remarkably, because this combinatorial measurement gets rid of the background noise, the detection threshold is about 10 ng of iron oxide, or equivalently 10 billion of nanoparticles of 9 nm in diameter.

Figures 2(a)–2(d) presents all measurements obtained at different times of the spheroids' maturation. The VSM measurements (Figs. 2(a) and 2(b)) provide the magnetic moments of the samples, expressed in emu while the magnetic sensor values represent the magnetic signal measured by the sensor (Figs. 2(c) and 2(d)). The VSM data showed in Figs. 2(a) and 2(b) provide first the internalized dose of the nanoparticles (at day 1), these emu values can be converted into the number of internalized nanoparticles (a 9-nm nanoparticle has a magnetic moment at saturation of 10^{-16} emu), as depicted on the secondary vertical axis in the VSM graphs (Figs. 2(a) and 2(b)). These values correspond to 200,000 cells organized as a spheroid, providing therefore the mean number of nanoparticles within each cell, and revealing a nanoparticle internalization increasing with the incubation dose for both the citrate (Fig. 2(a)) and the PEG coating (Fig. 2(b)). Values are in the range of millions of nanoparticles per cell, 0.8, 1.3 and 4 million per cell for the citrate-coated nanoparticles incubated at [Fe] = 0.5, 1 and 2 mM, respectively; and 2.2, 3.5 and 6.1 million per cell for the PEG-coated nanoparticles incubated at [Fe] = 1, 2 and 4 mM, respectively. Following internalization, a progressive decrease in magnetism is observed over the 21 days of tissue culture, reflecting a decrease in the number of still intact nanoparticles within the tissue. Remarkably, the evolution of the magnetic sensor values upon nanoparticles degradation, shown in Figs. 2(c) and 2(d), is highly similar to the VSM measurements. Besides, and importantly, the total iron content within the spheroids was measured by elemental analysis (Fig. S3 in the ESM) and was found constant over the 21 days of tissue culture, discarding any possibility of cell death and subsequent iron release from the spheroids. Representative TEM images of the cells right after nanoparticle incubation (day 1) show all nanoparticles, about 9 nm in diameter, internalized within the endosomes of the cells (Figs. 2(e) and 2(f) and Fig. S4(a) in the ESM). After 21 days of culture, the apparition of ~ 6 nm dots, lighter than the initial nanoparticles, can be observed both within the endosomes and outside, dispersed in the cytoplasm of the cells (Figs. 2(g) and 2(h) and Fig. S4(b) in the ESM). These dots are representative of iron stored within the ferritin protein and can be correlated with the degradation of the nanoparticles and the consequent release of free iron.

3.2 A strong correlation between the magnetic sensor signal of intracellular nanoparticles and their VSM magnetic moment

All magnetic sensor values obtained on cellular samples are compared with the VSM measurements in Fig. 3, evidencing a strong correlation between the two techniques, with $R^2 > 0.99$, within a very large range of concentrations. The magnetic sensor signal can thus be equaled to a magnetic moment, expressed in emu. However, it has to be kept in mind that the signal obtained with the magnetic sensor depends on the size of the nanoparticles, and such correlation must be determined for each nanoparticle design. Importantly, herein the correlation remains unchanged between day 1 (first day of the nanoparticles within the cells) and at the following days (3 to 21), for samples where a proportion of nanoparticles are already degraded. It indicates that only intact (9 nm in diameter) nanoparticles are measured, meaning that the nanoparticles

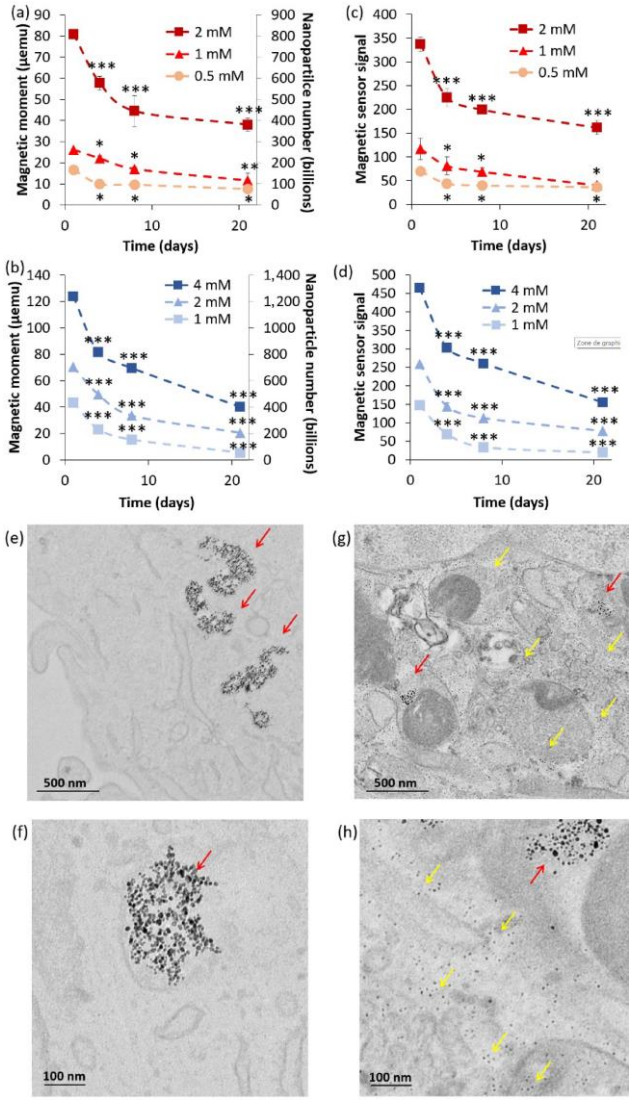

Figure 2 Progressive degradation of magnetic nanoparticles in a stem cell spheroid model similarly quantified via both magnetic sensor and VSM magnetometry techniques. (a) and (b) VSM magnetometry of the stem cells spheroids is performed at days 1, 4, 8, and 21. The saturation magnetic moments of the samples, expressed in μemu can be converted into a number of intact nanoparticles (1 μ emu equals 10 billion of 9 nm-diameter nanoparticles). Measurements are obtained for three different incubation concentrations and two coatings: (a) a citrate and (b) a PEG coating. ((c), (d)) Similar measurements on the same spheroids, with the magnetic sensor, expressed in the measurement unit of the device. Asterisks indicate significant differences when compared to day 0, $*p < 0.05$, $**p < 0.01$, $***p < 0.001$. ((e), (h)). Representative TEM images of the cells at day 1 ((e), (f)) and day 21 ((g), (h)). At day 1 ((e), (f)), dark dots can be observed, representative of the nanoparticles that are initially internalized in the endosomes of the cells. At day 21 ((g), (h)), light grey dots appear in the endosomes and the cytoplasm, ranging in the size of the storage ferritin protein loaded with iron. Remaining intact nanoparticles (dark dots) can also be observed in the endosomes. Red arrows: intact nanoparticles; yellow arrows: ferritin proteins.

are either still intact or fully degraded, thus not contributing neither to the VSM signal, nor the magnetic sensor one.

3.3 Real-time *in situ* follow-up of the nanoparticles degradation in the stem cells spheroids

To investigate the potential of the magnetic sensor to monitor nanoparticle biodegradation *in situ* within living cells, on the exact same spheroid, independent spheroids were first placed in a traditional incubator and measured once a day using the magnetic sensor. The aim was to observe if repeated punctual measurements of live cells spheroids could be achieved. Two intracellular doses of nanoparticles were chosen: a mild dose of 4–6 million nanoparticles per cell, dose achieved for the nanoparticles with the citrate coating; and a low dose of 1–2 million nanoparticles per cell, achieved with the PEG-coated nanoparticles, to test the limits of the sensor. Results are shown in Figs. 4(a) and 4(d), for citrate-coated and PEG-coated nanoparticles, respectively, and clearly demonstrate that the measurements are reliable, as shown by the progressive decrease in the magnetic sensor signal, the excellent reproducibility amongst the spheroids, and a similar degradation profile than the one obtained on fixed samples. Then, a home-made incubator was specifically adapted to the magnetic sensor, designed to mimic the culture conditions encountered in a traditional incubator, with 5% CO_2 and 37 °C temperature (Fig. S5 in the ESM). Using this set-up, continuous measurements were obtained on single spheroids for 6 days in a raw, with data taken every 0.5 seconds then averaged every 10 min. Typical curves of the resulting magnetic signal are shown in Figs. 4(b) and 4(c) and Figs. 4(e) and 4(f)), for citrate-coated and PEG-coated nanoparticles, respectively, and a progressive decrease in the signal is evidenced for all spheroids assessed, similarly to the data previously observed on punctual assessments (Figs. 4(a) and 4(d)). Besides, Figs. 4(b) and 4(e) correspond to single spheroid prepared and investigated at the same time as the ones measured punctually in Figs. 4(a) and 4(d), respectively. Instead of obtaining a regular decrease, degradation appeared intermittent. As a comparison standpoint, the degradation of nanoparticles in a solution mimicking the lysosomal environment of the cells (aqueous dispersion, pH 4, supplemented with 20 mM citrate serving as iron chelating agent) displayed a regular decrease (Fig. S6 in the ESM). After 6 days of real-time measurements, cell spheroids labeled with citrate were placed in the traditional incubator until day 21; they were then harvested and analyzed by TEM. Representative images (Figs. 4(g)–4(i) and Fig. S7 in the ESM) show the presence of light grey dots in the endosomes and the cytoplasm, corresponding to iron stored in ferritin proteins typically observed upon the degradation of magnetic nanoparticles, and confirming that degradation happens in a similar mode upon culture in the magnetic sensor.

Next step was to investigate any potential impact on stem cell functions (spheroid formation and differentiation capacity) of the real-time *in situ* continuous degradation monitoring inside the magnetic sensor. The chondrogenic differentiation was investigated, as it is the one differentiation possible in the 3D spheroid geometry, and also because it is the first differentiation to be impacted by environmental changes, such as exposure to nanoparticles [49]. First, images of the spheroids over time showed their progressive development as a cohesive 3D structure along and upon continuous recordings, suggesting spheroid formation and contractility indicative of functional cell–cell adhesions (Fig. 5(a)). Histological sections stained with hematoxylin and eosin also evidenced a cohesive viable tissue structure three weeks after spheroid formation, for both the spheroids cultured in the magnetic sensor and the ones in the conventional incubator (Fig. S7 in the ESM). Staining with Safranin O was then performed as an indicator of successful chondrogenesis through the production of proteoglycans (Fig. 5(b)). It evidenced that proteoglycans production is at the same level for the samples cultured in the magnetic sensor than for those cultured in the traditional incubator. TEM observations at day 21 similarly evidenced synthesis of extracellular matrix components in both the spheroids cultured in the magnetic

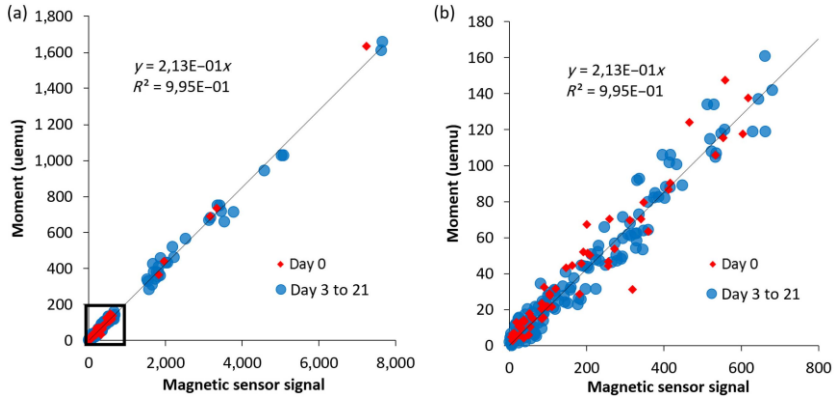

Figure 3 Correlation between the magnetic sensor signal and the magnetic moment obtained via VSM. ((a), (b)) A strong correlation is observed between the magnetic sensor and the VSM measurements of 9 nm iron oxide nanoparticles coated with citrate or PEG, internalized in stem cells and cultured for up to 21 days as cellular spheroids. (a) shows the correlation for the entire set of data and (b) is a close-up on the lower values (corresponding to the black square of (a)).

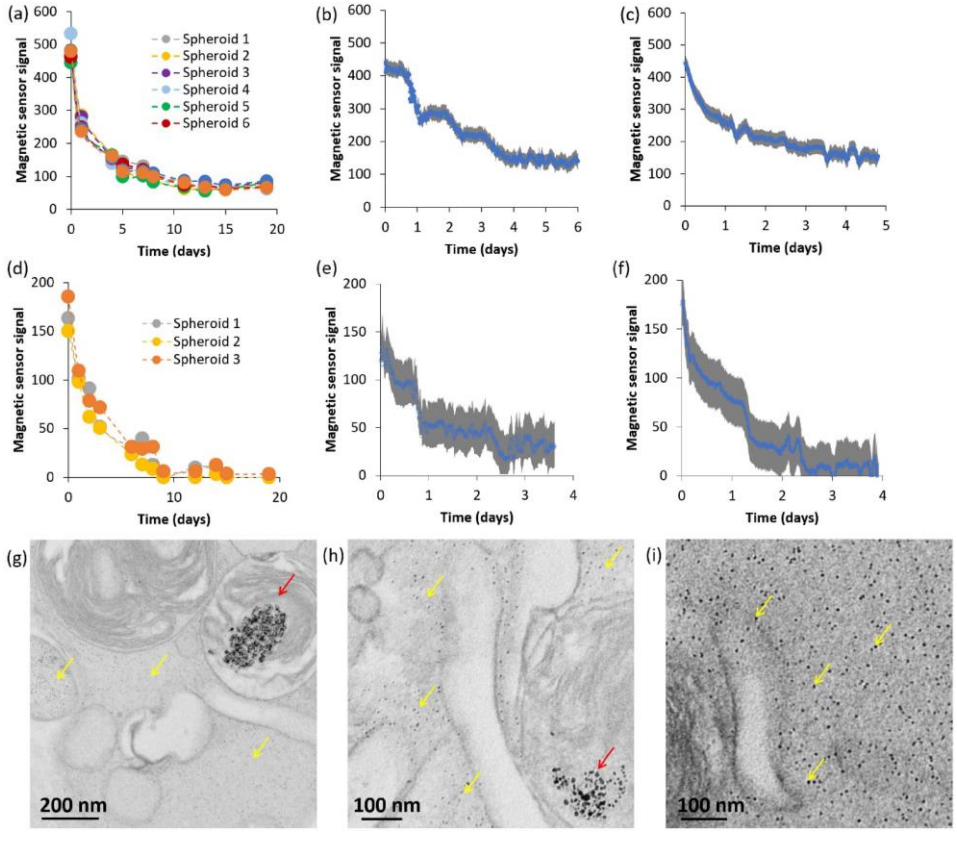

Figure 4 Magnetic sensor measurements allow long-term monitoring of the nanoparticles' biodegradation in operando on living cell spheroids. (a)–(f) Magnetism of cell spheroids is analyzed using the magnetic sensor, either every few days for a few minutes with the samples being cultured in a standard incubator for the remaining time ((a), (c)) or in real-time with data are obtained every 0.5 s for up to 6 continuous days and averaged every 10 min ((b), (d)–(f)) (the grey area represents the measurement variations coming from the device). The cells are labeled with magnetic nanoparticles either coated with citrate (a)–(c) or PEG (d)–(f). (g)–(i) TEM images taken upon 6 days of real-time recordings followed by traditional culture in an incubator for 15 days display the appearance of small grey dots (around 6 nm in diameter) in the endosomes and the cytoplasm of the cells, typical appearance of ferritin proteins loaded with iron released from the degradation of magnetic nanoparticles. Red arrows: intact nanoparticles; yellow arrows: ferritin proteins.

sensor (Fig. 5(c) and Fig. S8 in the ESM) as well as in the ones kept in the incubator (Fig. 5(d)). Finally, gene expression of extracellular matrix components specifically expressed during the chondrogenic differentiation of stem cells (aggrecan, collagen type X, cartilage oligomeric matrix protein, transcription factor sox 9) was assessed after 14 and 21 days of spheroid maturation. It displayed similar levels for the samples that were cultured in the magnetic sensor and for the ones remaining in the traditional incubator (Fig. 5(e)).

4 Discussion

There is undeniable potential for magnetic nanoparticles in biomedical applications [50]; however, the question of their fate once within the organism is not fully resolved yet. Studies performed *in vivo* demonstrated that injected nanoparticles are progressively degraded, join the iron pool, and integrate the iron metabolism [28, 29, 31, 32, 51]. More recently, quantitative measurements have been performed *in vitro* on a given pool of

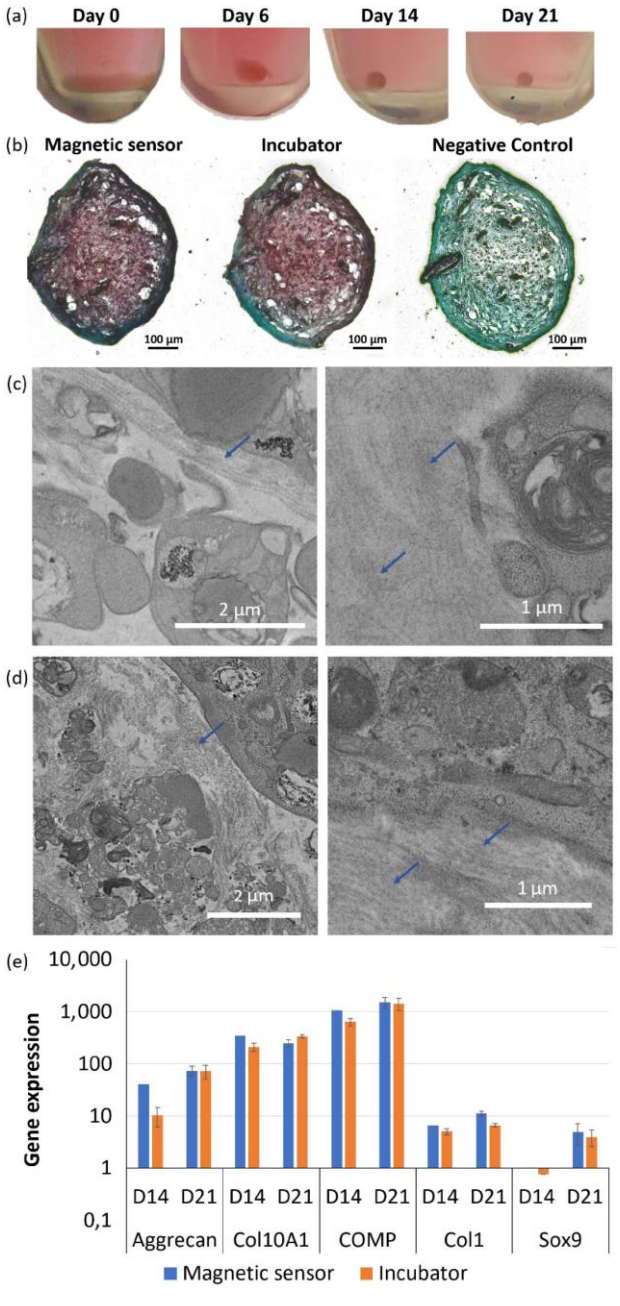

Figure 5 The cell spheroids remain viable along the real-time measurements using the magnetic sensor. (a) Representative photographs taken upon centrifugation of the cells at day 0 and after 6 days of culture and continuous magnetometry measurements in the magnetic sensor show that the cells formed a cohesive 3D cell spheroid, similar structure to the one obtained traditionally when cultured in an incubator. These spheroids are then cultured for 15 additional days in a traditional incubator (until day 21) and harvested for histology, PCR, and TEM analyses. (b) Representative histological images of aggregates fixed at day 21 and stained with Safranin O reveal the presence of extracellular matrix components (glycosaminoglycans) in the aggregates cultured in the sensor under continuous magnetometry measurements (magnetic sensor condition) as well as in the ones cultured in the traditional incubator only (incubator condition). For both these conditions, the aggregates are stimulated with growth factors to initiate ECM formation, while the negative control was cultured in the incubator and without growth factor. (c) and (d) Representative TEM images of samples cultured in the magnetic sensor (c) and in the incubator (d), after 21 days of culture with growth factors, show the formation of extracellular matrix (blue arrows) for both. (e) Gene expression of extracellular matrix components at days 14 and 21 display similar gene expression for the cell spheroids in the magnetic sensor or in the incubator.

cells [33–35]. In this case, contrary to the *in vivo* experiments, the entire pool of injected nanoparticles is followed on the long-term as no nanoparticle can circulate away from the system. The progressive degradation of nanoparticles within stem cells was demonstrated and reached up to 90% degradation over the course of a month [33]. It shed light on the transformations of nanoparticles within the cells; however, the integrity of the nanoparticles was tracked via their original magnetic properties that allow them to be monitored at a distance using magnetometry measurements; and these measures are performed on large-scale machines with limited accessibility, and impossible on living cells. As such, numerous discrete samples needed to be fixed for each data point resulting in data points at every few days only, and never on the exact same cell samples.

Herein, we introduce the use of a small, bench-top size, magnetic sensor for performing such assessments. This device provides a signal proportional to the magnetism of samples and was initially developed for immunoassays, using probes based on magnetic nanoparticles [48, 52]. It has further been expanded to study the synthesis and functionalization of magnetic nanoparticles [53, 54] and the internalization of nanoparticles in cells [55–57]. It also allowed the non-invasive monitoring of nanoparticles *in vivo*; either by assessing their blood half-life in the tail veins of mice [58] or by non-invasive monitoring of their long-term distribution in various organs upon intra-arterial injection [59]. In the present study, the magnetic sensor serves as an innovative tool to assess the transformations of the nanoparticles *in vitro*, in a tissue model based on stem cells [33–35]. Briefly, stem cells are labeled with magnetic nanoparticles, centrifuged, and kept in culture such as they form a 3D cohesive tissue in the shape of a spheroid. This tissue model is advantageous as the culture parameters prevent cell proliferation, and the tissue formed is easy to manipulate and to keep in culture for months. Moreover, stem cells are a cell-source of choice for regenerative medicine applications and a full comprehension of the intracellular fate of nanoparticles is required for transitioning to the clinic. Also, stem cells provide an intracellular environment containing a large range of biomolecules including, among others, proteins related to iron metabolism and responsible for the assimilation of magnetic nanoparticles in the biological environment.

Results first demonstrate that the magnetic sensor is a relevant approach for the follow-up of the intracellular integrity of nanoparticles. Data obtained on punctual samples show the progressive degradation of the nanoparticles *in cellulo*, similarly to observations obtained with conventional magnetometry approaches, in agreement with previous works [33–35]. When compared to the VSM technique, a strong correlation is observed ($R^2 > 0.99$) between both measurements and the signal acquired with the magnetic sensor can then be converted in a magnetic moment (expressed in emu). It has to be noted that this correlation should be achieved for each nanoparticle type, as the signal of the magnetic sensor depends on each nanoparticle system [60]. Interestingly, the correlation between the magnetic sensor and the VSM measurements remains unchanged even upon degradation of the nanoparticles. It means that only nanoparticles in the size range of the internalized ones (9 nm) are measured, indicating an all-or-nothing degradation of the nanoparticles (the nanoparticles are either intact or fully degraded).

Additionally, and quite remarkably, the magnetic sensor allowed real-time follow-up of the magnetism of living cell spheroids over days, delineating precise variations in the biotransformation of the nanoparticles. This real-time degradation

observed in the cell spheroid signal is much more fluctuated than the ones of the same nanoparticles in an aqueous medium at pH 4.5 with iron chelating agent (citrate), often used as lysosomal-like medium [61, 62], where the magnetism decrease is regular. The more irregular degradation process is probably, and logically, linked to biological processes.

Remarkably, the cell spheroids subjected to continuous magnetic sensor measurements remained totally functional, opening up to the real-time tracking of magnetic nanoparticles in tissues, important for some applications where the diagnostic and therapeutic potential of the nanoparticles in the long-term depend on their stability in the biological environment. The degradation of the nanoparticles could for example lead to a loss of signal in MRI imaging, an issue if the goal is to track implanted cells or grafts over a long period of time [63, 64]. Moreover, the remote control of cells' spatial arrangements would also be reduced thus impacting *in vivo* targeting abilities and the magnetic development of 3D tissue constructs.

To conclude, the magnetic sensor is a small bench-top machine that can be easily set into a laboratory and used for a fast screen of cell labeling efficiency and for the *in situ* follow-up of time dependent nanoparticles' integrity, both on living cells.

Acknowledgements

This work was supported by the European Research Council (ERC-2014-CoG project MaTissE #648779). The authors would like to acknowledge the CNanoMat physico-chemical characterizations platform of University Paris 13, and Nicolas Chevalier for his help in controlling the CO_2 level in thehome-made incubator associated to the magnetic sensor.

Electronic Supplementary Material: Supplementary material (photographs of the magnetometers, additional TEM and histology images, additional real-time curves) is available in the online version of this article at https:// doi.org/10.1007/ s12274-020-2631-1.

References

[1] Wei, H.; Bruns, O. T.; Kaul, M. G.; Hansen, E. C.; Barch, M.; Wiśniowska, A.; Chen, O.; Chen, Y.; Li, N.; Okada, S. et al. Exceedingly small iron oxide nanoparticles as positive MRI contrast agents. *Proc. Natl. Acad. Sci. U.S.A* **2017**, *114*, 2325–2330.

[2] Hachani, R.; Lowdell, M.; Birchall, M.; Hervault, A.; Mertz, D.; Begin-Colin, S.; Thanh, N. T. K. Polyol synthesis, functionalisation, and biocompatibility studies of superparamagnetic iron oxide nanoparticles as potential MRI contrast agents. *Nanoscale* **2016**, *8*, 3278–3287.

[3] Blanco-Andujar, C.; Walter, A.; Cotin, G.; Bordeianu, C.; Mertz, D.; Felder-Flesch, D.; Begin-Colin, S. Design of iron oxide-based nanoparticles for MRI and magnetic hyperthermia. *Nanomedicine* **2016**, *11*, 1889–1910.

[4] Cotin, G.; Blanco-Andujar, C.; Nguyen, D. V.; Affolter, C.; Boutry, S.; Boos, A.; Ronot, P.; Uring-Lambert, B.; Choquet, P.; Zorn, P. E. et al. Dendron based antifouling, MRI and magnetic hyperthermia properties of different shaped iron oxide nanoparticles. *Nanotechnology* **2019**, *30*, 374002.

[5] Cortajarena, A. L.; Ortega, D.; Ocampo, S. M.; Gonzalez-García, A.; Couleaud, P.; Miranda, R.; Belda-Iniesta, C.; Ayuso-Sacido, A. Engineering iron oxide nanoparticles for clinical settings. *Nanobiomedicine* **2014**, *1*, 2.

[6] Johannsen, M.; Thiesen, B.; Wust, P.; Jordan, A. Magnetic nanoparticle hyperthermia for prostate cancer. *Int. J. Hyperthermia* **2010**, *26*, 790–795.

[7] Blanco-Andujar, C.; Teran, F. J.; Ortega, D. Current outlook and perspectives on nanoparticle-mediated magnetic hyperthermia. In *Iron Oxide Nanoparticles for Biomedical Applications*. Mahmoudi, M.; Laurent, S., Eds.; Metal Oxides: Elsevier, 2018; pp 197–245.

[8] Maier-Hauff, K.; Ulrich, F.; Nestler, D.; Niehoff, H.; Wust, P.; Thiesen, B.; Orawa, H.; Budach, V.; Jordan, A. Efficacy and safety of intratumoral thermotherapy using magnetic iron-oxide nanoparticles combined with external beam radiotherapy on patients with recurrent glioblastoma multiforme. *J. Neurooncol*. **2011**, *103*, 317–324.

[9] Espinosa, A.; Kolosnjaj-Tabi, J.; Abou-Hassan, A.; Sangnier, A. P.; Curcio, A.; Silva, A. K. A.; Di Corato, R.; Neveu, S.; Pellegrino, T.; Liz-Marzán, L. M. et al. Magnetic (Hyper)thermia or photothermia? Progressive comparison of iron oxide and gold nanoparticles heating in water, in cells, and *in vivo*. Adv. *Funct. Mater*. **2018**, *28*, 1803660.

[10] Kakwere, H.; Leal, M. P.; Materia, M. E.; Curcio, A.; Guardia, P.; Niculaes, D.; Marotta, R.; Falqui, A.; Pellegrino, T. Functionalization of strongly interacting magnetic nanocubes with (thermo)responsive coating and their application in hyperthermia and heat-triggered drug delivery. *ACS Appl. Mater. Interfaces* **2015**, *7*, 10132–10145.

[11] Sandre, O.; Genevois, C.; Garaio, E.; Adumeau, L.; Mornet, S.; Couillaud, F. *In vivo* imaging of local gene expression induced by magnetic hyperthermia. *Genes* **2017**, *8*, 61.

[12] Cazares-Cortes, E.; Cabana, S.; Boitard, C.; Nehlig, E.; Griffete, N.; Fresnais, J.; Wilhelm, C.; Abou-Hassan, A.; Ménager, C. Recent insights in magnetic hyperthermia: From the "hot-spot" effect for local delivery to combined magneto-photo-thermia using magneto-plasmonic hybrids. *Adv. Drug Deliv. Rev*. **2019**, *138*, 233–246.

[13] Blanco-Andujar, C.; Ortega, D.; Southern, P.; Pankhurst, Q. A.; Thanh, N. T. K. High performance multi-core iron oxide nanoparticles for magnetic hyperthermia: Microwave synthesis, and the role of core-to-core interactions. *Nanoscale* **2015**, *7*, 1768–1775.

[14] Asensio, J. M.; Marbaix, J.; Mille, N.; Lacroix, L. M.; Soulantica, K.; Fazzini, P. F.; Carrey, J.; Chaudret, B. To heat or not to heat: A study of the performances of iron carbide nanoparticles in magnetic heating. *Nanoscale* **2019**, *11*, 5402–5411.

[15] Hallali, N.; Clerc, P.; Fourmy, D.; Gigoux, V.; Carrey, J. Influence on cell death of high frequency motion of magnetic nanoparticles during magnetic hyperthermia experiments. *Appl. Phys. Lett*. **2016**, *109*, 032402.

[16] Plan Sangnier, A.; Preveral, S.; Curcio, A.; Silva, A. K. A.; Lefèvre, C. T.; Pignol, D.; Lalatonne, Y.; Wilhelm, C. Targeted thermal therapy with genetically engineered magnetite magnetosomes@RGD: Photothermia is far more efficient than magnetic hyperthermia. *J. Control. Release* **2018**, *279*, 271–281.

[17] Chu, M. Q.; Shao, Y. X.; Peng, J. L.; Dai, X. Y.; Li, H. K.; Wu, Q. S.; Shi, D. L. Near-infrared laser light mediated cancer therapy by photothermal effect of Fe_3O_4 magnetic nanoparticles. *Biomaterials* **2013**, *34*, 4078–4088.

[18] Zhou, Z. G.; Sun, Y. N.; Shen, J. C.; Wei, J.; Yu, C.; Kong, B.; Liu, W.; Yang, H.; Yang, S. P.; Wang, W. Iron/iron oxide core/shell nanoparticles for magnetic targeting MRI and near-infrared photothermal therapy. *Biomaterials* **2014**, *35*, 7470–7478.

[19] Shen, S.; Wang, S.; Zheng, R.; Zhu, X. Y.; Jiang, X. G.; Fu, D. L.; Yang, W. L. Magnetic nanoparticle clusters for photothermal therapy with near-infrared irradiation. *Biomaterials* **2015**, *39*, 67–74.

[20] Ye, D. W.; Li, Y.; Gu, N. Magnetic labeling of natural lipid encapsulations with iron-based nanoparticles. *Nano Res*. **2018**, *11*, 2970–2991.

[21] Ulbrich, K.; Holá, K.; Šubr, V.; Bakandritsos, A.; Tuček, J.; Zbořil, R. Targeted drug delivery with polymers and magnetic nanoparticles: Covalent and noncovalent approaches, release control, and clinical studies. *Chem. Rev*. **2016**, *116*, 5338–5431.

[22] Carregal-Romero, S.; Guardia, P.; Yu, X.; Hartmann, R.; Pellegrino, T.; Parak, W. J. Magnetically triggered release of molecular cargo from iron oxide nanoparticle loaded microcapsules. *Nanoscale* **2015**, *7*, 570–576.

[23] Mertz, D.; Sandre, O.; Bégin-Colin, S. Drug releasing nanoplatforms activated by alternating magnetic fields. *Biochim. Biophys. Acta Gen. Subj*. **2017**, *1861*, 1617–1641.

[24] Adedoyin, A. A.; Ekenseair, A. K. Biomedical applications of magneto-responsive scaffolds. *Nano Res*. **2018**, *11*, 5049–5064.

[25] Souza, G. R.; Molina, J. R.; Raphael, R. M.; Ozawa, M. G.; Stark, D. J.; Levin, C. S.; Bronk, L. F.; Ananta, J. S.; Mandelin, J.; Georgescu, M. M. et al. Three-dimensional tissue culture based on magnetic cell levitation. *Nat. Nanotechnol*, **2010**, *5*, 291–296.

[26] Mattix, B.; Olsen, T. R.; Gu, Y.; Casco, M.; Herbst, A.; Simionescu, D. T.; Visconti, R. P.; Kornev, K. G.; Alexis, F. Biological magnetic cellular spheroids as building blocks for tissue engineering. *Acta Biomater*. **2014**, *10*, 623–629.
[27] Hachani, R.; Lowdell, M.; Birchall, M.; Thanh, N. T. K. Tracking stem cells in tissue-engineered organs using magnetic nanoparticles. *Nanoscale* **2013**, *5*, 11362–11373.
[28] Pham, B. T. T.; Colvin, E. K.; Pham, N. T. H.; Kim, B. J.; Fuller, E. S.; Moon, E. A.; Barbey, R.; Yuen, S.; Rickman, B. H.; Bryce, N. S. et al. Biodistribution and clearance of stable superparamagnetic maghemite iron oxide nanoparticles in mice following intraperitoneal administration. *Int. J. Mol. Sci*. **2018**, *19*, 205.
[29] Bargheer, D.; Giemsa, A.; Freund, B.; Heine, M.; Waurisch, C.; Stachowski, G. M.; Hickey, S. G.; Eychmüller, A.; Heeren, J.; Nielsen, P. The distribution and degradation of radiolabeled superparamagnetic iron oxide nanoparticles and quantum dots in mice. *Beilstein J. Nanotechnol*. **2015**, *6*, 111–123.
[30] Freund, B.; Tromsdorf, U. I.; Bruns, O. T.; Heine, M.; Giemsa, A.; Bartelt, A.; Salmen, S. C.; Raabe, N.; Heeren, J.; Ittrich, H. et al. A simple and widely applicable method to ^{59}Fe-radiolabel monodisperse superparamagnetic iron oxide nanoparticles for *in vivo* quantification studies. *ACS Nano* **2012**, *6*, 7318–7325.
[31] Singh, S. P.; Rahman, M. F.; Murty, U. S. N.; Mahboob, M.; Grover, P. Comparative study of genotoxicity and tissue distribution of nano and micron sized iron oxide in rats after acute oral treatment. *Toxicol. Appl. Pharmacol*. **2013**, *266*, 56–66.
[32] Gu, L.; Fang, R. H.; Sailor, M. J.; Park, J. H. *In vivo* clearance and toxicity of monodisperse iron oxide nanocrystals. *ACS Nano* **2012**, *6*, 4947–4954.
[33] Mazuel, F.; Espinosa, A.; Luciani, N.; Reffay, M.; Le Borgne, R.; Motte, L.; Desboeufs, K.; Michel, A.; Pellegrino, T.; Lalatonne, Y. et al. Massive intracellular biodegradation of iron oxide nanoparticles evidenced magnetically at single-endosome and tissue levels. *ACS Nano* **2016**, *10*, 7627–7638.
[34] Plan Sangnier, A.; Van De Walle, A. B.; Curcio, A.; Le Borgne, R.; Motte, L.; Lalatonne, Y.; Wilhelm, C. Impact of magnetic nanoparticle surface coating on their long-term intracellular biodegradation in stem cells. *Nanoscale* **2019**, *11*, 16488–16498.
[35] Van De Walle, A.; Plan Sangnier, A.; Abou-Hassan, A.; Curcio, A.; Hémadi, M.; Menguy, N.; Lalatonne, Y.; Luciani, N.; Wilhelm, C. Biosynthesis of magnetic nanoparticles from nano-degradation products revealed in human stem cells. *Proc. Natl. Acad. Sci. USA* **2019**, *116*, 4044–4053.
[36] Hemery, G.; Garanger, E.; Lecommandoux, S.; Wong, A. D.; Gillies, E. R.; Pedrono, B.; Bayle, T.; Jacob, D.; Sandre, O. Thermosensitive polymer-grafted iron oxide nanoparticles studied by *in situ* dynamic light backscattering under magnetic hyperthermia. *J. Phys. D.: Appl. Phys*. **2015**, *48*, 494001.
[37] Wang, L.; Wang, Z. J.; Li, X. M.; Zhang, Y.; Yin, M.; Li, J.; Song, H. Y.; Shi, J. Y.; Ling, D. S.; Wang, L. H. et al. Deciphering active biocompatibility of iron oxide nanoparticles from their intrinsic antagonism. *Nano Res*. **2018**, *11*, 2746–2755.
[38] Wilhelm, C.; Gazeau, F. Universal cell labelling with anionic magnetic nanoparticles. *Biomaterials* **2008**, *29*, 3161–3174.
[39] Negi, H.; Takeuchi, S.; Kamei, N.; Yanada, S.; Adachi, N.; Ochi, M. *In vitro* safety and quality of magnetically labeled human mesenchymal stem cells preparation for cartilage repair. *Tissue Eng. Part C: Methods* **2019**, *25*, 324–333.
[40] Van De Walle, A.; Faissal, W.; Wilhelm, C.; Luciani, N. Role of growth factors and oxygen to limit hypertrophy and impact of high magnetic nanoparticles dose during stem cell chondrogenesis. *Comput. Struct. Biotechnol. J*. **2018**, *16*, 532–542.
[41] Chang, Y. K.; Liu, Y. P.; Ho, J. H.; Hsu, S. C.; Lee, O. K. Amine-surface-modified superparamagnetic iron oxide nanoparticles interfere with differentiation of human mesenchymal stem cells. *J. Orthop. Res*. **2012**, *30*, 1499–1506.
[42] Chen, Y. C.; Hsiao, J. K.; Liu, H. M.; Lai, I. Y.; Yao, M.; Hsu, S. C.; Ko, B. S.; Chen, Y. C.; Yang, C. S.; Huang, D. M. The inhibitory effect of superparamagnetic iron oxide nanoparticle (Ferucarbotran) on osteogenic differentiation and its signaling mechanism in human mesenchymal stem cells. *Toxicol. Appl. Pharmacol*. **2010**, *245*, 272–279.
[43] Huang, D. M.; Hsiao, J. K.; Chen, Y. C.; Chien, L. Y.; Yao, M.; Chen, Y. K.; Ko, B. S.; Hsu, S. C.; Tai, L. A.; Cheng, H. Y.. The promotion of human mesenchymal stem cell proliferation by superparamagnetic iron oxide nanoparticles. *Biomaterials* **2009**, *30*, 3645–3651.
[44] Roeder, E.; Henrionnet, C.; Goebel, J. C.; Gambier, N.; Beuf, O.; Grenier, D.; Chen, B. L.; Vuissoz, P. A.; Gillet, P.; Pinzano, A. Dose-response of superparamagnetic iron oxide labeling on mesenchymal stem cells chondrogenic differentiation: A multi-scale *in vitro* study. *PLoS One* **2014**, *9*, e98451.
[45] Nikitin, P. I.; Vetoshko, P. M.; Ksenevich, T. I. New type of biosensor based on magnetic nanoparticle detection. *J. Magn. Magn. Mater*. **2007**, *311*, 445–449.
[46] Lenglet, L.; Motte, L. Neel effect: Exploiting the nonlinear behavior of superparamagnetic nanoparticles for applications in life sciences up to electrical engineering. In *Novel Magnetic Nanostructures*. Domracheva, N.; Caporali, M.; Rentschler, E., Eds.; Elsevier: Amsterdam, **2018**; pp 247–265.
[47] Richard, S.; Eder, V.; Caputo, G.; Journé, C.; Ou, P.; Bolley, J.; Louedec, L.; Guenin, E.; Motte, L.; Pinna, N. et al. USPIO size control through microwave nonaqueous sol-gel method for neoangiogenesis T_2 MRI contrast agent. *Nanomedicine* (*Lond*) **2016**, *11*, 2769–2779.
[48] Motte, L.; Benyettou, F.; De Beaucorps, C.; Lecouvey, M.; Milesovic, I.; Lalatonne, Y. Multimodal superparamagnetic nanoplatform for clinical applications: Immunoassays, imaging & therapy. *Faraday Discuss*. **2011**, *149*, 211–225.
[49] Kostura, L.; Kraitchman, D. L.; Mackay, A. M.; Pittenger, M. F.; Bulte, J. W. M. Feridex labeling of mesenchymal stem cells inhibits chondrogenesis but not adipogenesis or osteogenesis. *NMR Biomed*. **2004**, *17*, 513–517.
[50] Assa, F.; Jafarizadeh-Malmiri, H.; Ajamein, H.; Anarjan, N.; Vaghari, H.; Sayyar, Z.; Berenjian, A. A biotechnological perspective on the application of iron oxide nanoparticles. *Nano Res*. **2016**, *9*, 2203–2225.
[51] Tamion, A.; Hillenkamp, M.; Hillion, A.; Maraloiu, V. A.; Vlaicu, I. D.; Stefan, M.; Ghica, D.; Rositi, H.; Chauveau, F.; Blanchin, M. G. et al. Ferritin surplus in mouse spleen 14 months after intravenous injection of iron oxide nanoparticles at clinical dose. *Nano Res*. **2016**, *9*, 2398–2410.
[52] Nikitin, P. I.; Vetoshko, P. M.; Ksenevich, T. I. Magnetic immunoassays. *Sens. Lett*. **2007**, *5*, 296–299.
[53] Guénin, E.; Lalatonne, Y.; Bolley, J.; Milosevic, I.; Platas-Iglesias, C.; Motte, L. Catechol versus bisphosphonate ligand exchange at the surface of iron oxide nanoparticles: Towards multi-functionalization. *J. Nanopart. Res*. **2014**, *16*, 2596.
[54] Milosevic, I.; Warmont, F.; Lalatonne, Y.; Motte, L. Magnetic metrology for iron oxide nanoparticle scaled-up synthesis. *RSC Adv*. **2014**, *4*, 49086–49089.
[55] Geinguenaud, F.; Souissi, I.; Fagard, R.; Motte, L.; Lalatonne, Y. Electrostatic assembly of a DNA superparamagnetic nano-tool for simultaneous intracellular delivery and *in situ* monitoring. *Nanomedicine* **2012**, *8*, 1106–1115.
[56] Geinguenaud, F.; Souissi, I.; Fagard, R.; Lalatonne, Y.; Motte, L. Easily controlled grafting of oligonucleotides on γFe_2O_3 Nanoparticles: Physicochemical characterization of DNA organization and biological activity studies. *J. Phys. Chem. B* **2014**, *118*, 1535–1544.
[57] Benyettou, F.; Fahs, H.; Elkharrag, R.; Bilbeisi, R. A.; Asma, B.; Rezgui, R.; Motte, L.; Magzoub, M.; Brandel, J.; Olsen, J. C. et al. Selective growth inhibition of cancer cells with doxorubicin-loaded CB[7]-modified iron-oxide nanoparticles. *RSC Adv*. **2017**, *7*,23827–23834.
[58] Nikitin, M. P.; Vetoshko, P. M.; Brusentsov, N. A.; Nikitin, P. I. Highly sensitive room-temperature method of non-invasive *in vivo* detection of magnetic nanoparticles. *J. Magn. Magn. Mater*. **2009**, *321*, 1658–1661.
[59] Nikitin, M.; Yuriev, M.; Brusentsov, N.; Vetoshko, P.; Nikitin, P. Non-invasive *in vivo* mapping and long-term monitoring of magnetic nanoparticles in different organs of animals. *AIP Conf. Proc*. **2010**, *1311*, 452–457.
[60] De Montferrand, C.; Hu, L.; Milosevic, I.; Russier, V.; Bonnin, D.; Motte, L.; Brioude, A.; Lalatonne, Y. Iron oxide nanoparticles with sizes, shapes and compositions resulting in different magnetization signatures as potential labels for multiparametric detection. *Acta*

Biomater. **2013**, *9*, 6150–6157.

[61] Arbab, A. S.; Wilson, L. B.; Ashari, P.; Jordan, E. K.; Lewis, B. K.; Frank, J. A. A model of lysosomal metabolism of dextran coated superparamagnetic iron oxide (SPIO) nanoparticles: Implications for cellular magnetic resonance imaging. *NMR Biomed*. **2005**, *18*, 383–389.

[62] Gutiérrez, L.; Romero, S.; Da Silva, G. B.; Costo, R.; Vargas, M. D.; Ronconi, C. M.; Serna, C. J.; Veintemillas-Verdaguer, S.; Del Puerto Morales, M. Degradation of magnetic nanoparticles mimicking lysosomal conditions followed by AC susceptibility. *Biomed. Tech.* (*Berl*) **2015**, *60*, 417–425.

[63] Soenen, S. J. H.; Himmelreich, U.; Nuytten, N.; Pisanic II, T. R.; Ferrari, A.; De Cuyper, M. Intracellular nanoparticle coating stability determines nanoparticle diagnostics efficacy and cell functionality. *Small* **2010**, *6*, 2136–2145.

[64] Garcés, V.; Rodríguez-Nogales, A.; González, A.; Gálvez, N.; Rodríguez-Cabezas, M. E.; García-Martin, M. L.; Gutiérrez, L.; Rondón, D.; Olivares, M.; Gálvez, J. et al. Bacteria-carried iron oxide nanoparticles for treatment of anemia. *Bioconjugate Chem*. **2018**, *29*, 1785–1791.

Electronic Supplementary Material

Real-time *in situ* magnetic measurement of the intracellular biodegradation of iron oxide nanoparticles in a stem cell-spheroid tissue model

Aurore Van de Walle[1] (✉), Alexandre Fromain[1], Anouchka Plan Sangnier[1,2], Alberto Curcio[1], Luc Lenglet[3], Laurence Motte[2] (✉), Yoann Lalatonne[2,4] (✉), and Claire Wilhelm[1] (✉)

[1] *Laboratoire Matière et Systèmes, Complexes MSC, UMR 7057, CNRS & University Paris Diderot, 75205, Paris Cedex 13, France*
[2] *Inserm, U1148, Laboratory for Vascular Translational Science, Université Paris 13, Sorbonne Paris Cité, F-93017 Bobigny, France*
[3] *Normafin Sàrl, 8 rue Mathilde Girault, 92300 Levallois-Perret, France*
[4] *Services de Biochimie et Médecine Nucléaire, Hôpital Avicenne Assistance Publique-Hôpitaux de Paris F-93009 Bobigny, France*

Supporting information to https://doi.org/10.1007/s12274-020-2631-1

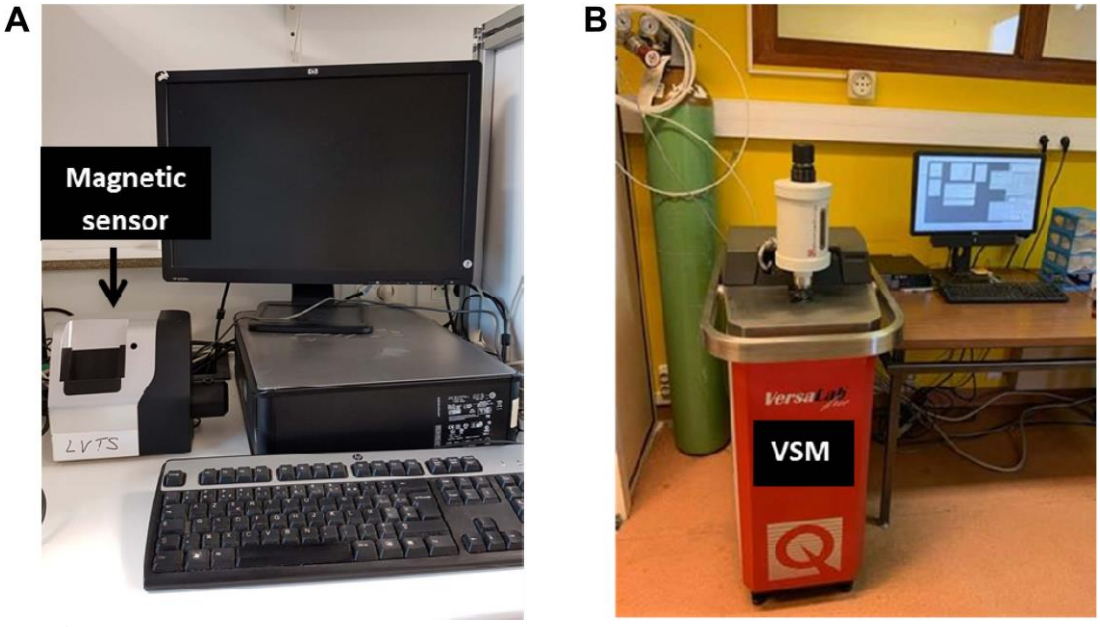

Figure S1 Photos of the two magnetometers used: A) the magnetic sensor and B) the VSM. When comparing the size to the computer in each image, it clearly appears that the VSM is larger.

Address correspondence to Aurore Van de Walle, aurore.vandewalle@univ-paris-diderot.fr; Laurence Motte, laurence.motte@univ-paris13.fr; Yoann Lalatonne, yoann.lalatonne@aphp.fr; Claire Wilhelm, claire.wilhelm@univ-paris-diderot.fr

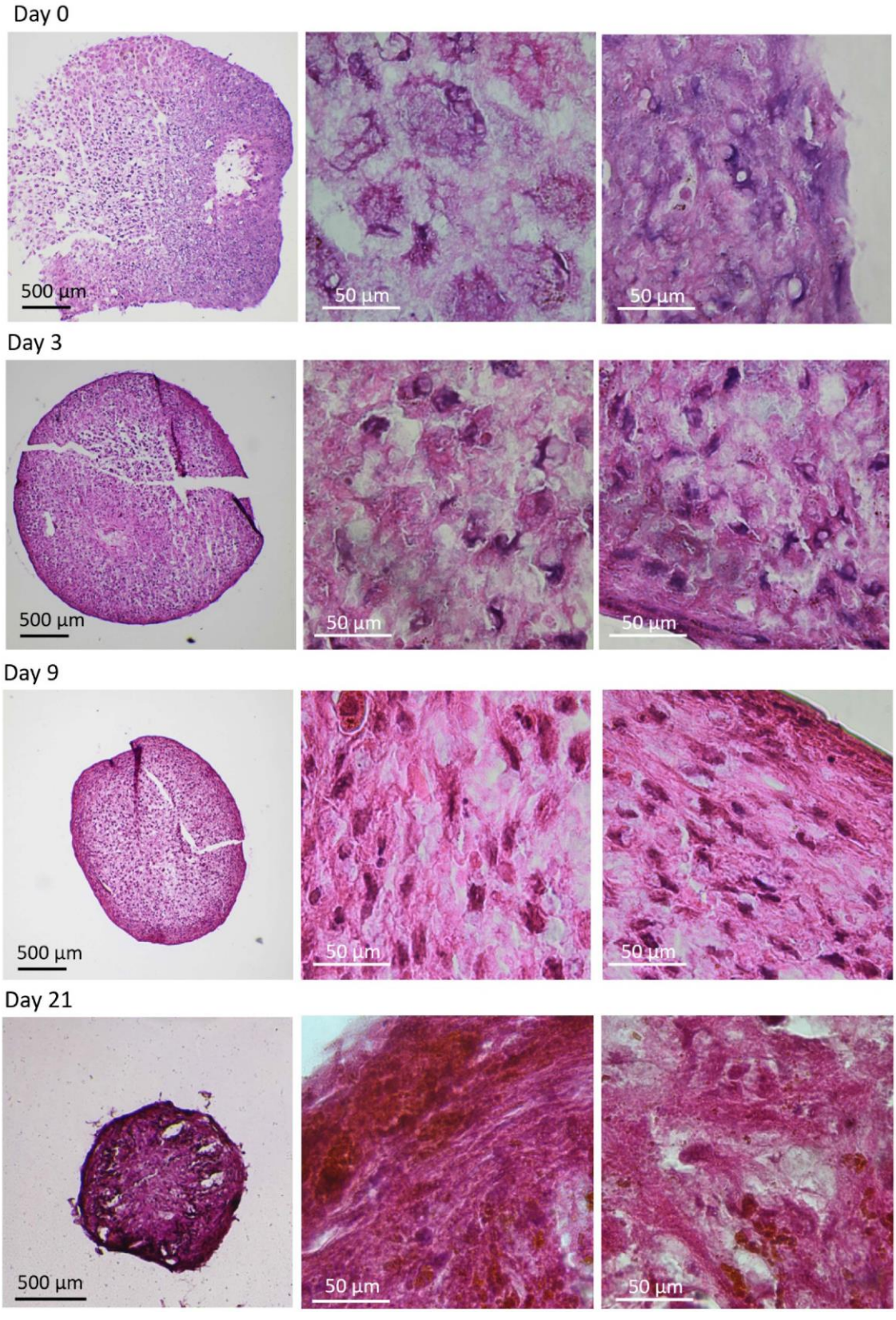

Figure S2 Hematoxylin and eosin staining of the spheroids made of stem cells, the day of their formation (day 0, loose structure), 3 days after (day 3, more cohesive structure), and 9 days later (day 9, compact spheroid). The hematoxylin stains the cell nuclei in dark red, and eosin stains the extracellular matrix and cytoplasm of live cells in pink. For all maturation times, the component cells appear viable.

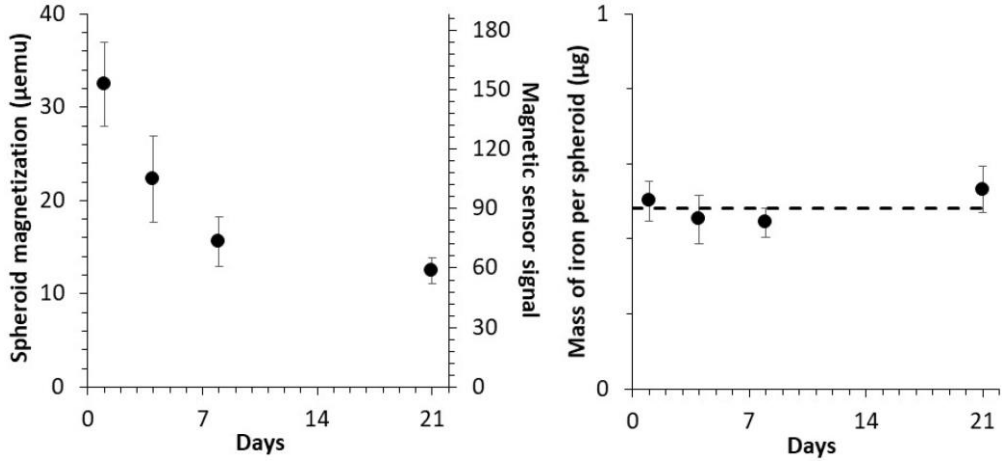

Figure S3 Measurements of spheroid magnetism (left) and spheroid iron content (right) were performed at different times after spheroid formation (days 1, 3, 9 and 21). Spheroids magnetism signal, expressed in µemu from the VSM measurement, and in the magnetic sensor signal (secondary axis) progressively decreases overtime. Oppositely, total iron, measured via ICP, remains constant.

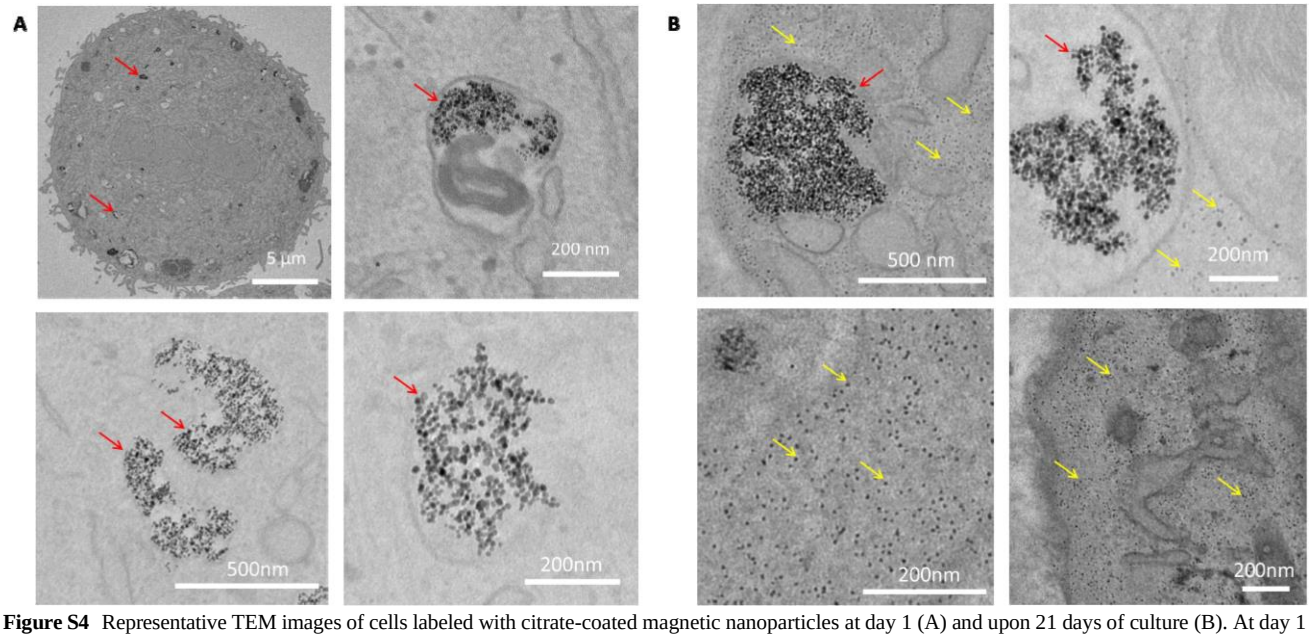

Figure S4 Representative TEM images of cells labeled with citrate-coated magnetic nanoparticles at day 1 (A) and upon 21 days of culture (B). At day 1 (A) the magnetic nanoparticles are internalized in the endosomes of the cells. At day 21 (B) some nanoparticles that remained intact can be observed in the endosomes, and small grey dots can be observed in the endosomes and the cytoplasm corresponding to the size and appearance of ferritin proteins loaded with iron.

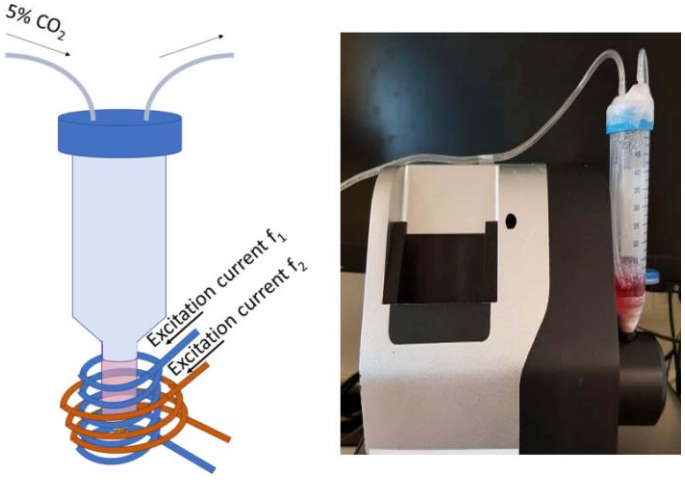

Figure S5 Design of the"home-made" bioreactor. In order to obtain these culture parameters, a 5% CO_2 bottle was directly attached to the entrance of 50 mL Falcon tube, itself clipped to a 500 µL eppendorf tube (fitting the size of the measurement hole of the magnetic sensor), and this bottle continuously injected CO_2 at 5%. Additionally, the room temperature was adjusted such as the sample remained at a temperature around 37˚C.

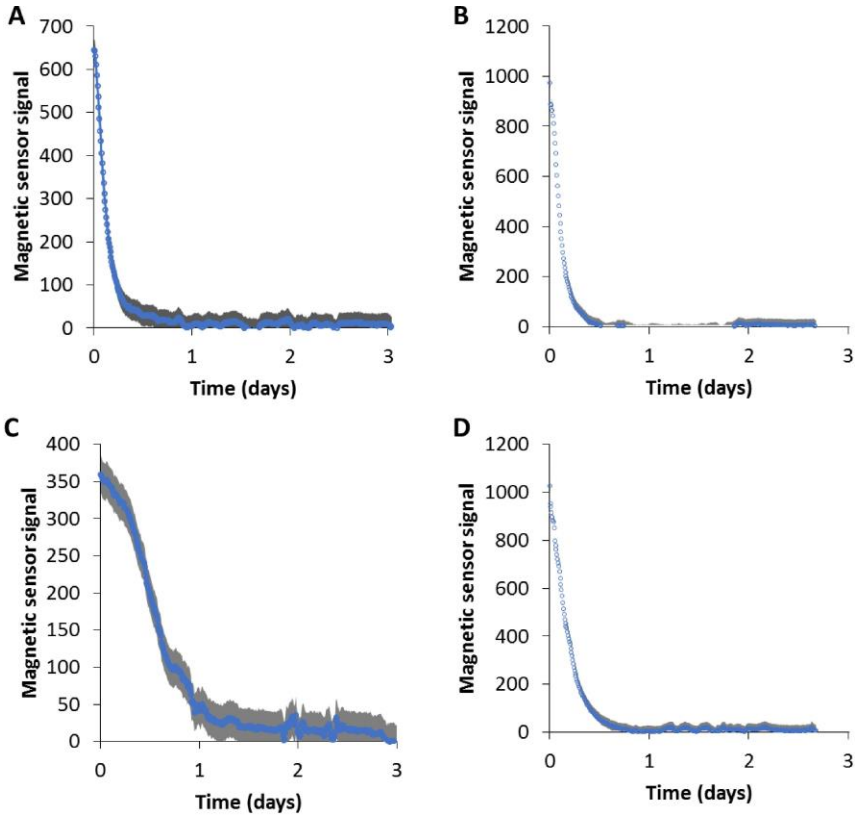

Figure S6 Real-time recordings of the degradation of magnetic nanoparticles coated with citrate (A,B) or PEG (C,D) in a lysosomal mimicking solution (pH between 4 and 4.5, citrate = 20 mM) using the magnetic sensor.

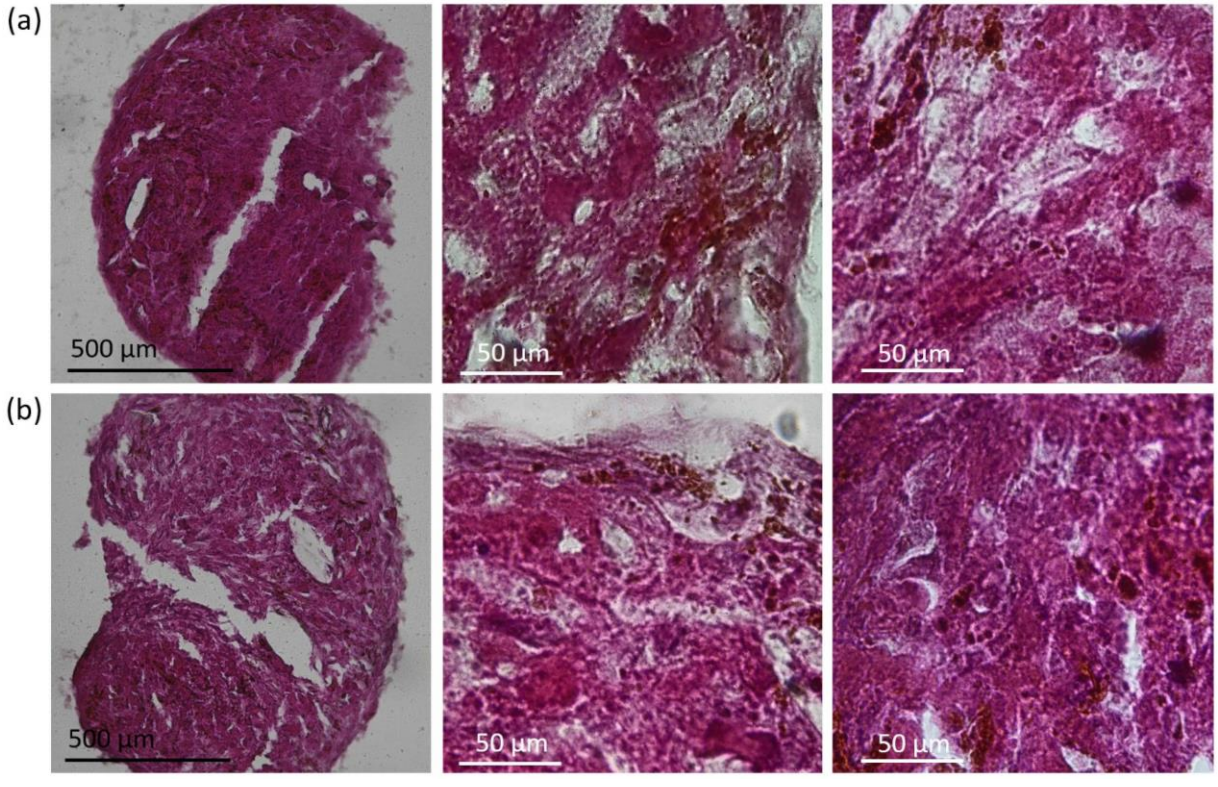

Figure S7 Histological images stained with hematoxylin and eosin show the formation of a cohesive tissue after 21 days of culture for spheroids in both (a) the magnetic sensor and (b) the incubator conditions. Middle image is a zoom of the periphery of the spheroid whereas right image is a zoom of the center of the spheroid.

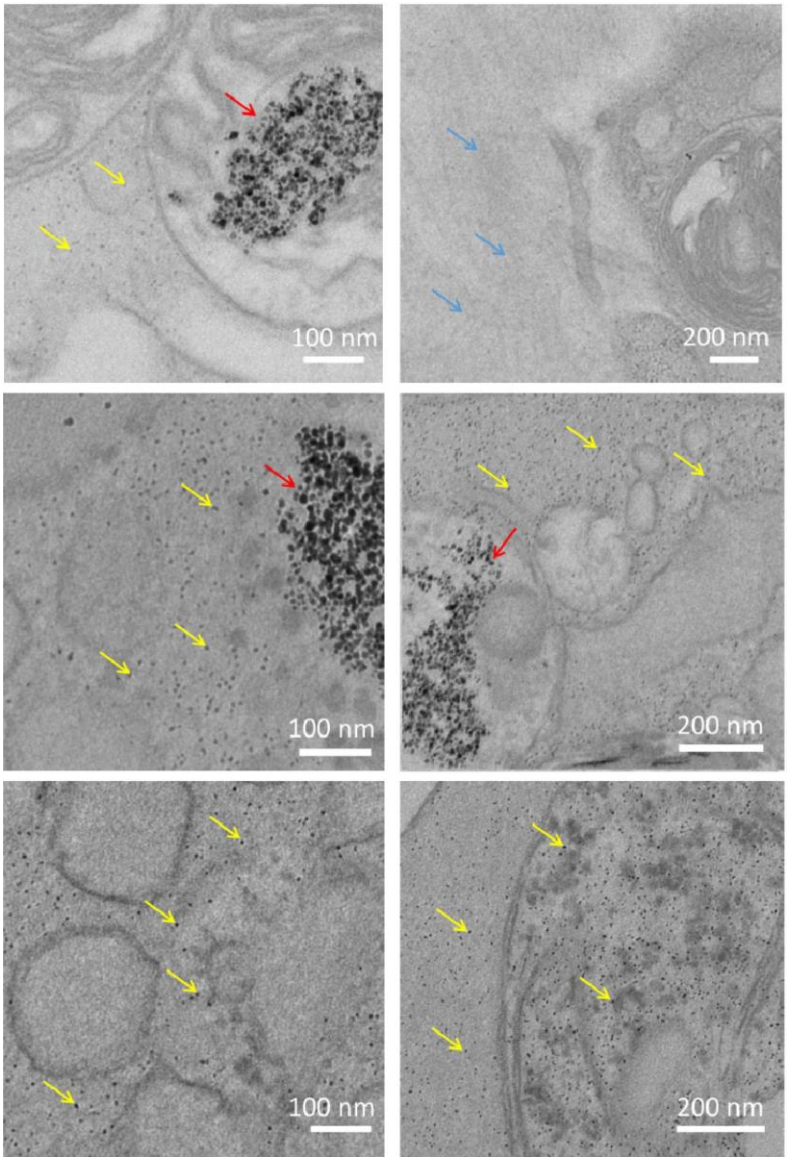

Figure S8 Representative TEM images of the cells after 6 days of continuous measurements in the Magnetic sensor followed by 15 days in the incubator for citrate-coated nanoparticles. In addition to some nanoparticles that remained intact (red arrows), small grey dots can be observed in the endosomes and the cytoplasm corresponding to the size and appearance of ferritin proteins loaded with iron (yellow arrows). The synthesis of extracellular matrix can also be observed (blue arrows), it indicates viability and functionality of the cells.

Table S1 List of primer sequences for gene expression analyses by quantitative real-time PCR.

Genes	Primers sequences (5' → 3')
RPLP0	Fwd: TGC ATC AGT ACC CCA TTC TAT CA
	Rev: AAG GTG TAA TCC GTC TCC ACA GA
ACAN	Fwd: TCT ACC GCT GCG AGG TGA T
	Rev: TGT AAT GGA ACA CGA TGC CTT T
Col10A1	Fwd: TGC CCA CAG GCA TAA AAG G
	Rev: TTT ATG GTG TAG GGA ATG AAG AAC TG
COMP	Fwd: GCCTGGCTGTGGGTTACACT
	Rev: CGTGACCGTGTTCACATGGA
Col1A1	Fwd: TGC CCA CAG GCA TAA AAG G
	Rev: TTT ATG GTG TAG GGA ATG AAG AAC TG
Sox 9	Fwd: AAA GGC AAC TCG TAC CCA AAT TT
	Rev: AGT GGG TAA TGC GCT TGG AT

RPLP0: Ribosomal protein large subunit P0; ACAN: Aggrecan; Col10A1: Collagen type X; COMP: Cartilage oligomeric matrix protein; Col1: Collagen type I; Sox9: SRY-Box Transcription Factor 9.